

UCLA

UCLA Electronic Theses and Dissertations

Title

Transient analysis of flash cooling for dynamic thermal management for high-performance electronic systems

Permalink

<https://escholarship.org/uc/item/8510z7zd>

Author

Shah, Ujash

Publication Date

2023

Peer reviewed|Thesis/dissertation

UNIVERSITY OF CALIFORNIA

Los Angeles

Transient analysis of flash cooling for dynamic thermal management
for high-performance electronic systems

A dissertation submitted in partial satisfaction of the
requirements for the degree Doctor of Philosophy
in Mechanical Engineering

by

Ujash Dipakkumar Shah

2023

© Copyright by

Ujash Dipakkumar Shah

2023

ABSTRACT OF THE DISSERTATION

Transient analysis of flash cooling for dynamic thermal management
for high-performance electronic systems

by

Ujash Dipakkumar Shah

Doctor of Philosophy in Mechanical Engineering

University of California, Los Angeles, 2023

Professor Timothy S. Fisher, Chair

Flash cooling is a promising high-heat-flux cooling solution that utilizes pressure-controlled boiling of liquid coolant. This two-phase cooling solution is inherently transient and therefore less understood than traditional cooling approaches. Flash cooling has been studied previously based on individual cooling pulses rather than a continuous convective cooling solution. Convective cooling is an integral part of high-performance computing infrastructure with emerging needs for two-phase cooling due to increasing heat fluxes. The primary objective of this work is to enable dynamic thermal management of high-heat flux high-performance systems through foundational understanding of the transient mechanisms associated with pulsed, pressure-driven flash cooling techniques. A thermal testbed is developed for continuous, pulsed experiments for flash cooling with sufficient flexibility to adapt to several cooling architectures and electronic devices. A set of surrogate models are developed to enable system-design and run-time prediction

for flash cooling that can be deployed for specific applications. The emphasis is on the integration of thermal data for optimal and predictive flash cooling. A next-generation high-heat-flux application that requires dynamic cooling is Silicon Interconnect Fabric, which is a platform that allows heterogeneous integration and system scaling on a silicon wafer. This platform requires large heat removal over a large area without any accommodation for heat spreading outside of the active zones. Three innovative architectures are developed to provide flash cooling for this application. The fabrication of individual prototypes and comparison of preliminary steady-periodic testing provides vital information for selection of architecture. A detailed analysis of one of the architectures – the segmented pin-fin cooling chambers, is performed with a set of thirty experiments spanning wide range of heating and cooling conditions. Several representative surrogate models are developed from this thermal data for this application that demonstrates the efficacy of flash cooling for dynamic cooling. This work lays a strong and wide foundation for understanding transient behavior of flash cooling for high-performance electronic systems, and also provides significant support material for enabling further research to enable adoption of flash cooling for broader commercial applications.

The dissertation of Ujash Dipakkumar Shah is approved.

Vijay K. Dhir

Richard B. Kaner

Subramanian S. Iyer

Timothy S. Fisher, Committee Chair

University of California, Los Angeles

2023

Table of Contents

Abstract	ii
List of Figures	viii
List of Tables	xviii
List of Symbols	xx
Acknowledgements	xxi
Vita	xxii
Chapter 1: Introduction	1
1.1. Motivation: Scientific perspective.....	1
1.2. Motivation: Technological perspective	7
1.3. Objectives.....	14
1.4. Organization.....	15
Chapter 2: Background	17
2.1. Mechanistic studies for boiling	17
2.2. Flash cooling	21
2.3. Numerical techniques for transient two-phase flow.....	26
2.4. Explored methodologies.....	35
2.5. Empirical limits for cooling Si-IF	45
Chapter 3: Continuous, pulsed flash cooling for Si-F	49
3.1. Flash cooling testbed.....	49
3.2. PowerTherm 1.0 (PT1).....	56
3.3. Steady-periodic analysis.....	58
3.4. Prototype results.....	60
Chapter 4: Wafer-scale cooling with pin-fin flash chamber	66

4.1. PowerTherm 2.0 (PT2).....	66
4.2. Lumped capacitance analysis	68
4.3. Prototype results.....	69
4.4. Thermal test vehicle	73
Chapter 5: Segmented thermal management with array of pin-fin flash chambers	77
5.1. Thermal Dissipation Unit (TDU)	77
5.2. Steady-periodic averaged, effective heat transfer coefficient	80
5.3. Prototype results.....	81
5.4. Comparison between cooling architectures.....	84
Chapter 6: Surrogate modeling for dynamic flash cooling	86
6.1. Dynamic flash cooling	86
6.2. Implementation of surrogate modeling	88
6.3. Extensive testing and surrogate modeling of TDU prototype	95
6.4. Improved heat sink and smaller ceramic heater	109
Chapter 7: Flash cooling in a vapor chamber.....	113
7.1. Flash vapor chamber (F-VC).....	113
7.2. Extension of testbed and analysis tools for vapor chamber application.....	113
7.3. Prototype results.....	116
Chapter 8: Conclusions.....	120
8.1. Future work	123
Appendix A: Utility code for processing transient data.....	127
Appendix B: Parameter code and steady-periodic analysis	136
Appendix C: Transient estimation code	142
Appendix D: Dominant frequency-driven analysis	151

Appendix E: Optimization code for thermal test vehicle..... 160
Appendix F: Thermal data for surrogate modeling..... 171
References 172

List of Figures

Figure 1: Graphical representation of flash cooling system. Saturated liquid is pulsed into a low-pressure “flash” chamber to initiate rapid-phase change..... 1

Figure 2: 1-D block homogeneous material with a constant pulsed heating and variable cooling conditions, reproduced from [2]. 3

Figure 3: Non-dimensional temperature (T^*) vs Non-dimensional time of anticipation (Fo); solid lines represent $T(x = L)$ and dotted lines represent $T(x = 0)$; Left: Constant pulsed cooling, Right: Convective cooling. These images are reproduced from [2] 4

Figure 4: Comparison of thermal response time of different cooling techniques with respect to base heat flux under heating ramp-up condition, adapted from ([5], Fig. 9a). The overlay identifies key information discussed in this document. 5

Figure 5: Energy consumption for information and communication technology, reproduced from [8] . The energy forecast highlights the computing energy crisis projected over the next decade. 8

Figure 6: (a) Silicon Interconnect Fabric on a 4-in wafer for demonstration, reproduced from [10]. (b) The basic toology of Si-IF is described with emphasis on metal bonding between Cu-pads and Cu-pillars. 9

Figure 7: System-level requirements for a 12-in Si-IF system are documented. Multiple Si-IF wafers on a single rack / chassis would require combination of power and thermal overheads. . 10

Figure 8: Depiction of heat removal from System-on-Chip (SOC) VS a wafer-scale Si-IF. The difference in size of the system, and the lack of heat spreading are highlighted..... 12

Figure 9: A cartoon depicting spatially and temporally varying temperature distribution across a Si-IF system. The cooling solution should be able to adapt and address worst-case workloads.....	12
Figure 10: Forces acting on a bubble in a liquid pool, reproduced from [2]......	19
Figure 11: Different flow regimes for forced convection flow boiling in circular tubes as described in [21]. The image is reproduced from [21].	20
Figure 12: Phase-change transitions for evaporation waves, reproduced from [23]	23
Figure 13: Test chamber and obtained cooling rate measured in previous work [3]. The peak cooling rate of flash cooling is very high and acts as a motivation for this work. The images are reproduced from [6].	24
Figure 14: Comparison of depressurization rates and onsets for various average initial temperatures corresponding to different heat inputs.....	25
Figure 15: Horizontal tube setup for pressure wave propagation experiments, reproduced from [18]......	25
Figure 16: Demonstration of pressure undershoot, reproduced from [18].	26
Figure 17: A representative volume element for the mesoscopic approach for pure homogenous boiling. Reproduced from [27]......	27
Figure 18: (a) Simulation results to show onset of flash boiling. (b) zoomed in view near the critical time. Figure 18 and b are reproduced from [27]......	28
Figure 19: VAT Based Modeling workflow as described in and reproduced from [31]......	29
Figure 20: Discretization within a pipe in EcosimPro for 1D analysis. The image is reproduced from [32].	32

Figure 21: Hierarchical mechanistic study for flash cooling with rapid depressurization playing a significant role..... 36

Figure 22: Spinodal curves for liquid-vapor, overlay with a $T_2 < T_s$ curve. The yellow zone between T_1 and T_s represents the superheating required to achieve phase change. The green zone represents depressurization leading to superheated liquid state. The image is adapted from [19]. 37

Figure 23: (a) Experimentation is limited by several factors to measure state parameters only at certain locations. (b) Desired target distribution of known state properties for controlled cooling is shown. 38

Figure 24: System-level analysis with a single diameter tube being the component of interest. First step is to perform time-averaged steady state estimates. 39

Figure 25: Kalman filter to improve transient model for single tube analysis. 43

Figure 26: The Bayesian framework will help optimize the flash cooling process for cooling architecture once a Kalman filter modified model for single tube is available. 44

Figure 27: Typical surrogate model workflow to develop an engineering model from experimental or simulation data..... 45

Figure 28: Flash cooling setup version 1 [13]. (a) Different components supporting the thermal testbed including the vacuum pump and the power supply are shown. (b) The zoomed-in view provides details of the preliminary flow testing. (c) A simplified workflow of the two-phase loop. 49

Figure 29: Comparison of water, methanol, NOVEC649 and R-134a for flash cooling. (a) Saturation properties to determine use of compressor or vacuum pump (b) Latent heat of

vaporization as function of saturation temperature (c) Mass flow rate required per kW of cooling derived from phase change.	52
Figure 30: Flow chart for dynamic control of the setup with the help of LabVIEW and CompactDAQ.	54
Figure 31: Simplified P&ID for the thermal testbed for flash cooling experiments [24]. The actual CompactDAQ controller used is included in the image.....	54
Figure 32: Template for lab journal developed in Microsoft OneNote	55
Figure 33: Corrected pulse interval VS specified pulse interval	56
Figure 34: Calibration of injection control for flash cooling.....	56
Figure 35: Architectural design of PowerTherm 1.0 [13] that incorporates block-and-tube arrangement. The silicon wafer has increased transparency to highlight the arrangement. The power delivery path from PowerBoard and heat removal path through the tubes are shown in the SIDE view.	57
Figure 36: Cartoon depicting terminal block attached to a silicon die with prototype dimensions.	58
Figure 37: Attachment of copper block to silicon die is enabled through Ni and Sn thin films... 58	
Figure 38: Prototypes for PowerTherm 1.0. (a) Single Si coupon with single block and tube (b) Array of blocks and tubes for 100 mm Si-IF testing (not finished as architecture discontinued).....	59
Figure 39: Single pulse cooling of silicon with terminal block (PT1 prototype) is demonstrated by the drop in T_b . The pulse is indicated by the outlet pressure jump indicated on the secondary axis.	61

Figure 40: Temperature profile and pressure variation for different pulse cycles under constant heat load condition. (a) 40s flash cycle, (b) 20s flash cycle, (c) 15s flash cycle..... 63

Figure 41: Comparison of different flash cooling pulse timing under the same heat load with PT1 cooling architecture. 64

Figure 42: Architectural design of PowerTherm 2.0 [24] that incorporates a wafer-scale cooling chamber with pin-fins to enhance heat transfer for flash cooling..... 66

Figure 43: Prototype of pin fin cooling chamber. (a) Copper pins inserted into the top and bottom layers (b) Thermo-compression bonding of pins to Si-IF. (c) Prototype with fluid connections for thermal test bed. 68

Figure 44: Continuous pulsed cooling with 1.5 mL methanol per pulse. (a) Temperature profiles for different heating power and duration of pulse (b) Heat estimations from natural convection, radiation and flash cooling based on (44) for case 3 (22 W,40 s). The dashed line represents the periodic averages over 240s and tabulated in Table 8. 70

Figure 45: Continuous pulsed cooling with 1.5 mL methanol every 40s but different heating. (a) Outlet pressure indicating the chamber conditions over time (b) Cooling rate as calculated based on (44) from obtained temperature profiles in Fig. 44a..... 71

Figure 46: Continuous pulsed cooling with 1.5 mL methanol for heating power of 22 W. (a) Outlet pressure indicating the chamber conditions over time. (b) Cooling rate as calculated based on (44) from obtained temperature profiles in Fig. 44a..... 72

Figure 47: Optimization of thermal test vehicle with the help of Jupyter notebook. Single or double metal layer trace parameters are optimized for maximum joule heating given power supply and safety constraints. 73

Figure 48: Nichrome TTV fabrication process flow for single metal layer nichrome deposition 74

Figure 49: Two-step relay control for dynamic heating. The CompactDAQ can only support small current relays (<1.5A) so external relays are used to handle actual current flowing through the heaters..... 74

Figure 50: Nichrome based TTV; a) After nichrome deposition, b) IR imaging without emissivity adjustment, c) Black coat of about 30 μm for uniform emissivity, d) IR imaging with uniform emissivity (Controlled heating is visible) 75

Figure 51: Nichrome heating layer with copper routing layer to act as thermal test vehicle providing up to 0.3 W/mm². 75

Figure 52: Double-sided nichrome deposition on Al₂O₃ ceramic substrate. Both sides are shorted with the help of nichrome coating in the lug area..... 76

Figure 53: Images of nichrome TTV on ceramic wafers. Minor scratches visible when using a magnifying glass. 76

Figure 54: Resistance map of nichrome TTV on ceramic wafer. Green and red box indicates good and bad connection, respectively, between back and front side of the wafer..... 76

Figure 55: Description of the architecture for segmented thermal management with flash cooling zones. Each zone consists of a flash chamber with individual inlet and outlets. A top plate combines all zones into a common entity and connects them with the inlet and..... 77

Figure 56: Construction of single flash chamber. (a) Walls attached to a commercial heat sink (b) Machining in top plate for grooves and holes (c) Assembly of copper heat sink with top plate via O-ring. 79

Figure 57: Assembled single flash chamber with inlet and outlet tubes, 3 temperature sensors, 1 pressure sensor, 1 heater cable, and 4 1/4-20 UNC bolts. 79

Figure 58: Steady-periodic pulse testing with 1 mL methanol. (a) Temperature profile for different pulse intervals for 22 W heating. (b) Outlet pressure indicating chamber conditions. (c) Outlet temperature clearly indicating pooling of liquid inside chamber for 10s pulse interval. (d) The plot shows behavior of sidewall temperature sensor for 20s pulse interval. 82

Figure 59: Comparison between 22W and 44W testing for similar cooling conditions..... 83

Figure 60: Different volume of methanol every pulse with 44 W heating and 20s interval. (a) Different steady-periodic temperatures observed. (b) Consistent pressure fluctuations. (c) With 2 mL methanol injection significant pooling of liquid in the chamber..... 83

Figure 61: Demonstration of anticipatory cooling effect on the TDU prototype. (a) The expected non-dimensional plot as per discussion in section 1.1, Fig. 3 (reproduced from [2]). (b) Temperature change observed under different anticipation times for a 22 W heat input to the TDU prototype demonstrating the reduction in peak temperature observed due to anticipated flash pulse during heat ramp-up. 86

Figure 62: Ramp-up test from 22 W to 44 W under 3 different conditions..... 87

Figure 63: Surrogate model workflow for flash cooling experiments as adapted from the general workflow described in section 2.4.3, Fig. 26. 89

Figure 64: Steady-periodic surrogate modeling approach for system-design 90

Figure 65: File and data management for surrogate modeling 94

Figure 66: Sample results for 150 W heating power (0.12 W/mm^2) and with varying coolant parameters showing all 5 different states..... 97

Figure 67: Distribution of State of cooling against input parameters (a) 3D scatter plot highlighting qualitative trends (b) Density of scatter point reflects the relative number of experiments at each power level. 98

Figure 68: Distribution of state markers at 200 W. (a) Plane cross-section (b) Function of v_p and t_p	98
Figure 69: State of cooling at different flow rate and different input power. This data is obtained from the parameter file (Fig. 66).....	99
Figure 70: Average base temperature and its fluctuations. (a) Function of power levels (b) function of file number	99
Figure 71: Effective heat transfer coefficient evaluated from steady-periodic averaging is shown here. (a) Higher heat transfer coefficients are obtained at lower cumulative efficiencies for limited power input. (b) The higher base temperature cases indicate lower heat transfer coefficient.	100
Figure 72: Cumulative efficiency from steady-periodic data compared to effective flow rate obtained.....	100
Figure 73: Comparison of average flash cooling between developed surrogate model to the actual values obtained through data averaging. (a) Comparison for states 2, 3 and 4. (b) Percentage error of the surrogate model at different power inputs to the heater.....	101
Figure 74: Comparison of base temperature data from dominant frequency-driven steady-periodic model and original data.....	102
Figure 75: Steady state experiments to determine Gloss.....	103
Figure 76: Estimation of flash cooling with curve-fitted parameters at a given input combination. (a) Heat components for complete experiment are shown along with recorded base temperature. (b) Focusing near 200-s timestamp, better visualization of individual pulses.....	104

Figure 77: Estimation of effective heat transfer coefficient based on the transient model. (a) Data for first 600-s of experiment, highlighting the initial peaks obtained at higher temperature. (b) Focusing near 200-s timestamp to understand the behavior for individual pulses..... 105

Figure 78: Estimated effective heat transfer coefficient utilizing both steady-periodic and transient models as applicable (section 6.1) for each case..... 106

Figure 79: Estimated effective heat transfer coefficient compared to the steady-periodic base temperature at constant heat input of 200-W..... 107

Figure 80: (a) Comparison of original temperature data with predicted temperature from fitted flash cooling expression. (b) Looking around time=180 s, the reduction in sensor data frequency may lead to incorrect cooling decisions below 1 Hz. 108

Figure 81: Representative CAD cut-sections for TDU. (a) Configuration 0 with fluid inlet at the top plate. (b) Configuration 1 with fluid inlet close to copper base..... 109

Figure 82: Watlow Ultramic 600 Advanced Ceramic Heater provided by Thermal Devices, Inc [51]. The heater dimensions are 25 x 15 mm². 110

Figure 83: Averaged base temperature is recorded over time for four demonstration experiments performed with the smaller ceramic heater. 111

Figure 84: Experimental flash vapor chamber setup with corresponding P&ID. An injection syringe is added to the testbed for filling procedure of methanol [24]. 114

Figure 85: Flash vapor chamber results with different initial volume of methanol in the vapor chamber (a) Change in average vapor chamber temperature vs. time for different amounts of methanol under constant 6.2 W heat input. (b) Results for transient cooling rate of vapor

chamber with a constant heat load (c) Cumulative energy dissipation of vapor chamber due to flash cooling. (d) Cumulative phase-change efficiency based on (61). 117

Figure 86: Results for transient cooling rate of the vapor chamber for various heat loads with constant working fluid volume of 3 mL. 119

List of Tables

Table 1: Comparison of chip-scale and wafer-scale thermal requirements	12
Table 2: Empirical cooling limits for Si-IF.....	47
Table 3: Preliminary selection of coolant for laboratory flash cooling tests	53
Table 4: Estimation of flash cooling enthalpy for R134a, R410a and R1234ze based on CoolProp	53
Table 5: Parameter selection for PT1 prototype	61
Table 6: Steady-periodic averaged data for PT1 prototype	64
Table 7: Parameters selected for flash cooling with PT2 prototype.	69
Table 8: Periodic averaged observations and calculations. Data is collected for 240 s (t=160 s to 400 s) and thus incorporates complete pulses for all 5 cases.....	73
Table 9: Parameter selection for flash cooling with TDU prototype.....	81
Table 10: Steady-periodic analysis with effective heat transfer coefficient calculations as described in sectioned 5.2.....	84
Table 11: Qualitative comparison of three architectures for flash cooling of the Si-IF	85
Table 12: Comparison of steady-periodic averages observed at similar input parameters for different representative prototypes	85
Table 13: Parameter space for detailed experiments and surrogate modeling of TDU prototype.	96
Table 14: Definition and conditions for state of cooling	96
Table 15: Variables obtained for frequency-driven analysis using steady-periodic averages for a specific experiment (case 20).....	102

Table 16: Reduction in operating temperature with configuration 1. The extension of inlet tube closer to base surface reduces bypass and enhances overall heat transfer for flash cooling.....	109
Table 17: Preliminary data for demonstration tests with the assembly of improved heat sink with smaller ceramic heater. The data is compared at 170-s test time is considered as an example.	112
Table 18: Comparison of steady-periodic averages of TDU with flash vapor chamber observed at similar input parameters.	119

List of Symbols

A	Surface area [m ²]	N_l	Number density [m ⁻³]
D_h	Hydraulic diameter [m]	k_b	Boltzmann constant [J/K]
L	Length of tube/chamber [m]	m	Molecular weight [g/mol]
P_l	Pressure of liquid phase [Pa]	h_{fg}	Latent heat of vaporization [J/kg]
P_v	Pressure of vapor phase [Pa]	J	Rate of bubble nucleation [m ⁻³]
P_{sat}	Saturation pressure [Pa]	k_l	Thermal conductivity of liquid [W/m-K]
P_r	Reservoir pressure [Pa]	k_v	Thermal conductivity of vapor [W/m-K]
P_f	Flash chamber pressure [Pa]	k_s	Thermal conductivity of solid matrix in porous media [W/m-K]
T_l	Liquid temperature [K]	D_d	Bubble departure diameter [m]
T_v	Vapor temperature [K]	t_w	Waiting time [s]
T_{sat}	Saturation temperature [K]	FO	Fourier number
T_s	Average surface temperature [K]	α_l	Thermal diffusivity of liquid [m ² /s]
T_∞	Bulk fluid temperature [K]	α_v	Thermal diffusivity of vapor [m ² /s]
T_m	Mean fluid temperature [K]	$C_{p,l}$	Specific heat of liquid [J/K]
q	Heat flow rate [W]	$C_{p,v}$	Specific heat of vapor [J/K]
q''	Heat flux [W/m ²]	K	Permeability [m ²]
Q	Volume flow rate [m ³ /s]	K_r	Relative permeability
R	Universal gas constant [J/mol-K]	μ_l	Dynamic viscosity of liquid [Pa-s]
σ	Surface tension [N/m]	μ_v	Dynamic viscosity of vapor [Pa-s]
ρ_l	Liquid density [kg/m ³]	α	Void fraction
ρ_v	Vapor density [kg/m ³]	s	Liquid saturation
r	Radius of bubble [m]	ϵ	Porosity

Acknowledgements

I would like to express my sincere gratitude and appreciation to my advisors, Professor Timothy S. Fisher, and Subramanian S. Iyer, for their constant encouragement and invaluable mentorship. Their guidance through each step of the process played an integral role in defining the path of my research and helped majorly in my progress as a researcher and a person.

I would also like to thank the following people, whose contribution to this research work and my academic development is highly appreciated:

- Faculty at UCLA for their valuable advice and research collaboration.
 - Jeff Eldredge, Laurent Pilon, Adrienne Lavine, Puneet Gupta
- Industry mentors for their critical feedback and commercial insights.
 - Ravi Mahajan, Michael Barako, Avram Bar-Cohen, Sam Gu
- Colleagues for their research collaborations, stimulating discussions and insightful feedback.
 - Kyle Jung, Matthew Ma, Yuan Hu, Haoxiang Ren, Krutikesh Sahoo, Boris Vaisband, Umesha Mogera, Pranav Ambhore, Kaiyuan Jin, Rishi Pugazhendhi
- Mentored undergraduate students for collaborative learning and cultivating communication skills to convey different perspectives.
 - Chen Ling, Stephen Eicher, Austin Tang, Abraham Alidadi, Alexandra Bajaras, Jasanpreet Pandher, Alex Pagano, Peter Worton, Maksim Bondarenko, Lorenzo Ontiveros, Anand Janev
- My parents, Kanan and Dipak Shah, for providing consistent support for my endeavors even through personal difficulties.

Vita

Ujash D. Shah

PhD Candidate, University of California, Los Angeles

A. Professional Preparation

University of California, Los Angeles	Mechanical Engineering	Ph.D. (Expected), 2023
Purdue University, West Lafayette	Mechanical Engineering	M.S. (Transfer), 2017
BITS-Pilani, Goa	Mechanical Engineering	B.E. (Honors), 2016

B. Appointments

University of California, Los Angeles

Graduate Student Researcher (MAE, ECE)	2017 – 2022
Teaching Assistant	2020 - 2021

APC Workforce Solutions II, LLC, San Diego

Thermal Intern	2018
----------------	------

Purdue University, West Lafayette

Grader	2017
S. N. Bose Scholar	2015

University of British Columbia, Vancouver

Visiting Researcher	2015
---------------------	------

BITS-Pilani, Goa

Teaching Assistant	2016
Certified Instructor, CTE	2014 - 2015

Tata Technologies Limited, Pune

Summer Intern (Design) 2014

Alstom Hydro (India) Limited, Vadodara

Summer Trainee (Fabrication) 2013

C. Publications

1. **U. Shah**, M. Ma, M. T. Barako, A. Bar-Cohen, S. S. Iyer, and T. S. Fisher, "Experimental demonstration of pressure-driven flash boiling for transient two-phase cooling," in *IEEE TCPMT*, vol. 11, pp. 1604-1614, 2021.
2. **U. Shah**, S. S. Iyer, and T. S. Fisher, "Segmented thermal management with Flash Cooling for Heterogeneous Wafer-Scale Systems", *ITherm*, 2021, pp. 589-594.
3. **U. Shah**, U. Mogera, P. Ambhore, B. Vaisband, S. S. Iyer and T. S. Fisher, "Dynamic Thermal Management of Silicon Interconnect Fabric Using Flash Cooling," *ITherm*, 2019, pp. 1228-1233.
4. P. Ambhore, **U. Shah**, U. Mogera, P. Ambhore, B. Vaisband, T. S. Fisher, M. Goorsky, and S. S. Iyer, "PowerTherm Attach Process for Power Delivery and Heat Extraction in the Silicon-Interconnect Fabric Using Thermocompression Bonding," *ECTC*, 2019, pp. 1605-1610.
5. M. H. Rahman, L. Daniel, **U. Shah**, X. Bi, J. R. Grace, and C. J. Lim, "Estimation of solids circulation rate and char transfer rate from gasifier to combustor in a dual fluidized-bed pilot plant for biomass steam gasification," *Particuology*, vol. 46, pp. 22-29, 2019.
6. M. Dasar, **U. Shah**, P. P. Raikar, and R. S. Patil, "Computational Studies on Effect of Novel Accelerating Perforated Distributor on Fluid Dynamic Characteristics of Circulating Fluidized Bed Riser," *Proceedings of 12th CFB*, 2019, pp. 313-320.

Chapter 1: Introduction

1.1. Motivation: Scientific perspective

Flash boiling of liquid pools has been most studied within the context of a loss of containment event. In such scenarios, a liquid is unintentionally released from a pressurized vessel, typically to atmospheric pressure, such that the liquid suddenly exists in a superheated state. Rapid phase change ensues, having potential negative consequences. The event is commonly termed a boiling-liquid expanding-vapor explosion. However, as shown in Fig. 1, a flash cooling system that utilizes the high heat absorption rates of explosion or flash boiling can provide an excellent transient cooling solution.

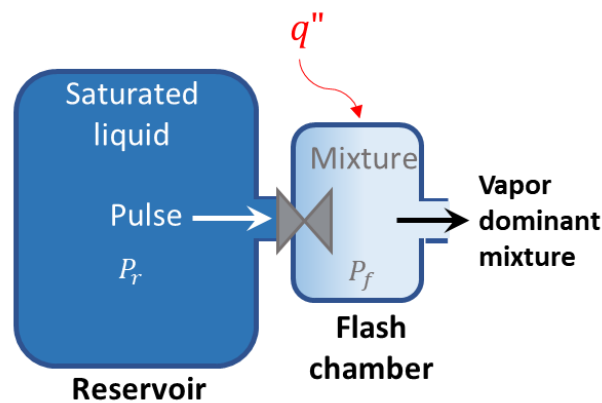


Figure 1: Graphical representation of flash cooling system. Saturated liquid is pulsed into a low-pressure “flash” chamber to initiate rapid-phase change.

Flash boiling from a liquid pool is unique in the respect that the phenomenon is inherently transient because the rate of phase change decays with time [1, 2]. Flash cooling is suitable for transient applications that require pulsed cooling for finite time periods, e.g., in the range of 100 ms to 10 s. In particular, the flash produces an initial peak cooling that wanes to a quasi-steady state plateau before the coolant is depleted. This characteristic could be useful for counteracting the thermal mass of the device to achieve a more constant transient temperature in a pulse-heated device. The pressure-controlled nature of flash cooling has been shown to produce peak heat

transfer coefficients of approximately $50,000 \text{ W/m}^2\text{K}$ [3]. Flash cooling is inherently transient, and because most existing boiling literature is based on steady-state phenomena, the scientific understanding of flash cooling is limited. Previous work on flash cooling [2] [3] has focused on empirical models or effects on solid-state boundaries; however, they have not deeply considered the fluid mechanics aspects of the process. The interaction of explosion boiling along with porous media leads to complex physical phenomena over multiple length scales. Even though the computational capability for solving complex problems has increased exponentially over the last two decades, the calculations needed to accurately model the science behind boiling processes is still a challenge even for steady-state boiling processes. Related research typically seeks either to understand effects at a single-bubble-level [4] or at a scale where only the macroscopic effects are considered.

1.1.1. Two-phase cooling

For any cooling system with fluid flow implementation, the thermodynamic limit of heat extraction is constrained by the temperature of the application. If the exit temperature of the fluid from a heat sink is the same as the operating temperature (or base temperature of the heat sink), it is not possible to transfer further heat, and thus it represents the limit of heat exchange for cooling system. For a single phase system, the maximum heat removal is then limited by the sensible heating provided between the inlet temperature and the operating temperature. However, the enthalpy change associated with a two-phase flow incorporates both sensible and latent heat, thus providing much higher thermodynamic limit of heat transfer from the device or the base of the heat sink. Mechanistically, the formation of vapor bubbles from surrounding liquid requires large amount of heat on the surface of the heat sink. This enables two-phase cooling solutions to absorb large amount of heat flux. Additionally, the phase change process allows for significantly lower mean

fluid temperature, thus enhancing the overall heat transfer coefficient obtained during the heat exchange.

1.1.2. Transient thermal phenomenon

The thermal resistance of a system or material is considered as an extensive heat property has become a standard for measuring the effectiveness of a cooling. The concept has been developed due to its relation to Ohm's Law in electrical circuits and can be expressed as,

$$R_{th} = \frac{\Delta T}{q} = \frac{T_j - T_\infty}{q} \quad (1)$$

where R_{th} is the thermal resistance, T_j is the junction temperature of the target object, T_∞ is the temperature of the fluid and q is the heat flow through the system. For a given heat flux requirement and steady-state coolant temperature, the thermal resistance dictates the junction temperature. This leads to the popularity of the term, especially in electronics packaging. However, this approach fails to model the behavior of a system when the heat loads are not constant, and even the addition of the concept of capacitance from linear circuit theory fails to capture critical phenomena such as a change of phase in transient thermal problems. It is emphasized that in the high-performance electronic systems, the loads are dynamic in nature, and thus understanding the transient response is crucial to the engineering of thermal management solutions.

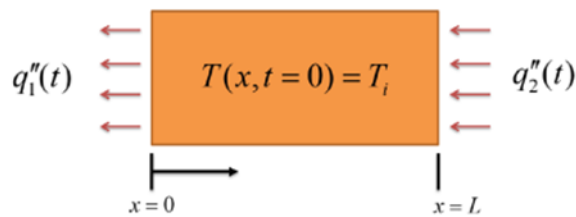


Figure 2: 1-D block homogeneous material with a constant pulsed heating and variable cooling conditions, reproduced from [2].

A set of simulations are performed in [2] that show the significance of transient response in 1-dimensional system. Consider a block of homogeneous material as shown in Fig. 2. The whole block is initially at a uniform temperature, T_i . Then a constant pulsed heat load is applied, which can be considered like a processor being turned on. The temperature at the junction, $T(x = L)$, is observed with different cooling conditions. In terms of steady-state behavior, if you apply same amount of cooling the block should remain at T_i .

However, as shown in Fig. 3, due to the transient response of the material of the block, the eventual temperature of the block is different from what would be predicted from a steady-state solution based on thermal resistance (blue curve). The effect is a result a combination of effect of thermal capacitance of the block and the speed of heat diffusion in the block. Importantly, if the cooling pulse is started in anticipation of the heat load, the final temperature of the block is less. If the cooling is convective in nature (Fig. 3), then cooling is proportional to $T(x = 0)$ and the peak temperature which is diminished over time, and eventually the steady-state solution is achieved with no temperature change. However, during the transient process the surface has seen temperature variation, which can be reduced again by anticipation. These results show two things:

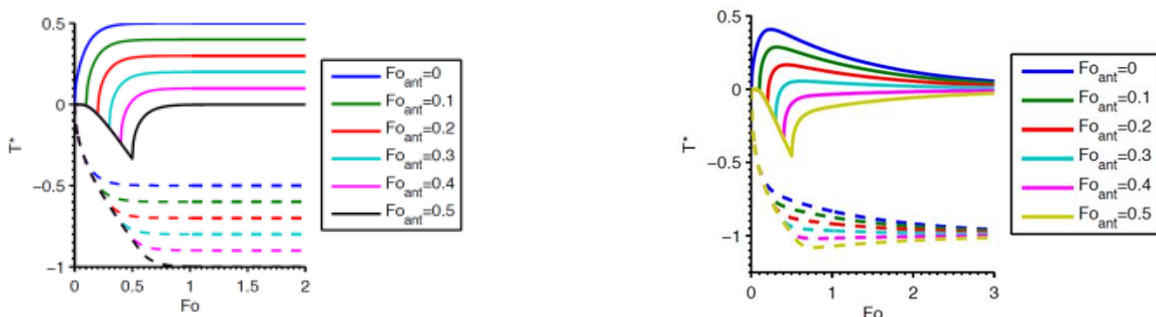


Figure 3: Non-dimensional temperature (T^*) vs Non-dimensional time of anticipation (Fo); solid lines represent $T(x=L)$ and dotted lines represent $T(x=0)$; Left: Constant pulsed cooling, Right: Convective cooling. These images are reproduced from [2]

the significance of transient considerations on temperature of system components, and the importance of anticipatory cooling for high-heat flux applications.

The analysis of thermal response time is shown in [5] with the help of temperature ramp-up associated with the heater power “on”. Thermal response time, τ_r , was defined as the duration per unit change in temperature during heat loading or unloading. The article considers different active and passive cooling technologies, and determines the time taken for achieving peak temperature during loading. The response time in such scenarios can be expressed as [5]:

$$\tau_r = \frac{t_{\Delta T_{peak}}}{\Delta T_{peak}} \quad (2)$$

The thermal response time and heat flux requirements of different applications, and different cooling approaches are shown in Fig. 4. Microprocessor chips and corresponding

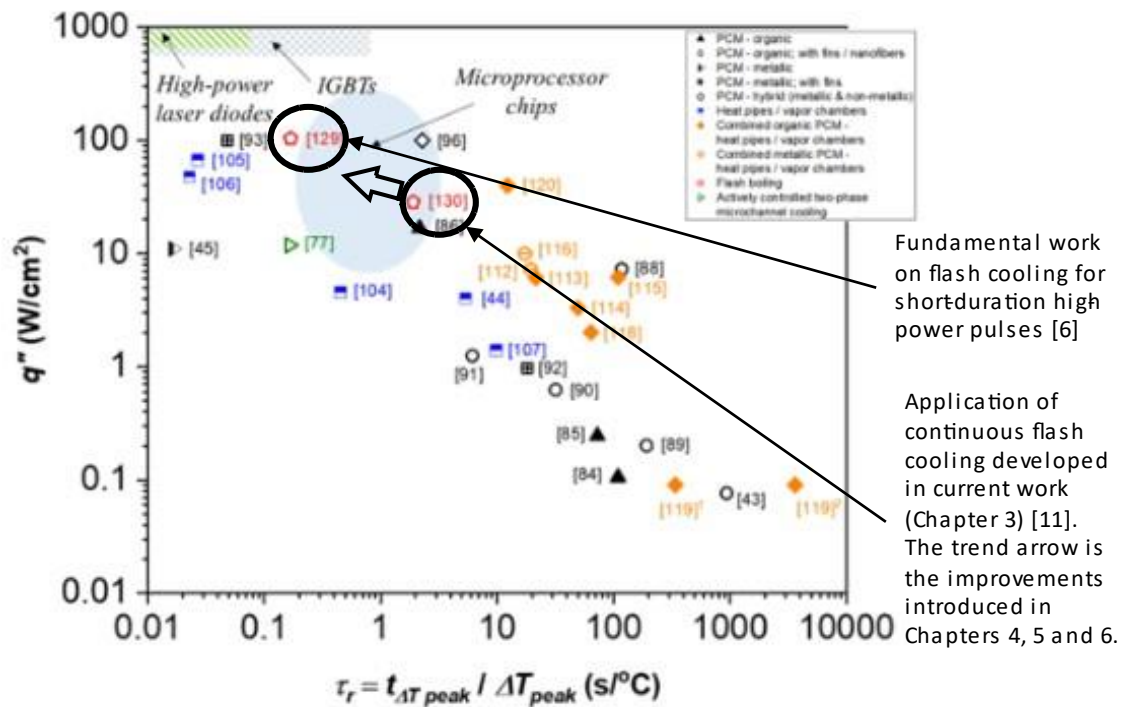


Figure 4: Comparison of thermal response time of different cooling techniques with respect to base heat flux under heating ramp-up condition, adapted from ([5], Fig.

9a). The overlay identifies key information discussed in this document.

electronic packages require high heat flux removal while demanding fast response time. The only active cooling techniques available for this review were flash cooling, and actively controlled two-phase microchannel cooling. The identifier labeled “[129]” refers to the fundamental work on flash performed in [6], and described in detail in section 2.2. The high heat flux removal along with small response time (~ 0.1 s) for this fundamental work is a major motivation to investigate the transient behavior of flash cooling when applied to high performance systems designed for continuous operation.

The identifier labeled “[130]” refers to a flash cooling architecture that was developed in current work and presented in 2019. The details of the architecture, prototype results, and analysis is presented in Chapter 3. The presence of high thermal capacitance led to very high thermal response time. However, the cooling architecture went through iterations of improvements to provide higher heat flux removal with flash cooling while reducing the thermal response time to below 1 s. The arrow in the overlay of the image represents the direction taken for this work to understand and enhance transient response for flash cooling (Chapters 4, 5 and 6).

1.1.3. Pressure-driven boiling

Another motivation behind this study is the fact that boiling literature is dominated by temperature-controlled conditions rather than depressurization. The mechanistic models that stem from forces acting at the micro-scale and the correlation-based macroscopic models both are temperature oriented. At the same time, most boiling literature is focused on the reporting of steady-state behavior, and thus the effect of rapid depressurization is less understood. The details of these models are discussed in Chapter 2. The motivation here is to develop non-equilibrium pressure-driven mechanistic or correlational models for transient boiling.

1.1.4. Two-phase cooling for sub-boiling operating temperatures

Flash boiling is a pulsed process, and both parameters depend on time, with T_{∞} being transient and much lower than the initial bulk fluid temperature, thus enhancing the initial heat transfer from the surface. This attribute also allows flash cooling to create temporary sub-ambient temperatures [7]. A detailed explanation is included in Chapter 2, section 2.2.

1.2. Motivation: Technological perspective

1.2.1. Computing energy crisis

The shift towards e-media, e-commerce and cloud-based services has raised the world's composite electrical energy expenditure. According to a recent estimate [8], data centers in United States of America alone consume more than 90 billion kWh of electricity per year. It requires about thirty-four coal power plants (500 MW each) across the country to support just data centers. Each of the social media giants like Facebook, Twitter, and Instagram consumes energy equivalent to a power plant for processing and storing data. According to the same report, global data centers consume about 3% of total electricity produced – which is more than total electricity consumption by United Kingdom. This trend is expected to worsen with the additional computational requirements due to the computational needs of the internet-of-things and artificial intelligence [8] (Fig. 5). These requirements are not only added for data processing and storage but also due to data transfer [9]. The introduction of 5G wireless networks is an example of energy intensive technology being deployed as a requirement and as a promoter of high computing demands. Thus, it is critical for to increase the energy efficiency of data center and network components.

Traditionally, energy efficiency has been improved by making the transistors smaller and smaller, known as Moore's law [10]. However, manufacturing processes are reaching physical limitations, and thus, simply making transistor size smaller is not possible. At the same time, the

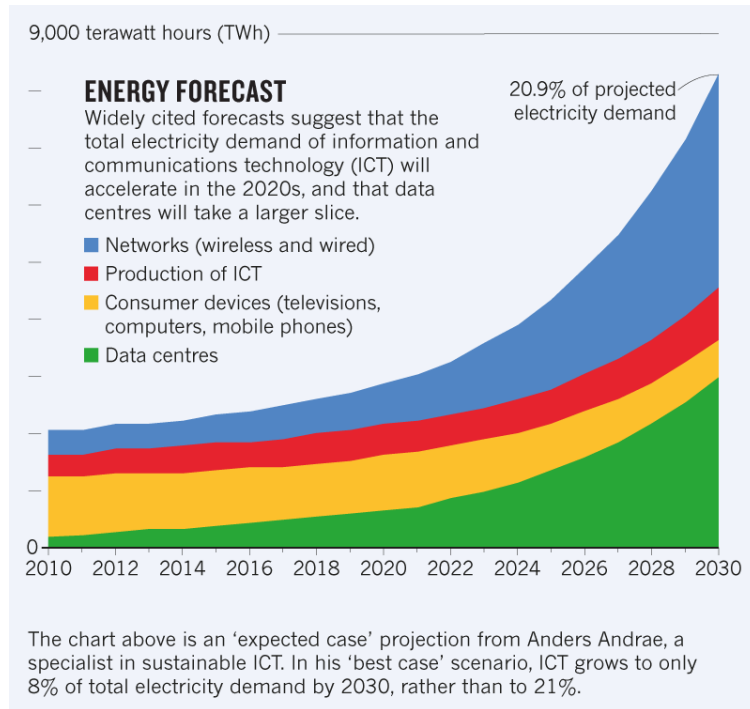


Figure 5: Energy consumption for information and communication technology, reproduced from [8]. The energy forecast highlights the computing energy crisis projected over the next decade.

manner in which these transistors are packaged has shown less change. The heat extraction and power delivery problems with smaller transistors are resolved by making extensions to the existing packaging configurations. These methods can either be insufficient and/or unable to adapt to the necessities of next-generation of electronic packages. However, moving away from Moore's law has its own challenges as discussed in next section.

1.2.2. Silicon Interconnect Fabric (Si-IF)

Data centers have become faster and more efficient by reducing transistor size. However, they still rely on extension of traditional 2D packaging techniques. From a thermal standpoint, new thermal interface materials and the optimization of cold plate sizes have been intensively pursued. In such legacy architectures, different packages are stacked together in server racks as shown, and the cooling is provided by either air flow or direct liquid flow. However, the new packaging

techniques, which includes 3D, 2.5 D (interposer-based) and wafer-level packaging techniques, generate considerable amount of heat over a specified area, and thus traditional methods are usually insufficient or unable to adapt to the requirements of new packaging techniques.

From an engineering perspective, this type of cooling technique has high potential for dynamic cooling applications. One of the best examples is the Silicon Interconnect Fabric (Si-IF) that is being developed at UCLA under the CHIPS consortium. The Si-IF is a platform that allows heterogeneous integration of dies using a fine-pitch integration approach that leverages silicon microelectronics patterning at the wafer scale [11]. Fine interconnect pitches allow compact die placement; however, such high packing density of dies leads to intense heat generation. Because the demand of processing power on an Si-IF architecture will vary with time according to the inherently variable workflow of integrated electronics, the thermal solution also should be dynamic and adaptable in nature. Thus, this work considers Si-IF as the platform to understand, optimize and demonstrate the efficacy of flash cooling technique for transient applications.

Heterogeneous integration, in which different components needed for a system are integrated on the same wafer, and system-level scaling, focusing on overall system performance, is an innovative approach for packaging. The silicon interconnect fabric (Si-IF) is a silicon-based platform that allows heterogeneous integration of dies using a fine-pitch integration approach [11,

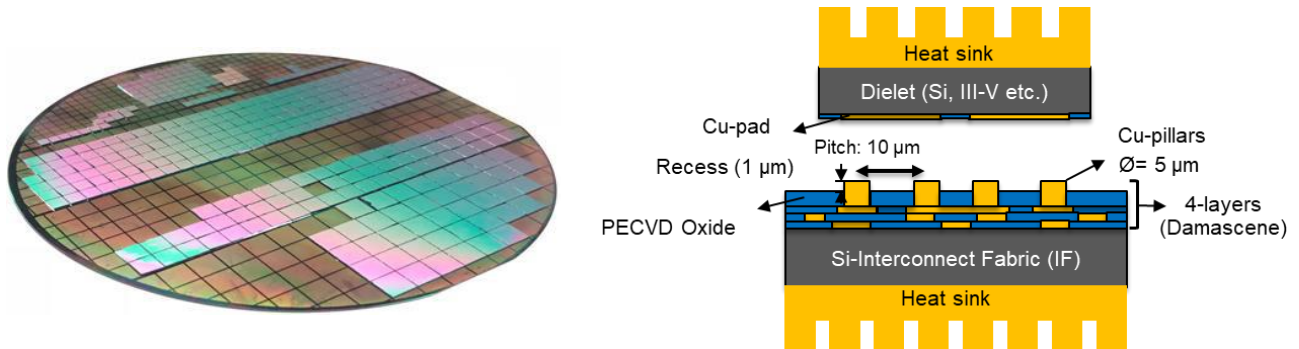


Figure 6: (a) Silicon Interconnect Fabric on a 4-in wafer for demonstration, reproduced from [10]. (b) The basic toology of Si-IF is described with emphasis on metal bonding between Cu-pads and Cu-pillars.

12]. Fine interconnect pitches allow compact die placement; however, such high packing density of dies leads to intense heat generation density (Fig. 6). Because silicon is a good thermal conductor, heat may be dissipated on both the chip and interconnect side; and for high-power radio frequency (RF) chips (e.g., GaN), heat spreading structures as well as coolant channels may be integrated into the Si-IF using established methods. The availability of the interconnect substrate as a heat spreader opens new means for efficient, on-demand cooling delivered directly to the backside of the Si-IF. Air cooling on top of the Si-IF is insufficient to cool the projected heat loads. Moreover, it would not be able to rapidly adapt to changing high-heat fluxes generated by compact die.

1.2.2.1. Thermal requirements of Si-IF

The Silicon Interconnect Fabric present co-design challenges. The power delivery and thermal management of the Si-IF is a multi-disciplinary and collaborative project termed as “PowerTherm.” The Si-IF platform would require 50 kW of power delivery and similar amount of cooling over a 300 mm wafer (Fig. 7).

Conventionally, power is delivered through periphery [13, 14]. However, peripheral power delivery has following limitations for large scale systems:

1. It is inadequate for high power systems.

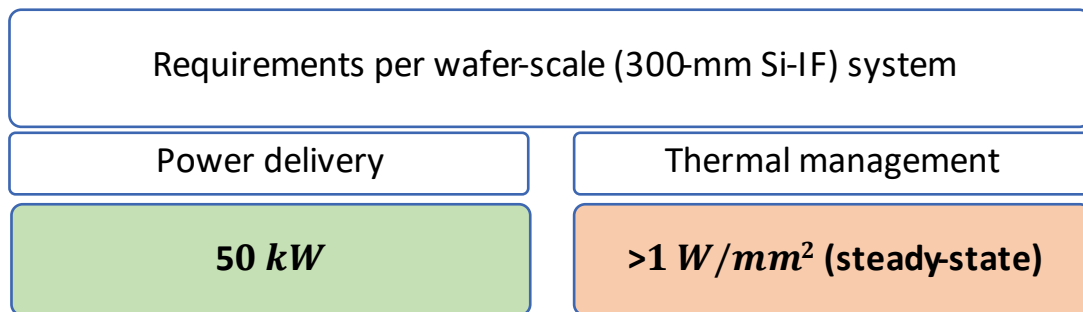


Figure 7: System-level requirements for a 12-in Si-IF system are documented. Multiple Si-IF wafers on a single rack / chassis would require combination of power and thermal overheads.

2. Power delivery at mission voltage leads to excessive voltage droop and I²R losses.
3. Power conversion at point-of-use is area inefficient.
4. It is not efficient to integrate large power components on the Si-IF.

Thus, an alternative approach for power delivery is needed. For cooling purposes, high-heat-flux generation of about 1 W/mm² is expected for the Si-IF. Considering the convective heat transfer equation, the required heat transfer coefficient would be,

$$h_{required} = \frac{q''}{T_s - T_\infty} \quad (3)$$

$$h_{required} = \frac{1}{(273.15 + 85) - (273.15 + 20)} \frac{\frac{W}{mm^2}}{K} \sim 17,000 \frac{W}{m^2K} \quad (4)$$

assuming typical wafer and coolant temperature to be 85 °C and 20 °C respectively. It is clear by looking at typical heat transfer coefficient ranges that a phase-change heat transfer is necessary to remove this large amount of heat throughout the 300 mm wafer. Si-IF has a natural advantage in terms of heat spreading on the backside as the substrate is a thin silicon wafer (about 500 μm) as opposed to organics-based laminate board in conventional electronics packaging [13]. This advantage has motivated new architectures that facilitates back-side cooling along with back-side power delivery.

A wafer-scale thermal solution presents these challenges when compared to “chip-scale” thermal management (Fig. 8 and Table 1):

- Up to 100X total heat removal
- Lack of lateral heat spreading area
 - Internal spreading possible for temperature uniformity
 - “Chip-scale” high-heat flux techniques are not feasible.

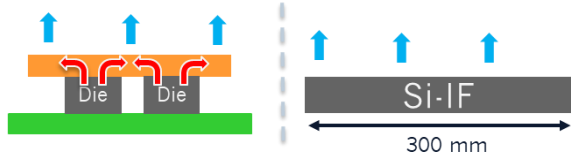


Figure 8: Depiction of heat removal from System-on-Chip (SOC) VS a wafer-scale Si-IF. The difference in size of the system, and the lack of heat spreading are highlighted.

Table 1: Comparison of chip-scale and wafer-scale thermal requirements

Characteristic	Chip-scale**	Wafer-scale
Total power	400 W	40 kW
Active area	400 mm ²	40,000 mm ²
Heat flux, q''	1 W/mm ²	1 W/mm ²
Heat spreading	Yes	No
Effective q''	>0.1 W/mm ²	~1 W/mm ²
Segmented cooling required?	No	Yes

Chip-scale requirements are calculated based on the specifications of Intel Xeon 2288G [15], 95W TDP, 1400 mm² package. Chip-scale thermal solutions can include technologies like micro-channel cooling; however, they cannot be scaled to wafer-scale systems due to high-pressure and overhead area requirements. Further details are explored in Chapter 2, section 2.5. Additionally, two-phase cooling of Si-IF requires the coolant boiling temperature to be less than 85 °C for traditional flow boiling, thus eliminating several potent coolants including water.

1.2.2.2. Dynamic processing

The energy management of data centers has improved with the help of dynamic control of individual processing components, even though the primary motivation behind the research might be improved thermal reliability. This creates spatially and temporally varying temperature and power generation distributions across any high-performance electronic system (Fig. 9). The transient peaks of up to 3 W/mm² are expected for brief intervals. However, the thermal management solutions have been dominated by steady-state approaches. However, these solutions

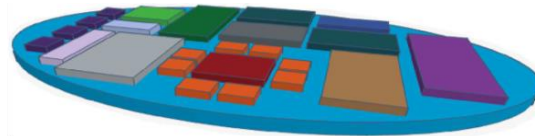


Figure 9: A cartoon depicting spatially and temporally varying temperature distribution across a Si-IF system. The cooling solution should be able to adapt and address worst-case workloads.

can be enhanced with the help of transient cooling techniques and/or by adopting predictive thermal management.

1.2.2.3. Network switch

Network switches are components that enable communication of devices over a network. Switches manage the flow of data across a network by transmitting a received network packet only to the one or more devices for which the packet is intended, allowing the switch to direct the flow of traffic maximizing the security and efficiency of the network. They go through a large number of cycles through their lifetimes. In a typical data center, there are various levels of network switches that control the flow of data. As mentioned previously, the energy consumption through network components is bound to increase, and the amount of heat generated in network switches is huge [16]. These are compelling example of components that need dynamic high-heat flux cooling solutions to operate at high efficiency and reliability.

1.2.2.4. Battery and radar applications

The use of batteries (mostly Li-ion) as electrical energy storage devices for electricity grids as well as electric vehicles (including cars, trucks, and airplanes) is increasingly popular. Batteries prove crucial to renewable energy sources like solar and wind that struggle from continuous or on-demand electricity generation. However, a major challenge with such batteries is their thermal management, especially during charging and discharging. Research is ongoing on battery thermal management for active control; however, like electronics packaging, this research tends to focus on reactive control of steady-state cooling techniques. Thus, battery packs represent an area to be explored for high-heat flux dynamic cooling.

Similarly, most radar-based devices consume large amount of energy at high, intermittent rates. As an example, some research based on micro-jet array cooling has been done for such

applications [17]. However, two-phase cooling techniques that deliver dynamic rapid cooling may allow higher frequency of operation and increase efficiency by utilizing less cooling when the device is working at lower frequency.

1.2.2.5. Single-use aerospace applications

Aerospace institutions are investigating flash cooling for the purpose of handling large initial transients associated with equipment. For example, a vapor chamber associated with heat spreading for radar may involve large heat flux when the instrument is turned on during operation or could be used only for small time interval. In such cases, a vapor chamber loaded with coolant can be used to cool large heat fluxes for short duration. This work includes foundational information on a collaborative project that led to testing of vapor chamber with flash cooling. Elaborate details can be found in [18].

1.3. Objectives

The primary objective of this work is to enable dynamic thermal management of high-heat flux high-performance systems through foundational understanding of the transient mechanisms associated with pulsed, pressure-driven flash cooling techniques. This objective encapsulates the development of a thermal testbed for transient experiments for flash cooling with sufficient flexibility to adapt to several cooling architectures and electronic devices. It also incorporates the goal of developing surrogate models to enable system-design and run-time prediction for flash cooling that can be deployed for specific applications. The emphasis is on the integration of thermal data for optimal and predictive flash cooling.

A secondary objective is to demonstrate the efficacy of the pulsed flash cooling technique for next-generation high-heat flux applications for thermal management. The primary target within this objective is to enable up to 1 W/mm^2 of cooling for wafer-scale Si-IF. This application as a

platform enables demonstration of multiple aspects – dynamic two-phase cooling that is scalable for large high-performance systems. Additionally, the different cooling architectures explored and designed in this work need to be cohesively designed with a larger system-design and validation team to enable faster adoption of flash cooling for the high-performance systems.

1.4. Organization

The first chapter introduces the report and highlights the motivation and objectives for this work. Chapter 2 provides a literature review of theory, experiments, and simulations for two-phase cooling methods. Additionally, it introduces relevant statistical techniques explored, and a brief background on preliminary testing performed on flash incipience. Afterwards, Chapter 3 discusses the implementation of a continuous, pulsed flash cooling system developed. It provides detailed information on the experimental setup and presents preliminary results of flash cooling with a block-and-tube cooling architecture. This architecture is co-designed to provide necessary power and thermal requirements. It also introduces the concept of steady-periodic averaging to analyze flash cooling. Chapter 4 presents an enhanced wafer-scale co-designed cooling architecture based on pin-fin arrangement. The improvement in heat transfer is highlighted with the help of lumped capacitance analysis for the Si-IF. It also introduces the need for a custom thermal test vehicle for demonstrating flash cooling capabilities at wafer-scale. Chapter 5 elaborates on a segmented pin-fin cooling architecture to provide scalable wafer-scale cooling solution with flash cooling. The prototype results for this segmented architecture are compared with the previous architectures. This prototype is selected for the detailed testing and provide foundation for surrogate modeling discussed in Chapter 6. Several tools developed for analyzing prototype data, create prediction and run-time models are presented in Chapter 6 as well. Section 6.2 provides details on steady-periodic and transient surrogate models developed along with sample implementation. Chapter 7 provides

an insight into extension of flash cooling application to handle large initial transients with a vapor chamber. The closing chapter layouts the conclusions and possible future directions stemming from this foundational work on implementation of flash cooling for high-performance electronics.

Chapter 2: Background

2.1. Mechanistic studies for boiling

Superheated boiling has been studied extensively in numerous ways, particularly for water. This document summarizes theoretical models for bubble nucleation, bubble growth and simplified models for internal flow boiling. The theoretical models that describe mechanisms of bubble nucleation are classified into two categories: homogenous nucleation and heterogeneous nucleation. Homogeneous nucleation occurs in the bulk of a liquid, whereas heterogeneous nucleation occurs at a solid surface or a meniscus. Homogenous nucleation models are based on two considerations, mechanical stability from classical thermodynamics and kinetic theory. Accordingly, a bubble is formed when the excess Gibbs free energy of an activated cluster of molecules is high enough to support an equilibrium bubble, coupled with the Young-Laplace for surface tension of a bubble ([19], Eq. 5.55),

$$r_c = \frac{2\sigma(T_l)}{P_{sat}(T_l) \exp\left[\frac{\{P_l - P_{sat}(T_l)\}}{\rho_l R T_l}\right] - P_l} \quad (5)$$

where r_c is the critical radius at which the bubble is formed. The kinetic limit of superheating provides the rate at which clusters with enough energy form, and thus the resulting rate of nucleation (J) is given by ([19], Eq. 5.105),

$$J = N_l \sqrt{\frac{3\sigma}{\pi m}} \exp\left[\frac{-16\pi\sigma^3}{3k_b T_l \{P_s(T_l) - P_l\}^2}\right] \quad (6)$$

Similarly, for heterogeneous nucleation, a critical radius is defined as,

$$r_c = \left[\frac{2C_1^2 \sigma T_{sat} k_l}{C_2 \rho_v h_{fg} q}\right]^{\frac{1}{2}} \quad (7)$$

where C_1 and C_2 are constants that depend on contact angle, and q is the heat flux from the surface. For heterogenous boiling, instead of the number of activated clusters the number of nucleation sites (N_a) plays a key role. Given conditions on the above equation, r_c has two values, and so all the nucleation sites with radii in the range of the two values are activated. It is difficult to predict the number of nucleation sites, and thus it remains one of the biggest uncertainties in quantifying heterogeneous nucleation. In heterogeneous nucleation, the bubble grows over the site until a departure diameter (D_d) is reached, and the time required is termed as waiting time (t_w),

$$t_w = \frac{1}{\pi\alpha_l} \left[\frac{\frac{C_2 r_c}{C_1}}{1 - \frac{2C_1 \sigma T_{sat}}{\rho_v h_{fg} r_c (T_w - T_{sat})}} \right]^2 \quad (8)$$

with the departure diameter and frequency of bubble nucleation (f) being specified by experimental models. Overall, the rate of bubble formation in heterogeneous nucleate boiling depends on several empirical factors.

For growth after nucleation, the change of radius of a bubble considering mechanical and thermodynamic equilibrium (Fig. 10) can be expressed as,

$$\frac{dr}{dt} = \sqrt{\frac{\alpha_l \rho_l C_{p,l} (T_l - T_v)}{\pi t}} \frac{1}{\rho_v h_{fg}} \quad (9)$$

However, these terms do not consider the effect of inertial forces due that may exist during flow. A more detailed analysis is available in [20].

2.1.1. Internal flow boiling

Internal flow boiling models, which can be considered as macroscopic mechanistic models, assume equilibrium steady state boiling through a pipe. Depending on the flow hydrodynamics and temperature profiles, different flow regimes have been classified [21] (Fig. 10). To model two phases in a pipe flow, several terms are defined including mass velocity, superficial velocity, and

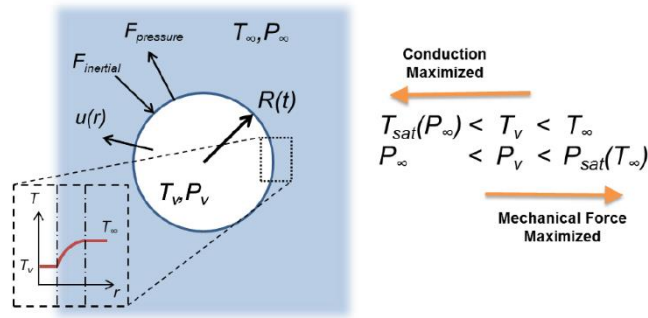


Figure 10: Forces acting on a bubble in a liquid pool, reproduced from [2].

slip velocity. These parameters help classify the flow regime ([19], Chapter 12). Also, these parameters aid in the development 1-D two-phase flow governing equations and models ([19], Chapter 10).

Generally, flow boiling problems are simulated in four diverse ways [22]:

1. Empirical or semi-empirical models. Based on single-phase flow, the approach adopts empirical correlations to calculate the wall temperature and integrated heat flux under boiling conditions by introducing coefficients to enhance heat transfer. Not considering phase changes, therefore, the calculated density, temperature and flow field distribution will be incorrect when the heat flux is high.

2. Homogenous flow models, which are used to represent both the liquid and vapor phases based on the assumption that vapor bubbles are small and perfectly mixed with the liquid phase. The concentration of vapor phase is described by an additional variable—void fraction. Thus, the governing equations are still single phase but with an additional equation to describe void fraction. The effect of density change due to the fluid phase change is fully considered, but detailed

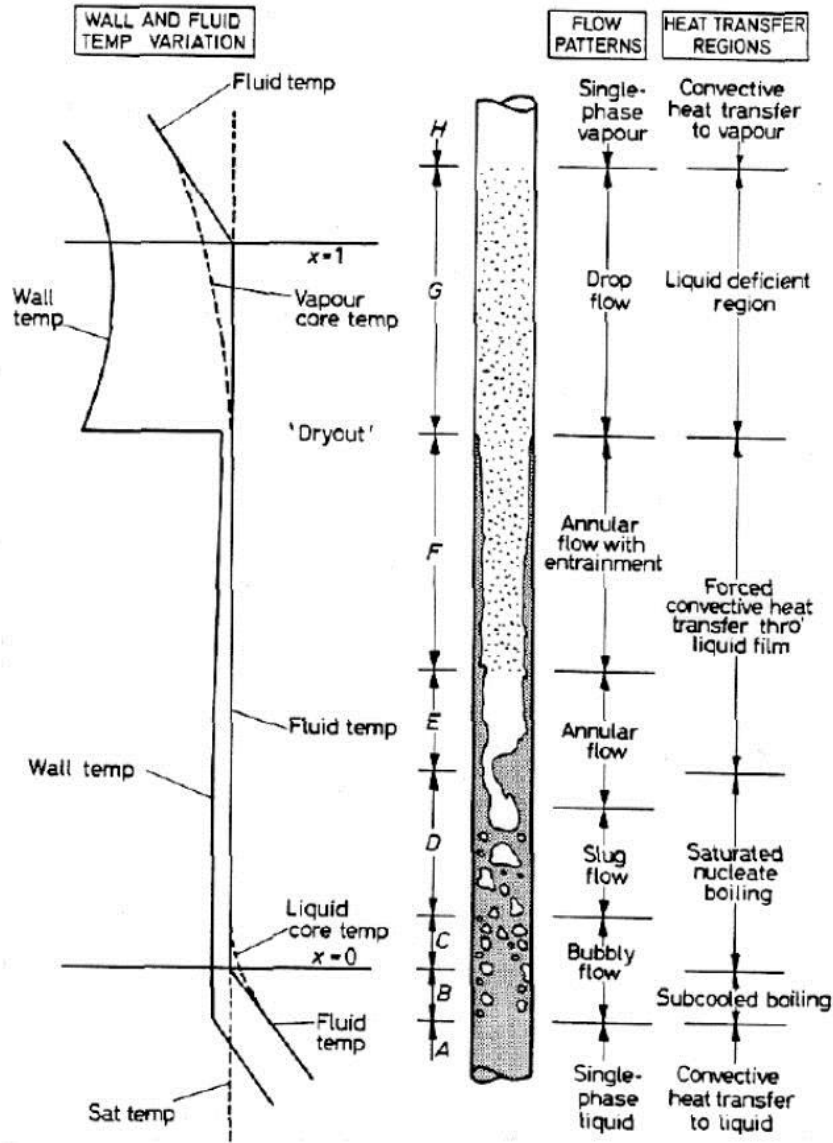


Figure 11: Different flow regimes for forced convection flow boiling in circular tubes as described in [21]. The image is reproduced from [21].

interfacial dynamics between the two phases are normally not modeled. Because of its simplicity and computational efficiency, this method can be used in CFD coolant boiling analysis.

3. Liquid and vapor phases are solved separately using two sets of governing equations. Mass, momentum, and energy transfer between the two phases are explicitly modeled. When the size of vapor bubbles is smaller than the size of computational mesh, the boundary

between the two phases cannot be predicted and the interactions between phases are calculated based on the locally estimated bubble size and amount. When the bubble size becomes larger than that of the mesh, the phase boundary can be simulated in detail with the help of an interface treatment. This method is a more promising one in principle, even though the accuracy of the prediction relies heavily on the quality of models, while many of these models have not yet reached maturity. Compared with methods 1 and 2, the increased computational time for obtaining numerical solution in two phases with this method is significant.

4. Similar to method three, liquid and vapor phases are solved separately using two sets of governing equations. However, an exceptionally fine computational mesh is used that enables detailed bubble dynamics to be simulated directly. Phase boundaries and interactions between phases are parts of the solution rather than modeled parameters. At present, the application of this method is still limited to study the characteristic of a single vapor bubble [4]. Due to the high computational demands, this kind of method offers less immediate potential for engineering applications.

2.2. Flash cooling

Flash boiling is a rapid depressurization process in which a liquid coolant is throttled to a low-pressure environment. The partial phase change due to depressurization brings down the local temperature of surrounding liquid close to saturation temperature at the lower pressure. Consider a cooling chamber of hydraulic diameter, D_h , with heat influx of q'' as shown in Fig. 1. The coolant is injected at reservoir pressure, P_r , and saturation temperature, $T_l(P_r)$. The heat is transferred at average surface temperature T_s . For convective flow boiling, the heat flux drawn by the liquid can be express in terms of convective heat transfer coefficient, h_{conv} , as,

$$q'' = h_{conv}[T_s - T_l(P_r)] \quad (10)$$

which can be modified for flash boiling as

$$q'' = h_{fc}(T_s - T_m); T_l(P_f) \leq T_m < T_l(P_r) \quad (11)$$

$$h_{eff} = \frac{h_{fc}(T_s - T_m)}{[T_s - T_l(P_r)]} \quad (12)$$

where, P_f is the pressure in the flash chamber, T_m is the mean fluid temperature in the chamber, h_{eff} is the effective heat transfer coefficient and h_{fc} is the heat transfer coefficient of flash cooling.

It is clear that T_m will be minimum if large amount of phase-change occurs due to depressurization, with least possible temperature being $T_l(P_f)$. The relations can also be written in more detailed form along tube length x which runs from points x_1 to x_2 ,

$$q''(x, t) = h(x, t)[T_s(x, t) - T_m(x, t)] \quad (13)$$

$$q_{12} = \int_{x_1}^{x_2} h(x, t)[T_s(x, t) - T_m(x, t)] \pi D_h dx \quad (14)$$

$$h_{eff} = \frac{\int_{x_1}^{x_2} h(x, t)[T_s(x, t) - T_m(x, t)] dx}{[T_s - T_l(P_r)] \int_{x_1}^{x_2} dx} \quad (15)$$

A comparison between (10) and (13) shows that since T_m for flash cooling is lower than $T_l(P_r)$ for convective flow boiling, effective heat transfer coefficient can be higher for flash cooling if the $h_{conv} \sim h_{fc}$. This highlights the reason flash cooling should be able to provide more cooling in initial transients of pulsed cooling as opposed to steady-state convective two-phase cooling.

2.2.1. Mechanisms

Flash boiling mechanisms are not completely understood, and this state of affairs is one of the motivating factors behind this work. In the absence of porous media, the depressurization can cause high rates of homogeneous nucleation as a function of local pressure. Large pressure

gradients exist and function as evaporation fronts. Grolmes and Fauske [23] are commonly credited as the first to observe evaporation waves, finding a transition region that depends on diameter of the vessel (Fig. 12). Below a certain superheat value, only quiescent evaporation was noted to occur. Above this value, a transition region existed, in which free-surface boiling was not sustained. At superheats higher than this transition region, sustained two-phase flashing occurred. Though most studies are based on correlations without any mechanistic model to support the observations. In the presence of porous media and significant nucleation sites on the tube wall, the two nucleation mechanisms compete and thus create a complex process with different time scales and competing phase-change processes. Some of the key criteria used for pool boiling and flow boiling such as effective critical heat flux (after which vapor inhibits the cooling effect) are unknown for such transient cooling processes, and thus, researchers seek to obtain these values at an engineering scale through experiments and statistical approaches discussed in later sections.

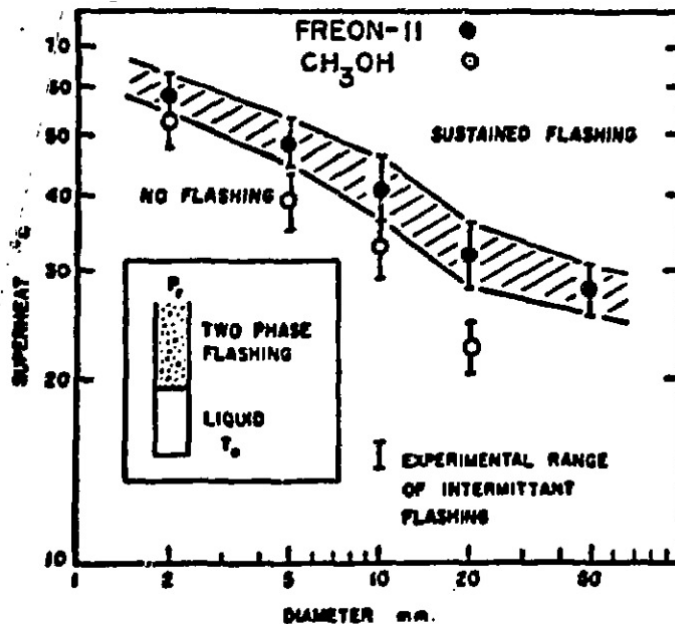


Figure 12: Phase-change transitions for evaporation waves, reproduced from [23]

2.2.2. Prior work

Previous results on an individual use flash cooling device for laser applications [7] have shown a peak effective heat transfer coefficient of about $50,000 \text{ W/m}^2\text{K}$ with the help of graphitic foam (Fig. 13). It was also observed that the peak is observed at early stage of flash cooling, thus providing a rapid response cooling of the order of 10-ms. The work included surrogate modeling to understand the effects of some parameters. However, the fluid domain was not considered in detail, and thus the information obtained cannot be directly used for different applications. The same work also utilized graphitic foams as extended surfaces for flash boiling. The graphitic foams have larger surface area and higher effective thermal conductivity at low densities. However, it was not clear if the use of graphitic foams enhanced the flash boiling process, and if it did, the magnitude of the contribution of enhanced heterogenous boiling.

2.2.3. Flash incipience and pressure undershoot

As a pressure-controlled boiling phenomenon, flash boiling, or the inception thereof, is sensitive to the pressure-controlled local liquid superheat. To better understand the underlying physical processes that drive flash discharge so a predictive model for flash can be implemented

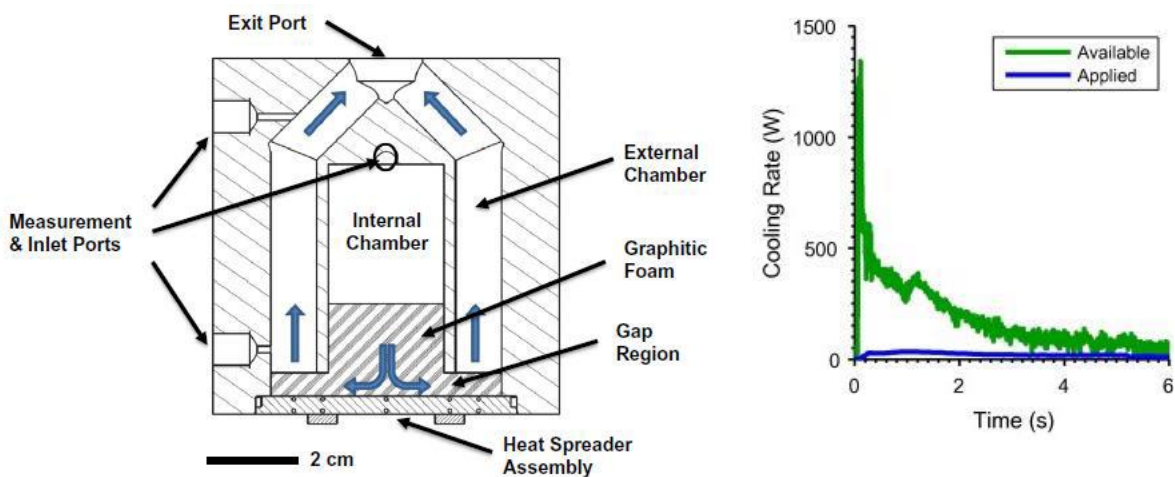


Figure 13: Test chamber and obtained cooling rate measured in previous work [3]. The peak cooling rate of flash cooling is very high and acts as a motivation for this work. The images are reproduced from [6].

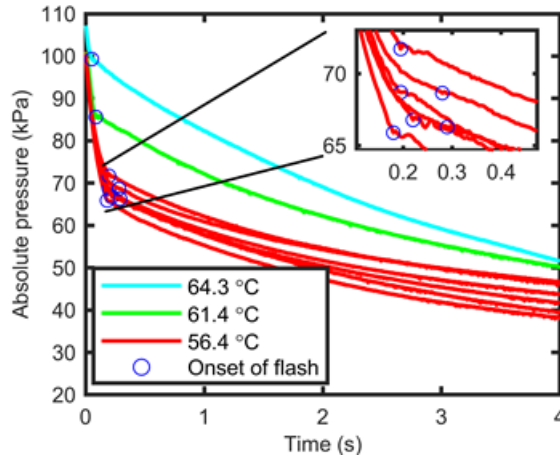


Figure 14: Comparison of depressurization rates and onsets for various average initial temperatures corresponding to different heat inputs.

in real systems, the superheat criterion for nucleation is addressed. The goal of the experiments described in [18, 24] is to provide insight into flash incipience conditions so that models for flash cooling can be developed. The experimental setup (Fig. 14) to conduct pressure wave propagation measurements is similar to that of [25].

A long, vertical copper tube is filled with methanol and subject to various depressurizations, whose magnitudes are captured with pressure gauges placed at the top and bottom of the tube. Thermocouples are also placed on the outside of the tube to measure changes in temperature associated with flash boiling. Further details can be found in [18]. The results are described in Fig. 15 with onset pressure indicating the incipience of flash.

Pressure is not a static quantity, but a dynamic one that changes with time and location during a flash process, as pressure waves propagate once a system is initially depressurized to initiate flash boiling. Here, background on pressure wave propagation is presented. As a pressure wave traverses, for instance through a tube, it was observed that at the location at the far end of the tube away from the surface closest to the initial depressurization the local pressure briefly dropped to a value below that prescribed by the initial depressurization. This phenomenon is



Figure 15: Horizontal tube setup for pressure wave propagation experiments, reproduced from [18].

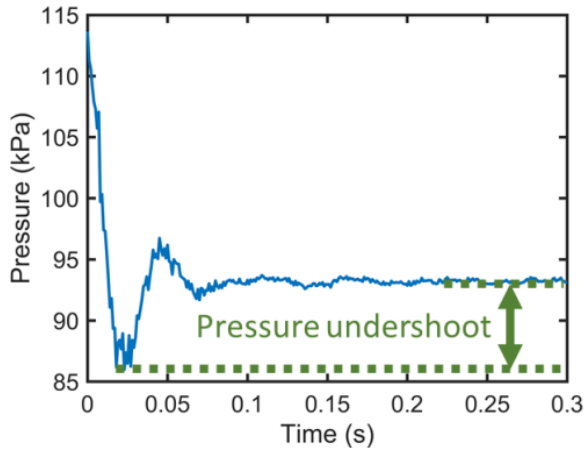


Figure 16: Demonstration of pressure undershoot, reproduced from [18].

denoted as pressure undershoot, and an example of pressure undershoot in a tube is shown in Fig. 16.

This undershoot phenomenon, as a result of the reflected pressure wave at the end of the tube, has also been observed experimentally in prior work. [25] reported pressure undershoots of up to 50% for an air-water mixture in a 2.1 m long vertical tube.

This phenomenon has some important implications. If local pressure within a system can achieve a minimum at a specified location, then localized flash boiling becomes possible. Also, the presence of the pressure undershoot reinforces the idea that only a partial initial depressurization is needed for flash; the undershoot will deliver a further local reduction in pressure that brings the working fluid to conditions suitable for bubble nucleation.

2.3. Numerical techniques for transient two-phase flow

2.3.1. Multiple-bubble-level

A particular set of research has focused on direct numerical simulation of discrete bubbles for understanding dynamic and heat transfer associated with single and merging bubbles [4] [26]. These transient codes at the bubble-level have been able to predict nucleate pool boiling phenomenon. However, they are computationally prohibitive for flash cooling since it is a combination of different boiling mechanisms and involves large pressure gradient.

A mesoscopic averaging approach is described in [27] that considers pure homogeneous nucleate boiling for flash processes, and thus follows the equation for critical radius and rate of

nucleation mentioned above. It considers small cube element of length x_e as shown in Fig. 17. The element is much smaller than the macroscopic observation scale but about twice the size of critical bubble radius. The temperature within the element is assumed to have an iteratively known average temperature (T_{avg}). The addition of conductive heat to the element is denoted by q_d and the amount of energy consumed to generate vapor is shown by q_c . The vapor generation rate within the element is described as,

$$\Gamma(t) = \int_0^t \left\{ 4\pi r^2 \frac{\partial r(t, t')}{\partial t} \rho_v \right\} J(T_l(t')) dt' \quad (16)$$

and $\frac{\partial r}{\partial t}$ is evaluated from a bubble growth model. The complete energy equation over the element gives effective change of T_{avg} . According to the approach, the onset of flash boiling occurs when $\frac{\partial T_{avg}}{\partial t} \leq 0$ as shown in Fig. 18.

Another study looked at flash-boiling enhancement of spray with focus on only heterogeneous nucleate boiling due to injected air bubbles [28]. The discrete model was like the previous paragraph but for a droplet. The study took fuel properties iteratively from the NIST database.

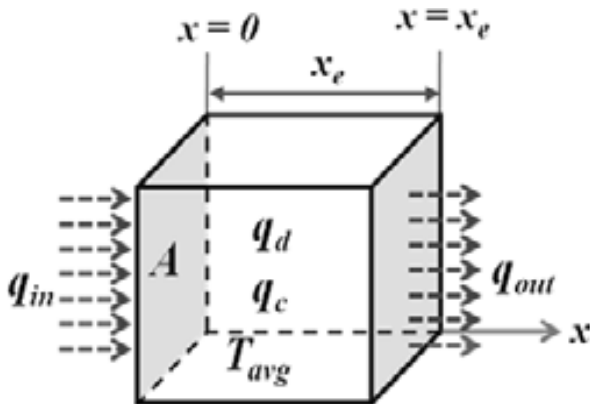


Figure 17: A representative volume element for the mesoscopic approach for pure homogeneous boiling.

Reproduced from [27].

2.3.2. Continuum-level

2.3.2.1. Volume averaging

Volume averaging techniques for two-phase boiling and multi-phase mixtures are discussed in [29]. These approaches simplify the governing equation with the help of volume averaging of properties over small volumes. A detailed derivation of volume

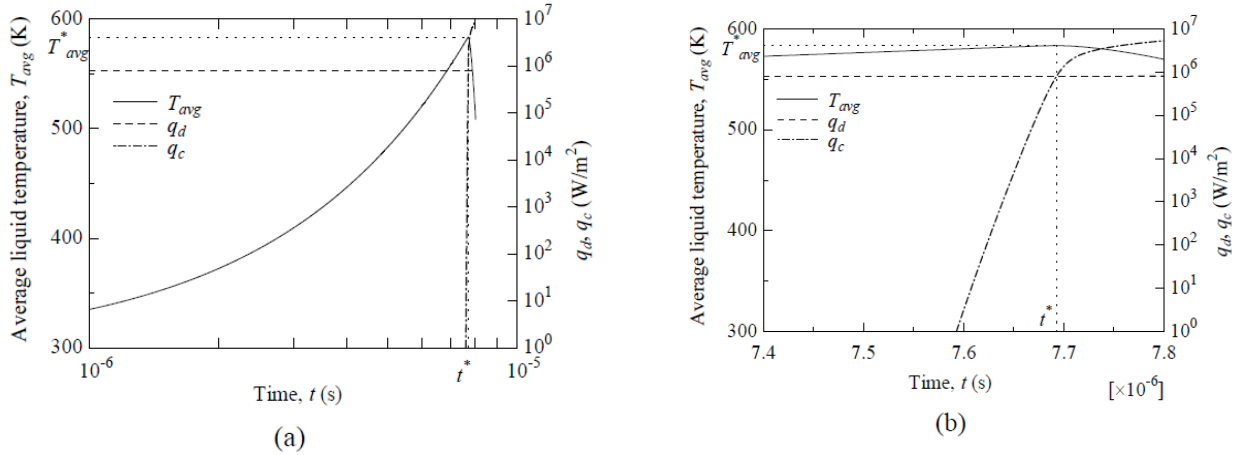


Figure 18: (a) Simulation results to show onset of flash boiling. (b) zoomed in view near the critical time. Figure 18 and b are reproduced from [27].

averaging for single phase fluid flow through porous media based on different assumptions (like porous media flow equations) is available in [29]. The equations for multi-phase systems with homogeneous flow assumptions are also included.

2.3.2.2. Volume averaging theory

Volume averaging theory (VAT) is a hierarchical modeling method to connect lower-scale governing equations to upper-scale averaged equations [30], [31]. It was developed originally for steady flow through porous media and requires closure of the complicated integro-differential equations. Closure equations can be obtained by theoretical assumptions, numerical simulations, or experimental methods. As seen in Fig. 19, VAT reduces modeling difficulties by eliminating the need for finite element or finite volume method. A properly closed VAT problem can provide an overall framework while saving computation costs. However, the code for VAT must be modified in order to accommodate non-equilibrium unsteady form of the equations. Also, two-phase flow through porous media has not been developed in VAT yet.

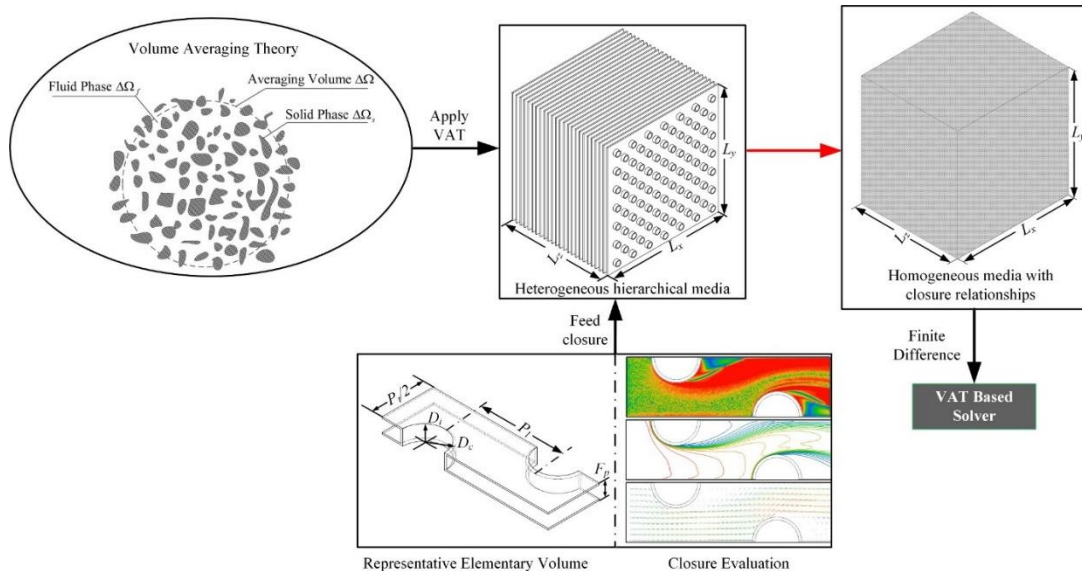


Figure 19: VAT Based Modeling workflow as described in and reproduced from [31].

2.3.3. System-level

2.3.3.1. Rocket engine transient models (0-D or 1-D)

Many zero- or first-order system-level transient models have been developed for rocket engines. A helpful review of existing transient codes is included in [32]. Typically, the ignition process of a liquid rocket engine involves non-linear interactions between multiple engine components (resistance, turbopump operation, heat transfer, phase change, and combustion etc.). Although the qualities of a thorough and in full-depth analysis may be desirable in the study of specific single components and scenarios, for complex, multi-component systems, the long computational times become overwhelming. Furthermore, the physical properties of liquid propellants and combustion products in such systems vary widely and rapidly. Various tools have been developed to simulate the transient behavior of rocket engine systems. In 1990, the Liquid Rocket Transient Code (LRTC) was developed as an in-house code of The Aerospace Corporation. The Rocket Engine Transient Simulator (ROCETS) was designed and developed during the 1990s by Pratt & Whitney for NASA-MSFC; it allows for cost effective computer predictions of liquid

rocket engine transient performance. Another powerful tool created in the United States is the Generalized Fluid System Simulation Program (GFSSP) for modelling cryogenic fluids in a complex circuit [33]. However, most of these tools are restricted in terms of access and thus, detailed understanding of the equations being solved is limited.

EcosimPro [34] is a modelling and simulation tool for modeling 0D or 1D multidisciplinary continuous-discrete systems and any kind of system based on differential-algebraic equations (DAE) and discrete events. Its uniqueness lies in the GUI design that makes it a visual block programming tool like National Instruments' LabVIEW or Matlab's Simulink software. In EcosimPro, multidisciplinary physical models are grouped into libraries, and each component can have its own set of physical models. These libraries are collectively termed as toolkits based on specific applications. The software has also incorporated optimization and design tools over the years. It also allows for external integration with Microsoft Excel and programming languages like Matlab and Python. Another advantage is the availability of enough published articles that provide the basic set of equations or models being solved for the components.

The most relevant toolkit with current work is the European Space Propulsion System Simulation (ESPSS) library that is developed for modelling rocket and satellite propulsion systems [35]. The relevant features of ESPSS includes:

- a. Fluid properties for single or two-phase fluids evaluated based on different models. For real properties, it has an interface with REFPROP database [36]. The capability of integration with python would allow use of CoolProp [37] in an equivalent manner. Ideal state models are also available. The details of individual property calculations can be found in [32].
- b. Pressurization systems including priming processes, tank behavior, heat transfer, mechanical or electronic pressure regulators, etc.

- c. Fluid networks with detailed simulation of transient phenomena due to inertia (water-hammer), heat exchange (radiators) or control processes.
- d. Models for turbomachinery, valves, and other flow devices.
- e. Homogeneous two-phase flow modeling for chambers.

The components in ESPSS are classified into two categories: capacitive (C) and momentum (M) elements. The capacitive elements have integrated mass, momentum, and energy equations whereas, momentum equations do not solve energy equations and are used to connect capacitive elements. For example, volumes and heat exchangers are C elements but junctions and valves are M elements. Similarly, pipes, tubes and nozzles are considered 1D components with C element discretization. The M and C elements both include inertial terms in the respective equations.

An example of a tube with an area-varying non-uniform 1D mesh is included (Fig. 20).

The conservation equations for the tube are as follows:

$$\text{Mass conservation: } A \frac{\partial \rho}{\partial t} + \frac{\partial(\rho v A)}{\partial x} = -\rho A k_{wall} \frac{\partial P}{\partial t} \quad (17)$$

$$\text{Momentum conservation: } A \frac{\partial \rho v}{\partial t} + \frac{\partial[(\rho v^2 + P)A]}{\partial x} = -\frac{1}{2} \frac{d\xi}{dx} \rho v |v| + P \left(\frac{dA}{dx} \right) \quad (18)$$

$$\text{Energy conservation: } A \frac{\partial(\rho E)}{\partial t} + \frac{\partial(\rho v H A)}{\partial x} = \left(\frac{d\dot{Q}_w}{dx} \right) + \rho g v A \quad (19)$$

The set of equations is closed by thermodynamic equations of state from the fluid property libraries. The term k_{wall} represents the wall compressibility which can be modeled to incorporate the effects of reflected pressure waves in case of non-equilibrium stoppage of the flow. The term ξ represents a source term for incorporating the friction effects into the momentum equation. This

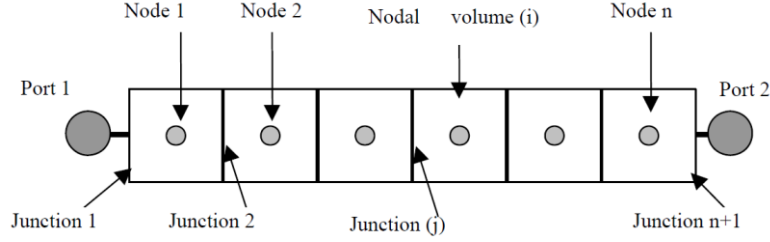


Figure 20: Discretization within a pipe in EcosimPro for 1D analysis. The image is reproduced from [32].

can be obtained with the help of multiple correlations. In the energy equation, the source \dot{Q}_w represents the heat transfer interaction with the wall:

$$\dot{Q}_w = h dx [average(T_{fluid} - T_{wall})] \quad (20)$$

where h is the overall heat transfer coefficient, dx is the distance between two nodes and $average(T_{fluid} - T_{wall})$ represents average temperature difference over the two nodes. The overall heat transfer coefficient is expressed in terms of different correlations.

The system-level approach in ESPSS thus utilizes 0D or 1D geometry and simplified equations to invest computational resources into finer time resolution of the equations. Some other commercial software that utilizes similar approach includes SimulationX, Simulink, Transient System Simulation Tool (TRNSYS) and Wolfram Modelica. However, they do not offer libraries developed for complex two-phase flow physics.

2.3.4. Relevant statistical techniques

The complex nature of flash cooling, as discussed in previous sections, makes it computationally exorbitant to simulate full flow physics. At the same time, the time scales associated with bubble formation are much smaller than measurement techniques available in the lab. The use of equipment like ultra-high-speed camera is expensive and it limits the experimental variables and does not allow use of materials (like metal tubing) that are practical for applications. It cannot be used for porous media flows as well. Thus, this section proposes use of statistical approach along with experiments and/or simulations to circumvent the limitations of both types of

techniques. The statistical approach can be either utilized to understand the cause-effect relationship among different parameters or it can provide adaptive nature to a known correlation. Data-driven techniques like neural networks also provide multi-layered correlations among parameters when no known physical model is available.

2.3.4.1. Bayesian inference:

Bayesian inference is a method of statistical inference in which Bayes' theorem is used to update the probability for a hypothesis as more evidence or information becomes available [38]. Bayesian inference is an important technique in statistics, and especially in mathematical statistics. Bayesian updating is particularly important in the dynamic analysis of a sequence of data. The details of Bayesian inference techniques are not included but a general sense is provided here. The technique assumes a number for a quantity with a large degree of disbelief or error. This assumed quantity and its disbelief is updated with every observation that is made. The approach can prove excellent in understanding cause-effect relationship among different variables in a system. Another advantage is that it provides an estimated range of error in prediction of every unknown. A Bayesian approach combined with a clever design of experiments technique can prove vital for this work. An already running code of the technique on Jupyter notebook is available within the research group. The model can be adjusted to minimize the bias errors obtained in the measurements and with more work might help to reduce the lagging errors in experimental data.

2.3.4.2. Data assimilation – Kalman filter:

Data assimilation techniques bridge the statistics with active control, and thus are chosen for run-time control of complex systems. Kalman filter is the most common data assimilation technique and is extensively used for estimation of linear differential equations [39]. Kalman filter works by updating a known low-order physical model with every time-step. Thus, the model is

used to predict state variables in a dynamic system and reduce the reliance on scarcely located sensors on real-time applications. Since, Kalman filter works on a reduced order version of physical model, for a complex flow physics with many variables, it may be a better choice over the Bayesian framework which can get computationally intensive especially in transient situations.

The shift from traditional efforts to extend Moore's law by reducing the transistor size has elicited significant advancements in electronics packaging including 3D stacked and wafer-level packaging techniques. These next-generation techniques involve dense heterogeneous integration and push the thermal limits of materials and systems. New cooling architectures are being developed to provide necessary heat extraction from such packages. Temperature estimation is critical for packaging design. However, design complexity in the third dimension and the variety of materials involved present challenges to estimate temperature profiles from limited sensor data and to predict temperature profiles throughout the packaging. Temperature sensing and prediction is critical to task scheduling of processors and regulation of limited cooling resources. Thermal simulations for developing new designs with high-fidelity, physics-based solvers, such as ANSYS Icepak, require high computational overhead especially due to the disparate length scales involved, and real-time prediction methods based on linearized temperature model and/or compact thermal modelling struggle to predict hotspots accurately in geometrically complex architectures.

Adaptive estimation methods, including the Kalman filter (KF), have been shown to perform well for simple packaging designs. The most common approach to reduce computational cost is to utilize reduced order modelling (ROM) with KF [39]. However, KF solves linearized equations, and even with ROM, it would require high computational overhead to maintain accuracy with new packaging structures. A temperature estimator and predictor based on ensemble Kalman filter (EnKF) can effectively handle non-linearities contained in the thermal equations.

EnKF is a data assimilation technique that has been used in the field of meteorology and oceanography extensively and is inherently capable of handling high-dimensional nonlinear systems and high volumes of measurement data [40]. Recently, EnKF has been used successfully to estimate the separated flow about a wing from available surface-based sensors, and the concept is extended here to obtain temperature profiles across electronic packages. The unscented Kalman filter (UKF) is another approach that promises better accuracy than EnKF with similar computational time. Its main advantage is that it uses fewer ensemble members since these members are strategically chosen at each iteration. It does, however, require that the state's covariance matrix be propagated along with the state itself, and this can be problematic if the state is exceptionally large. A software framework is created here to execute these three methods for thermal management of packaging and provide a comparison of computational cost and accuracy of hotspot prediction for a 3D stacked package and a wafer-level package.

2.3.4.3. Deep neural network (DNN):

Deep neural networks are multi-layered, multi-variate techniques that manage substantial amounts of data. It is a useful technique when the amount of data is large and correlation between distinct factors is unknown. Some DNN techniques are now informed by physical model like Kalman filter and so with enormous amounts of data – it produces result that is equivalent to a combination of both the above techniques. Even though there are several unknowns in a detailed two-phase flow in porous media and flash cooling, the amount of data generated may not be enough to choose DNN.

2.4. Explored methodologies

Flash cooling is a complex process inherently involving different mechanisms of nucleation, an evaporation front, and possibly additional interactions with porous media. A flow

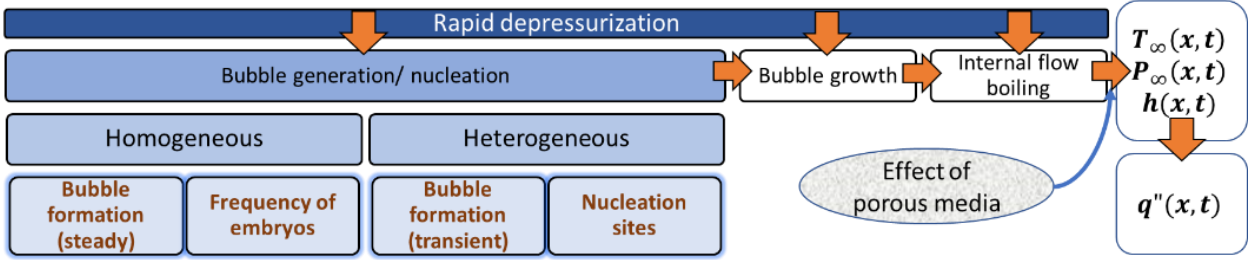


Figure 21: Hierarchical mechanistic study for flash cooling with rapid depressurization playing a significant role.

chart of dominant effects at different size and time scales is shown in Fig. 21. It is evident that a full computational analysis cannot be achieved considering the difference in the scales and the complexity of physics. Multiple routes are explored in this chapter.

2.4.1. Non-equilibrium mechanistic models – theory and simulations

A first step for deeper understand of flash cooling is to modify existing mechanistic models to understand the effect of non-equilibrium force balance and depressurization, estimate their relative effects and make corresponding simplifications. From a fundamental standpoint, liquid-vapor phase change is inherently unstable and governed by so-called spinodal curves (one for each phase) in the saturated liquid-vapor regime, leading to extreme mathematical complexity in modelling of phase-change processes (Fig. 22). The grey shaded portion is the region where a liquid can be superheated and remain as liquid because it satisfies criterion of mechanical stability. Criterion of thermal stability is satisfied when volumetric specific heat is positive ([19], Eq. 5.42, 5.43). When a liquid a saturation temperature T_{sat} is heated at saturation pressure, it goes in the yellow region – called the superheated liquid. The green region indicates the region of depressurization. Most nucleation theories are developed around constant pressure within the yellow region. However, it can be possible to run along a constant temperature line inside the spinodal zone.

For example, (5) for homogenous bubble nucleation must be modified for depressurization effects in a recursive manner,

$$r_c(x, t) = \frac{2\sigma(T_\infty(x, t))}{P_{sat}(T_\infty(x, t)) \exp\left[\frac{\{P_l(x, t) - P_{sat}(T_\infty(x, t))\}}{\rho_l(T_\infty(x, t))RT_\infty(x, t)}\right] - P_l(x, t)} \quad (21)$$

and the properties must be evaluated using NIST database to close the equation (CoolProp with Jupyter notebook is the current choice). Since the current work seeks to develop functional understanding of flash cooling in order to optimize it for high-performance systems, this path is not chosen, but it may be followed in some collaborative projects.

2.4.2. Mesoscopic approach with machine learning

The simulations/experiments can be done on a single tube flash cooling chamber and obtained understanding and data will be used to optimize the cooling for later applications. The overall methodology further incorporates two ideas: Continuum- level details are necessary for application purposes, and microscopic level details are necessary to understand the factors influencing flash cooling.

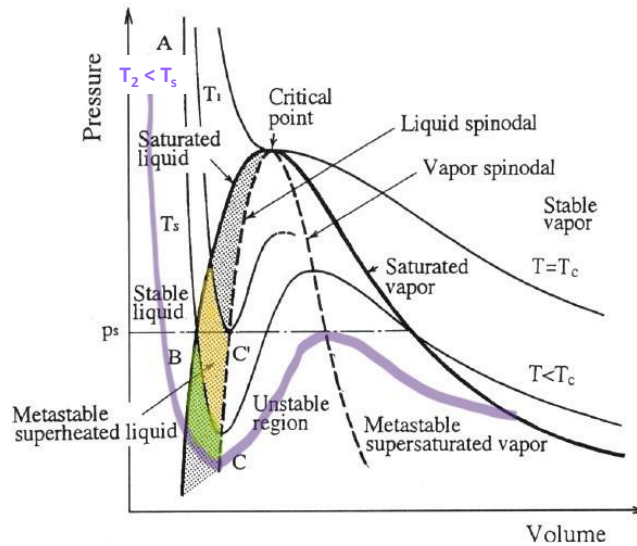


Figure 22: Spinodal curves for liquid-vapor, overlay with a $T_2 < T_s$ curve. The yellow zone between T_1 and T_s represents the superheating required to achieve phase change. The green zone represents depressurization leading to superheated liquid state. The image is adapted from [19].

The continuum understanding of flash cooling should provide information about the state of the system in small, discretized domains. The experiments can only give us the measurements of partial set of state variables at a few locations across the system (Fig. 23). Thus, to obtain $Q(x, t)$ of the flash cooling tube, it is necessary to statistically fit certain flow equations or correlations. The first macroscopic step to study flash cooling is to create a time-averaged steady-state analysis of the thermodynamic states of all system components to provide a good starting point for experimental testing (Fig. 24).

For the physical models, note that the assumption of homogeneous flow is very restrictive, and in fact accurate only under limited conditions (e.g., dispersed bubbly flow, mist flow). In general, a significant slip between the two phases is present, which requires the use of more realistic models in which v_v and v_l are not equal.

A conceptual progression for homogeneous flow boiling for porous media modeling is as follows:

1. Assumed properties for homogenous flow boiling: All the properties are weighted mean of individual values of liquid and vapor properties. The weight is decided by void fraction (or liquid saturation).

$$\alpha = 1 - s \tag{22}$$

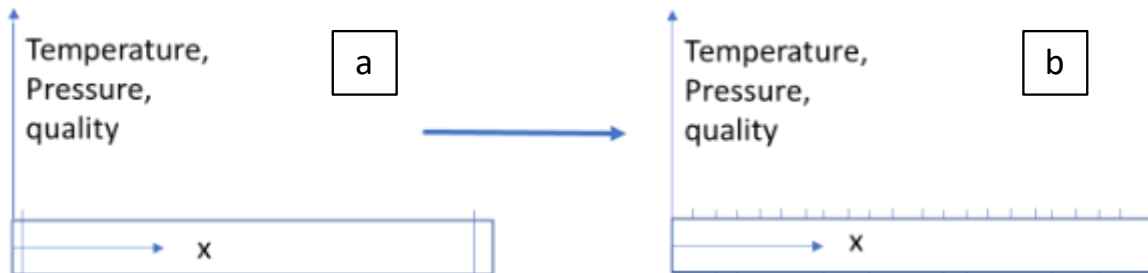


Figure 23: (a) Experimentation is limited by several factors to measure state parameters only at certain locations. (b) Desired target distribution of known state properties for controlled cooling is shown.

In case an instantaneous individual cross-section is considered, void fraction depends on the area average. If volume averaging is being performed for the entire discretized domain, then void fraction is defined by volume-based weighting:

$$\alpha = \frac{A_v}{A_t} \text{ or } \frac{V_v}{V_{total}} \quad (23)$$

Thus, if v_v, v_l are superficial velocities of vapor and liquid, and the homogeneous assumption ($v_v = v_l$) is valid, then the intrinsic phase-averaged velocity v is

$$v = \frac{\rho_v v_v + \rho_l v_l}{\rho} = \frac{\rho_v + \rho_l}{\alpha \rho_v + (1 - \alpha) \rho_l} v_l \quad (24)$$

Other properties are weighted similarly.

2. Homogeneous flow equations for two-phase flow without porous media looks similar to single fluid flow through a tube,

$$\text{Mass conservation: } \frac{\partial \rho}{\partial t} + \frac{\partial(\rho v)}{\partial x} = 0 \quad (25)$$

$$\text{Momentum conservation: } \frac{\partial(\rho v)}{\partial t} + \frac{\partial(\rho v^2)}{\partial x} = -\frac{\partial P}{\partial x} - \frac{1}{2} \frac{d\xi}{dx} \rho v^2 \quad (26)$$

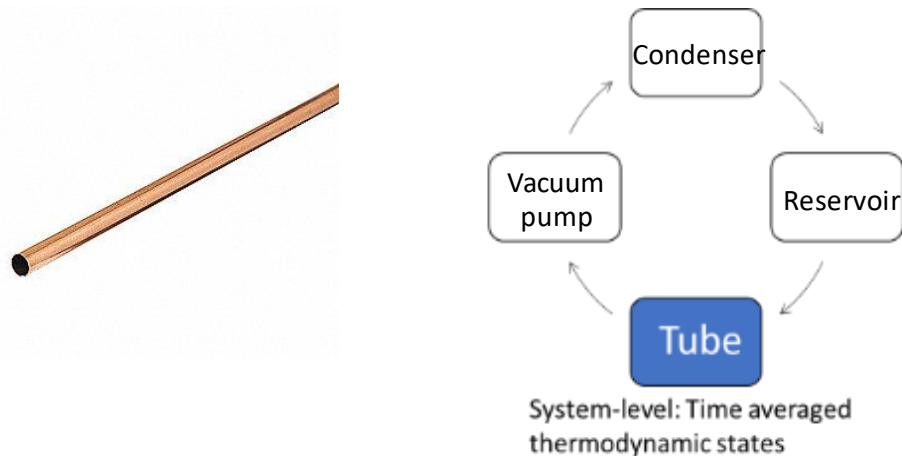


Figure 24: System-level analysis with a single diameter tube being the component of interest. First step is to perform time-averaged steady state estimates.

$$\text{Energy conservation: } \frac{\partial(\rho h)}{\partial t} + \frac{\partial(\rho v h)}{\partial x} = -k \nabla^2 T + \frac{dQ_w''}{dx} \quad (27)$$

where, ξ is a friction factor which allows different x-dependent functions to evaluate the frictional losses. Gravitational and other body forces are ignored. Cross-sectional area, A , is assumed to be constant throughout the flow field. In the energy conservation equation, enthalpy is total enthalpy which is a summation of static enthalpy, h' , and kinetic energy,

$$h = i + \frac{1}{2} v^2 + \frac{P}{\rho} = h' + \frac{1}{2} v^2; h' = \frac{(\rho_v \alpha h'_v + (1 - \alpha) \rho_l h'_l)}{\rho} \quad (28)$$

The viscous dissipation term is neglected in the energy equation, and k is a phase-averaged thermal conductivity defined as, $k = \alpha k_v + (1 - \alpha) k_l$. The heat flux added from the wall is considered an x-dependent source term $\frac{dQ_w''}{dx}$.

3. The primary unknown in the above set of equations is the pressure gradient, $\frac{\partial P}{\partial x}$.

Several different assumptions and correlations have been developed over the last few decades. For example, in Professor Dhir's course on "Boiling and Condensation" at UCLA, one of the considered models was

$$\frac{dp}{dx} = \frac{\frac{4}{D_h} f_{tp} \left(\frac{1}{2} \rho v^2 \right) + \rho^2 v^2 v_{l0} \frac{d\bar{x}}{dx} + \rho g}{1 + \rho^2 v^2 \frac{dv_v}{dP}} \quad (29)$$

where D_h is the hydraulic diameter of the flow tube, f_{tp} is the friction coefficient for two-phase flow which is approximated from friction coefficient of liquid/vapor with other correlations [41], v_{l0} is the velocity if only liquid was flowing through the total area, and \bar{x} is the quality of mixture as function of α . Such correlations provide an approximate start to these equations for simulations. However, these are not universally agreed upon, and depending on different flow situations several forms are presented over the years. Once the pressure gradient is solved in the momentum

equation, pressure and density serve as the basis for calculation of void fraction and thus enthalpy for the energy equation. Either an equation of state or a property table can be utilized. This work takes advantage of already established Jupyter notebook with CoolProp to obtain properties during the simulation.

4. When these homogenous equations are extended to a flow through porous media, the extrinsic phase-average velocity is modified due to the presence of porosity (ϵ) of porous media, defined as the ratio of pore volume to total volume. Assuming constant porosity through the length of the tube, ϵ , can be approximated as ratio of pore area to the total area. The modified conservation equations become:

$$\text{Mass conservation: } \epsilon \frac{\partial \rho}{\partial t} + \frac{\partial(\rho v)}{\partial x} = 0 \quad (30)$$

$$\text{Momentum conservation: } \epsilon \frac{\partial(\rho v)}{\partial t} + \frac{\partial(\rho v^2)}{\partial x} = -\epsilon^2 \frac{\partial P}{\partial x} - \frac{1}{2} \frac{d\xi'}{dx} \rho v^2 \quad (31)$$

$$\text{Energy conservation (fluid): } \epsilon \frac{\partial(\rho h)}{\partial t} + \frac{\partial(\rho v h)}{\partial x} = -k \nabla^2 T + \frac{dQ_w''}{dx} + Q_{sf} \quad (32)$$

$$\text{Energy conservation (solid): } (1 - \epsilon) \rho_s \frac{\partial h_s}{\partial t} = -k_s \nabla^2 T - Q_{sf} \quad (33)$$

$$\text{Energy conservation (total): } \epsilon \frac{\partial(\rho h)}{\partial t} + (1 - \epsilon) \rho_s \frac{\partial h_s}{\partial t} + \frac{\partial(\rho v h)}{\partial x} = -k_{eff} \nabla^2 T + \frac{dQ_w''}{dx} \quad (34)$$

The above equations are written with the assumption that porosity remains uniform throughout the domain. Here, ξ' is a modified frictional force equation for two-phase flow in porous media and correlations will be developed to solve for it. In the energy equation, fluid temperature is considered homogeneous with the solid temperature ($T_v = T_l = T_s$). The amount of heat transferred from solid to liquid phase is written as Q_{sf} and is added to the liquid phase energy equation and consequently removed from solid phase energy equation. However, this is inherently

removed while combining the two equations. The effective thermal conductivity for conduction is then defined as,

$$k_{eff} = k_s(1 - \epsilon) + \epsilon k = k_s(1 - \epsilon) + \epsilon[\alpha k_v + (1 - \alpha)k_l] \quad (35)$$

5. The solution of these equations, similar to internal flow boiling without porous media, start with an approximation for pressure gradient. However, for porous media Darcy's law (Eq. 13) can provide an approximate pressure gradient,

$$\frac{\partial P}{\partial x} = \frac{v\mu}{K} \quad (36)$$

where K is the permeability for the homogenous fluid and μ is the effective viscosity (multiple models available [41]). If an effective permeability is known through experiments, the equation can be solved. However, calculation of permeability for two-phase flow is property dependent and thus several models [42] exist.

$$K(\text{two} - \text{phase}) = \text{function}(K_{rl}, K_{rv}, \mu_l, \mu_v, \alpha, \epsilon, \dots) \quad (37)$$

Some experimental work [43] is also reported to understand the relation of single-phase and two-phase (non-boiling) permeability with pore geometry of porous media and packed beds. Several extensions to Darcy's law are available for modeling of pressure gradient and they will be explored in the further in this work. Similar to the homogeneous flow assumption, these equations can be derived for separate flow phase flow model as well. However, this approach requires more computation, and the derivation is not followed here.

One of the feasible options is to utilize data assimilation technique discussed above with a Kalman filter, a known transient physical model (linearized) with unknown parameters (approximated) is inserted. At every time step, the filter creates a prediction of the current step from previous step information, compares it with sensor measurement and then modifies the parameters according to the difference between the two. This approach provides an accurate

predictive model with known uncertainties in measurements and the predictive model. If an equation cannot be linearized, an extended or unscented Kalman filter will be used. This approach can be explained with the help of Fig. 25, where the flash cooling experiments provide data to improve the physical model. However, if an approximate physical relationship is unknown between observable and input parameters, the Kalman filter model will be insufficient to accurately predict unobservable states. The Bayesian framework provide more accurate cause-effect relationships but at the cost of computing resources. Some of the key parameters that will help improve the prediction include, length, diameter and material of the tube, location of heater and thermocouple sensors, pressure and heat load conditions, porosity, and location of porous plug.

Looking at the model above, many unknown variables in correlations can be identified that must be found with the help of data. The first step is to identify key parameters that can be correlated with the physical model – transient two-phase homogenous flow through porous media.

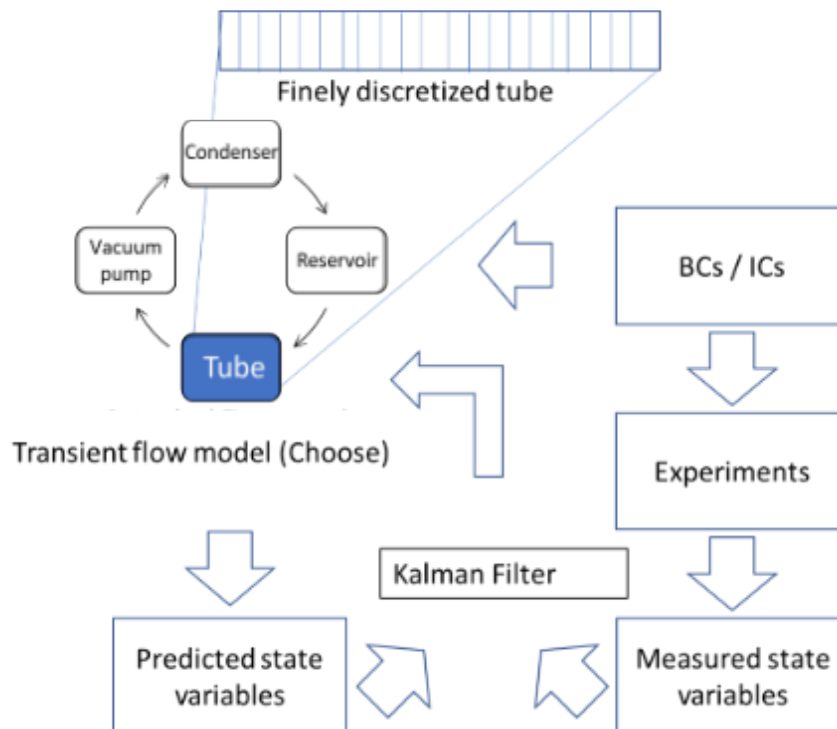


Figure 25: Kalman filter to improve transient model for single tube analysis.

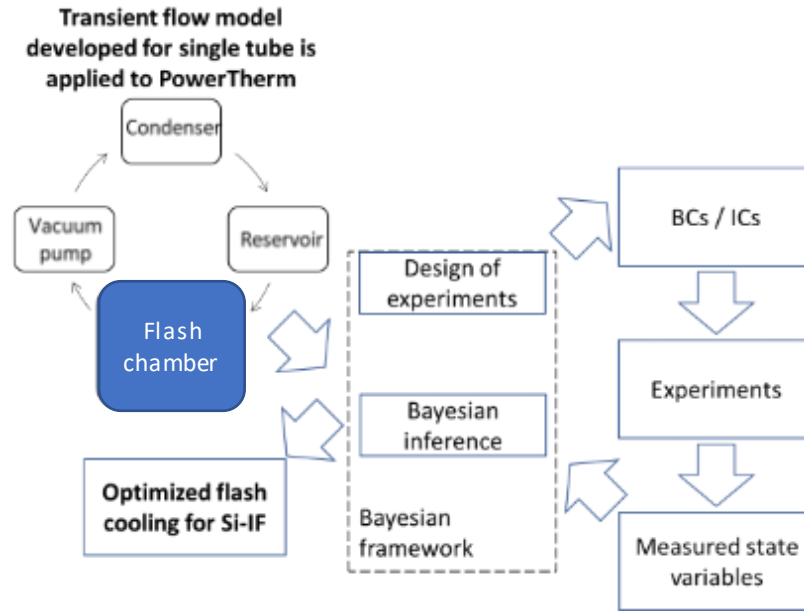


Figure 26: The Bayesian framework will help optimize the flash cooling process for cooling architecture once a Kalman filter modified model for single tube is available.

This model will be used with a Kalman filter to provide an updated transient model. This model will be insufficient to interact with physical parameters that do not directly appear in the set of equations being solved. This is where the Bayesian approach come into play (Fig. 26). The goal is to utilize the model created from a single tube and extend it to complex structures and improve the models for the specific architectures with the help of Bayesian approach.

2.4.3. System-level surrogate modeling

A surrogate model is an engineering method used when an outcome of interest cannot be easily measured or computed, so a model of the outcome is used instead. Most engineering design problems require experiments and/or simulations to evaluate design objective and constraint functions as a function of design variables (Fig. 27). For flash cooling, the complex physics associated with understanding transient cooling would require large amount of experimental data and computing power beyond the limits of laboratory environment. Thus, constructing approximate models, surrogate models, which mimic the behavior of the simulation/physical

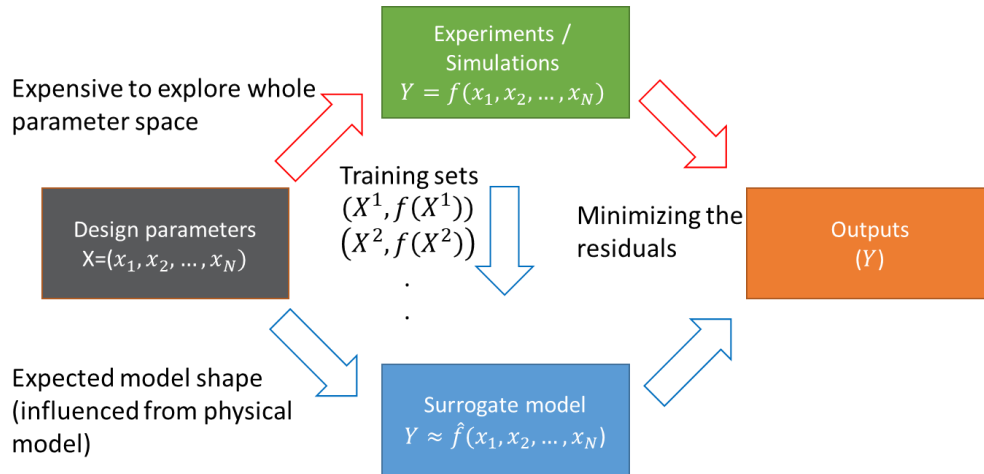


Figure 27: Typical surrogate model workflow to develop an engineering model from experimental or simulation data

model as closely as possible while being computationally cheap(er) to evaluate. When only a single design variable is involved at a time, the process is known as curve fitting.

A detailed workflow for the analysis in this work and the parameter space is explored in Chapter 6.

2.5. Empirical limits for cooling Si-IF

Silicon Interconnect Fabric (Si-IF) described in section 1.2 is the primary application for which several standard cooling options are considered during preliminary design. The analysis is done using empirical correlations described in [44], Chapter 3. The following assumptions are utilized to estimate the ideal maximum cooling provided by different cooling scenarios:

- Steady-state analysis with constant and uniform heat flux over the base of heatsink.
- The die surface temperature, T_s , is 85 °C, and ambient temperature of the fluid, T_∞ , is 25 °C.
- Ideal heat spreader and heat sink base with zero thermal resistance ($R_{heatsink,base} \sim 0$).
- Si-IF is a 300-mm silicon wafer
- Permissible outlet temperature for air and water is 45 °C.

For the analysis with pin fin geometries, the following additional assumptions are considered:

- Constant and uniform base temperature for all fins, $T_{x=0} = T_s = 85$ °C.
- Ideal condition for fins – constant fluid ambient temperature and heat transfer coefficient, h , throughout the fins.
- Pin fins are made of copper (thermal conductivity, $k_{Cu} = 400$ W/mK) with 1 mm diameter and 2 mm fin pitch.
- For water and two-phase cooling, permissible fin height, L , is 20 mm and adiabatic tip at the end of the fins ($q_{x=L} = 0$).

The total heat removal, q_t , with pin fins can be evaluated as:

$$q_t = \eta_o h A_t (T_s - T_{fluid}); \eta_o = 1 - \frac{N A_f}{A_t} (1 - \eta_f) \quad (38)$$

where, η_f and η_o are efficiencies of individual fin and overall surface respectively. The fluid temperature, T_{fluid} , is either ambient temperature for external flow, T_a , or mean fluid temperature for internal flows, T_m . The cross-section area of each individual fin, A_f , and total area of the base, A_t , are at constant base temperature, T_s . The assumed heat transfer coefficients for this analysis are typical heat transfer coefficients mentioned in ([45], Table 6.5): $h_{air-cooling} = 200$ W/m²K, $h_{single-phase,liquid} = 2000$ W/m²K, and $h_{two-phase} = 25,000$ W/m²K. The fin efficiencies are calculated for individual cases using expressions provided in ([44], Table 3.4).

The results from the calculations are presented in Table 2. The details of flow geometry are included in the description and whether cooling on the Si-IF is performed utilizing both sides or single side is also included. Another consideration for the analysis is whether the cooling solution will force use of peripheral power delivery. Peripheral power delivery is highly inefficient

for a large wafer scale solution like Si-IF and thus, the cooling solutions that limit direct power delivery to die are not preferred.

Since Si-IF platform is meant for high-performance computing requiring up to 50 kW of power over a 300 mm wafer, none of the air cooling solutions are preferred. However, for scenarios where low-powered memory and processing dies are bonded to the platform air-cooling solution can provide cooling for up to 5-8 kW of cooling. Graph applications requiring large amount of shared memory space on the Si-IF is a good example of this scenario [46]. The estimated cooling significant increases by switching to single-phase water cooling. Several different approaches are considered including variety of finned configurations, with the best practical approach as shown in Table 2. The constraints involved with power delivery in the design process involved a height restriction on the pin fins in a cooling chamber to be less than 10 mm. This allows a Si-IF with medium-power requirements to be cooled by water cooled approach with pin fins up to 13-kW of

Table 2: Empirical cooling limits for Si-IF

Representative technique	Flow description	Single-side or dual-side of Si-IF	Peripheral power delivery required? (Yes/No)	Estimated maximum cooling (kW)	Remarks	
Air cooling	Direct flow over the wafer	Single	No	1		
		Dual	Yes	2		
	Pin fins on copper base	Single	No	5		Infinite fins, $\eta_o = 0.65$
		Dual	Yes	10		
	Large (4x area) heat spreader with copper fins	Single	No	8		Infinite fins, $\eta_o = 0.75$
		Dual	Yes	14		
Single-phase water cooling	Direct flow over a copper base on the wafer	Single	No	5	Flow rate = 12 kg/s	
		Dual	Yes	10		
	Inside a large tube of 300 mm diameter	Single	No	5	Flow rate = 5 kg/s	
		Dual	Yes	10		
	Inside 40 tubes of 2.5 mm diameter	Single	No	6	Flow rate = 0.02 kg/s	
		Dual	Yes	12		
	Pin fins on copper base, large flow chamber	Single	No	16	Infinite fins, $\eta_o = 0.5$	
		Dual	Yes	32		
	Pin fins on copper base, restricted height (co-design restrictions)	Single	No	13	Finite fins with 10 mm height, $\eta_o = 0.75$	
		Dual	No	29	Infinite fins for the other side	
Two -phase flow	Pin fins on copper base	Single	No	60	Infinite fins, $\eta_o = 0.75$	
	Pin fins on copper base, restricted height (co-design restrictions)	Single	No	53	Finite fins, $\eta_o = 0.8$ (Explored further in Chapter 4)	

power [46]. However, none of these approaches discussed permits the use of Si-IF above 32-kW compared to the target requirement of at least 40-kW. Thus, two-phase cooling approaches are necessary for Si-IF as mentioned briefly in section 1.2. The height-restricted two-phase cooling chamber considered in Table 2 should provide up to 53-kW of heat flux for Si-IF. Additionally, this would allow one side of the Si-IF would be available for direct power delivery instead of peripheral delivery. Thus, this cooling structure is adopted and cohesively designed with other system constraints in Chapters 4 and 5.

Chapter 3: Continuous, pulsed flash cooling for Si-F

3.1. Flash cooling testbed

3.1.1. Methanol flow loop construction

The development of a thermal-fluid system for flash cooling is the key milestone for this work [13]. A dynamically controlled flow loop for flash cooling of high-heat-flux components has been constructed. The flow loop has been designed to be flexible and robust at various test conditions to quantify and benchmark flash cooling. The fluidic components including the test device rest on a pegboard as shown in Fig. 28. Flexible flow tubing and push-to-connect fittings are used to allow for quick changes. Most third-party components such as the pressure transducer use standard NPT fittings. Thus, Swagelok® fittings are used wherever metal NPT connections are necessary including for the copper tubes.

The testbed is dynamically controlled through LabVIEW software using a micro-controller (NI CompactDAQ) to manage the transient response of the system. A state-machine based code

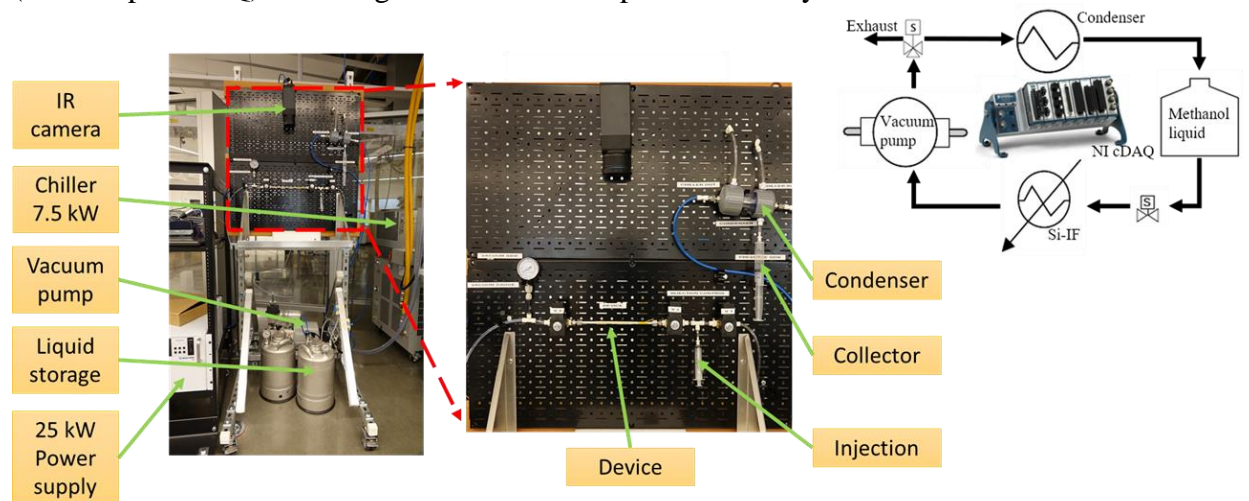


Figure 28: Flash cooling setup version 1 [13]. (a) Different components supporting the thermal testbed including the vacuum pump and the power supply are shown. (b) The zoomed-in view provides details of the preliminary flow testing. (c) A simplified workflow of the two-phase loop.

has been developed in-house to associate valve timings and data collection for the flash loop into a simple interface. Rapid thermal response of the loop is achieved with the help of flow control valves with a response time of the order of a few milliseconds. For temperature measurements, K-type thermocouples (Omega Engineering, Inc - 5TC-GG-K-20-36) and T-type surface thermocouple (Omega Engineering, Inc - SA1-TI-3M) are used. Pressure measurements are performed using a vacuum gauge ((Omega Engineering, Inc – PX419-015VI) for flash cooling tube and a pressure gauge (Omega Engineering, Inc – PX119-030GI) to monitor condenser pressure. A surface thermocouple is used for measuring the average surface temperature of silicon die. A compatible fluid temperature gauge is pending that will help to determine the exact fluid temperature.

Methanol, the current cooling fluid, is stored in a 11.4 L (3 gallon) stainless steel pressure vessel. Methanol needs to be degassed before flash boiling into the tubes to avoid artificial nucleation and to ensure repeatability. Helium was chosen to sparge because it is inert and has low solubility in liquids. The storage tank has connections for helium sparging by bubbling through the liquid methanol. The loop has extra connections to displace air in the system by helium prior to experiments. Methanol is injected into the vacuum tubes with the help of a syringe pump controlled by LabVIEW.

The vapor exiting the flash cooling tubes passes through the vacuum pump (Edwards RV3) and pushed into the condenser. The pressure in the condenser is maintained slightly higher than atmosphere. The condenser is a shell and tube heat exchanger with chilled water flowing through the tubes. The chiller can provide 7.5 kW of cooling and is maintained at 10°C. After condensation, the liquid methanol is sent back to the storage tank to achieve a fully closed loop allowing continuous operation of the system. However, for the experiments reported here, the methanol

supply tank provided adequate liquid, and closed loop condensation was not required. A Magna power supply (TSA500-50/208+HS+LXI) provides up to 25 kW of DC power to emulate the Si-IF heating. The response time for the power supply is less than 10-ms, allowing quick changes in heat loads applied to the system.

The flash cooling tests performed incorporated five sensor data for each test: Baseplate temperature (T_b), sidewall temperature (T_s), outlet fluid temperature (T_o), Vacuum pump inlet pressure (P_v) and outlet fluid pressure (P_o). Firstly, the behavior of the heater on the prototype is evaluated without flash cooling (the heat sink is already under vacuum). Before every test, the chamber is evacuated using a vacuum pump. Two conditions are imposed before the start of experiments: the chamber pressure should be less than 8 kPa, and the pressure change should be less than 0.2 kPa per minute to indicate stable conditions. The vacuum pump remains connected to the chamber throughout the experiment.

To consider cooling with flash boiling in two different applications – continuous flash cooling and single-use vapor chamber, the existing flow system was adapted to the test prototypes and experiment conditions. While different, both setups use the same principles of pressure-driven flash boiling to achieve transient cooling. More details on adapted experimental setup for vapor chamber testing is included in Chapter 7.

3.1.2. Coolant selection

The ideal working fluid has the following properties: high latent heat, high thermal conductivity, low liquid and vapor viscosities, low surface tension, and low freezing point (Table 3). Additionally, the working fluid must be compatible with the tubing in which the fluid is transported, namely copper and polypropylene. Four coolants are considered as shown in Fig. 29a.

Water and methanol provide highest latent heat of vaporization (Fig. 29b) enabling high heat flux removal at lower mass flow rates as shown in Fig. 29c. However, the vacuum pump work and evacuation time needed per pulse is extremely high for water as saturation pressure is extremely low for room temperature operations. Thus, methanol is optimal for flash cooling with fast pulses in laboratory environment.

However, methanol flow loop requires use of vacuum pump which are inefficient at higher mass flow rates. As the total heat removal requirements surpass 15 kW, the methanol coolant use

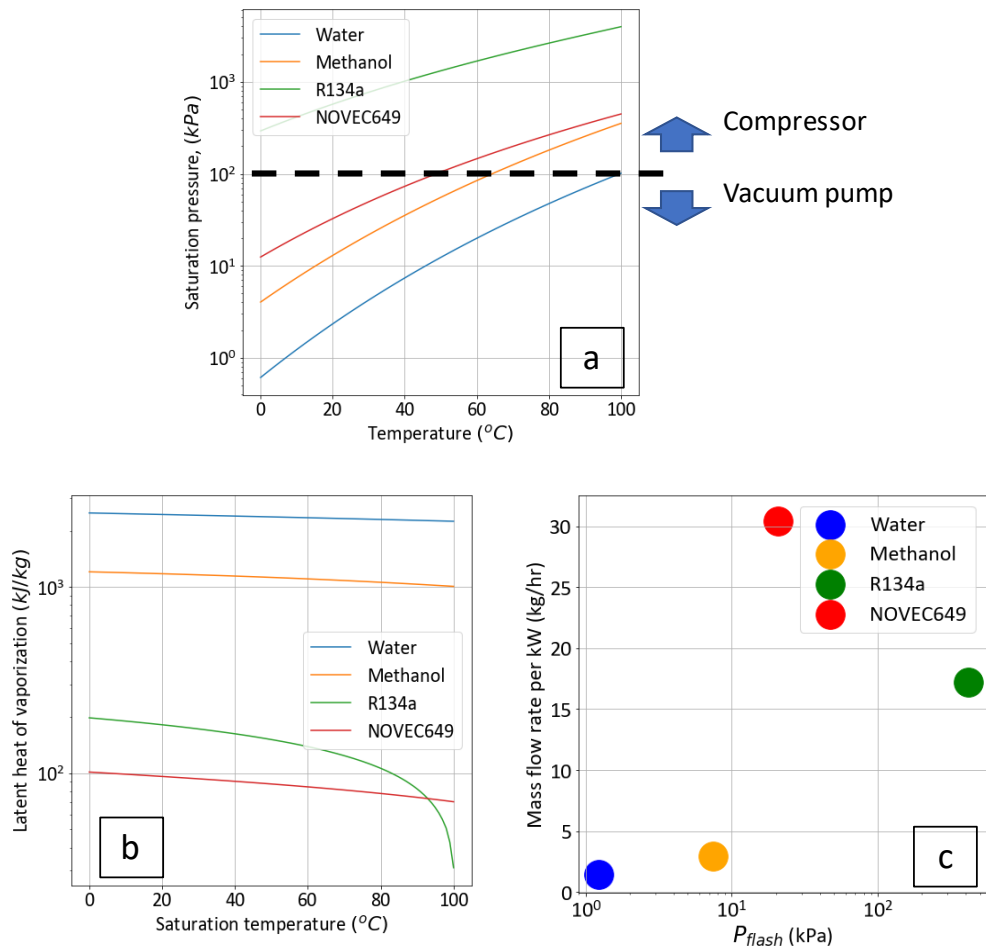


Figure 29: Comparison of water, methanol, NOVEC649 and R-134a for flash cooling. (a) Saturation properties to determine use of compressor or vacuum pump (b) Latent heat of vaporization as function of saturation temperature (c) Mass flow rate required per kW of cooling derived from phase change.

Table 3: Preliminary selection of coolant for laboratory flash cooling tests

Working Fluid	Freezing point (°C)	Boiling point (°C)	Latent heat (kJ/kg)	Surface tension (mN/m)	Copper compatibility	Polypropylene compatibility
Ethanol	-112	78	846	22	Excellent	Excellent
Methanol	-98	64	~1000	22	Good	Excellent
Water	0	100	2256	72	Good	Excellent
Acetone	-95	57	518	25	Excellent	Excellent
Pentane	-129	36	~350	16	N/A	Poor
R-134A	-103	-26.3	217	8.5	Excellent	Good
HFE7100	-135	61	125	13.6	Good	Good
Ammonia	-78	-33	1369	23	N/A	Excellent
Dowtherm	12	257	407	40	Good	N/A
Heptane	-91	98	318	20	Excellent	Fair

is inefficient and impractical. Thus, a commercial installation with more than 15kW cooling requirement should choose R-134a or similar refrigerants as the loop then functions at higher pressure and high mass flow rates managed by efficient compressors.

3.1.3. Refrigerant loop

A modified flow loop with stainless steel tubing and Swagelok® fittings is designed. The purpose is to utilize a refrigerant instead of methanol as the coolant. For control, current LabVIEW and CompactDAQ setup should serve as the basis, and a possibility of pneumatic solenoid combines system is considered (Parker Viking Lite series with Burkert Type 2103). This allows for lesser heat generation in the control valves as compared to current setup. Based on literature review, three refrigerants are given careful consideration: R134a, R410a and R1234ze. The properties as obtained from CoolProp are listed in Table 4. For simplicity, the initial state, and

Table 4: Estimation of flash cooling enthalpy for R134a, R410a and R1234ze based on CoolProp

Saturation temperature (°C)	R134a – Pressure (bar)	R410a – Pressure (bar)	R1234ze – Pressure (bar)	R134a – Enthalpy (kJ/kg)	R410a – Enthalpy (kJ/kg)	R1234ze – Enthalpy (kJ/kg)
-5, $x=1$	2.42	6.75	1.78	395.6	419.7	380.6
10, $x=0$	4.12	10.83	3.07	213.4	215.2	213.1
Δh				182.2	204.5	167.5

final states for all three coolants at their saturation conditions at $-5\text{ }^{\circ}\text{C}$ and $10\text{ }^{\circ}\text{C}$. It can be clearly seen that R410a has the maximum enthalpy change, indicating more maximum heat removal. However, R134a is a much cheaper and easy-to-handle refrigerant. Thus, it is decided to construct the loop for R134a. Similarly, 40-kW cooling system specifications are developed and submitted for future development with the Si-IF system.

3.1.4. Dynamic control with LabVIEW eco-system

The LabVIEW code is being developed in an integrated manner. It includes four different sub-codes: Power supply control, IR image data acquisition, PID decision code, and cooling data acquisition and control. The flow chart of the code is shown in Fig. 30 below. The overall Plumbing and Instrumentation Diagram (P&ID) is shown in Fig. 31.

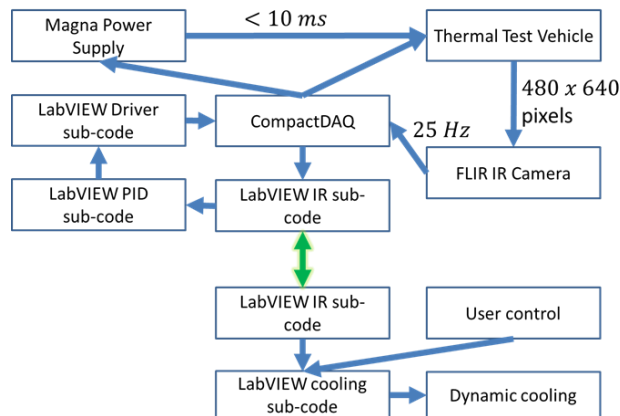


Figure 30: Flow chart for dynamic control of the setup with the help of LabVIEW and CompactDAQ.

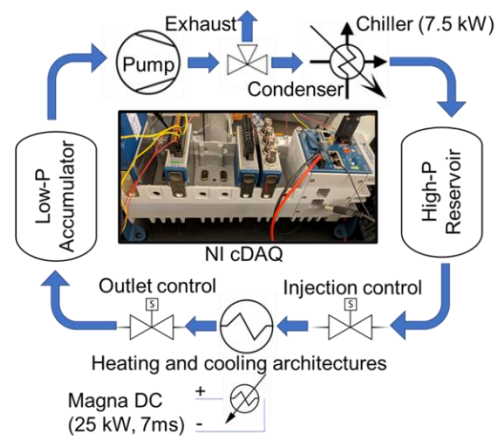


Figure 31: Simplified P&ID for the thermal testbed for flash cooling experiments [24]. The actual CompactDAQ controller used is included in the image.

3.1.5. Microsoft OneNote lab journal

A lab journal /notebook is created on OneNote with the template as shown in Fig. 32. The information provided in the journal is used to verify the data files of each transient experiment. Key qualitative observations including presence of liquid bubbles or slug flow at the outlet of the chamber is determined and noted in the journal. Additionally, the control times like heater ON and

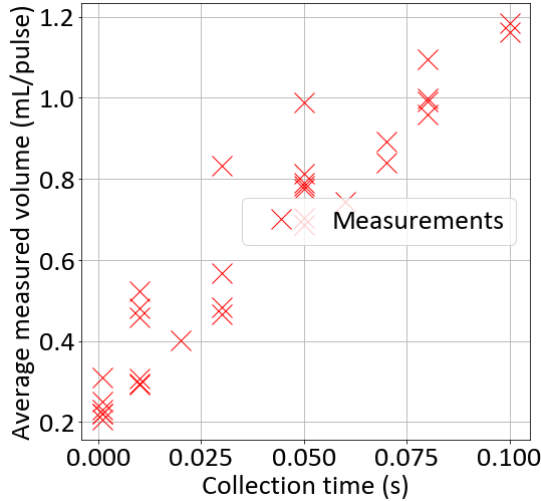


Figure 33: Calibration of injection control for flash cooling

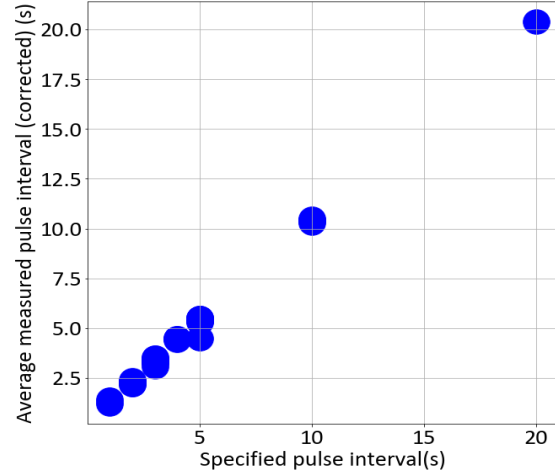


Figure 34: Corrected pulse interval VS specified pulse interval

chamber. This information allows user to design the system for specific cooling volume by controlling the collection time.

Similarly, the calibration of pulse interval specified in the LabVIEW eco-system was also performed. It has delays associated with DAQ controller and valve open/close delays. Thus, corrected pulse timings are analyzed in post-processing discussed in next section. For all the calculations, corrected pulse timings are used while the experiment labels use input parameters to allow for consistent design of experiments under different conditions. An example calibration plot from results discussed in section 6.4 is shown in Fig. 34.

3.2. PowerTherm 1.0 (PT1)

3.2.1. Architecture

In the first architecture, copper terminal blocks are attached on top of PowerBoard – a conventional PC board that incorporates voltage conversion needed for power delivery at mission voltage. Si-IF sits on top of copper terminal blocks with the help of Cu-Cu bonding [14]. Within the Si-IF, the power is delivered from back-side to top-side with the help of through-wafer-vias [47] (Fig. 35). The heat removal path takes place from Si-IF to the copper tubes through the same

terminal blocks. These tubes can be cooled either by single-phase or two-phase cooling method. Even though this architecture provided more control in terms of spatial cooling, the power delivery with large blocks was inefficient. Thus, it was decided to focus on this version for prototype thermal analysis but not for power delivery (and fabrication optimization). The construction details for this version are included in [13].

3.2.2. Prototype fabrication

The attachment of copper terminal blocks with the Si-IF is critical for structural integrity, electrical isolation between different voltage domains, and thermal conduction to the terminal blocks. The test structure used to perform preliminary experiments and simulations consists of three main elements: a silicon die ($28.5 \times 12 \times 0.525 \text{ mm}^3$) to mimic the Si-IF, a copper block ($8 \times 8 \times 24 \text{ mm}^3$) and a pipe (3.18 mm outer diameter, 2.54 mm inner diameter, 135 mm length) passing through the terminal block (Fig. 36). The copper terminal block and silicon die were

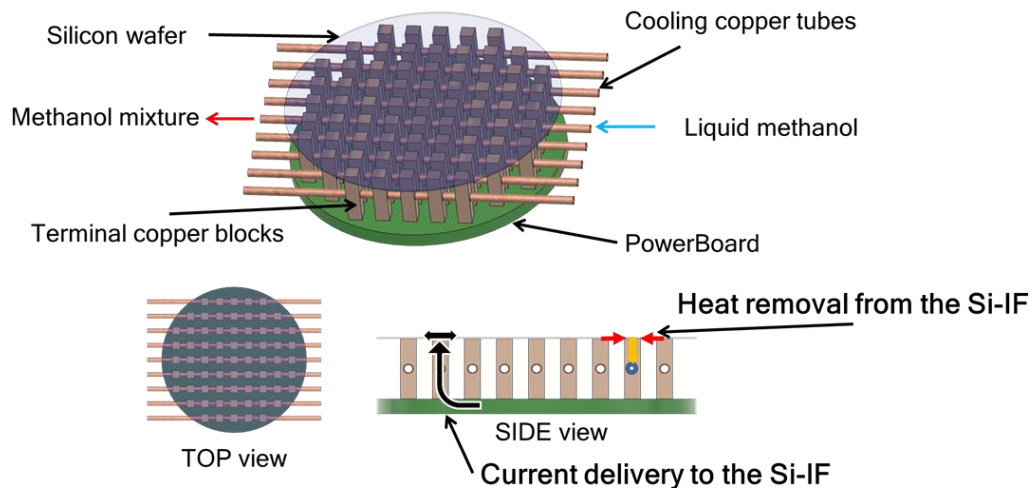


Figure 35: Architectural design of PowerTherm 1.0 [13] that incorporates block-and-tube arrangement. The silicon wafer has increased transparency to highlight the arrangement. The power delivery path from PowerBoard and heat removal path through the tubes are shown in the SIDE view.

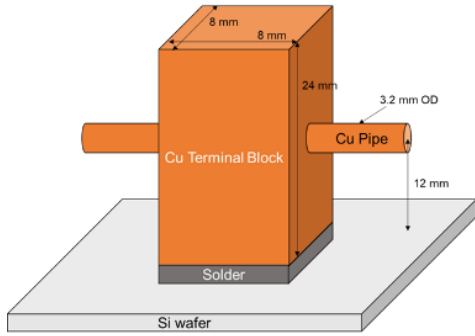


Figure 36: Cartoon depicting terminal block attached to a silicon die with prototype dimensions.

bonded using commercially available 50 μm thick Sn96.5-Ag3.5 solder film (Indium corporation). Solder was used to ensure good thermal and electrical connection. To ensure a mechanically strong bond, the silicon wafer had a thin film layer stack that consisted of 500 nm thermal silicon oxide, 30 nm titanium adhesion and diffusion barrier layer, 200 nm copper ‘wiring’ layer, 300 nm thick nickel diffusion barrier layer and 500 nm thick tin wetting layer. A similar stack of nickel barrier layer and tin wetting layer was deposited on the copper block. All metal deposition was done by sputtering in a Denton Discovery system. To improve the contact between the mechanically fitted pipe and terminal block, the pipe exterior was coated with a layer of thermal grease (Omega Engineering, Inc. – OT 201). A schematic of the bonded structure and thin film stack is shown in Fig. 37. The image of the single block prototype is shown in Fig. 38a. The prototype shown in Fig. 38b constitutes of an array of blocks, however, no testing was performed with this prototype.

barrier layer and tin wetting layer was deposited on the copper block. All metal deposition was done by sputtering in a Denton Discovery system. To improve the contact between the mechanically fitted pipe and terminal block, the pipe exterior was coated with a layer of thermal grease (Omega Engineering, Inc. – OT 201). A schematic of the bonded structure and thin film stack is shown in Fig. 37. The image of the single block prototype is shown in Fig. 38a. The prototype shown in Fig. 38b constitutes of an array of blocks, however, no testing was performed with this prototype.



Thin Film Layer Stack – Side View

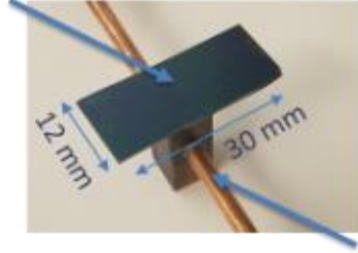
Figure 37: Attachment of copper block to silicon die is enabled through Ni and Sn thin films.

Inc. – OT 201). A schematic of the bonded structure and thin film stack is shown in Fig. 37. The image of the single block prototype is shown in Fig. 38a. The prototype shown in Fig. 38b constitutes of an array of blocks, however, no testing was performed with this prototype.

3.3. Steady-periodic analysis

For each test, averages are calculated for every pulse of flash cooling and if the amount of flash cooling being provided over time is sufficient to cool the prototypes, the average observations of temperature and pressure should be consistent. This is the point where average cooling provided by a flash cooling cycle has adjusted to the constant heat input to the system. Because each test has a different cycle time and requires different amount of time to achieve steady-periodic behavior,

Surface thermocouple/
IR camera (silicon)



Surface thermocouple
(copper tube)

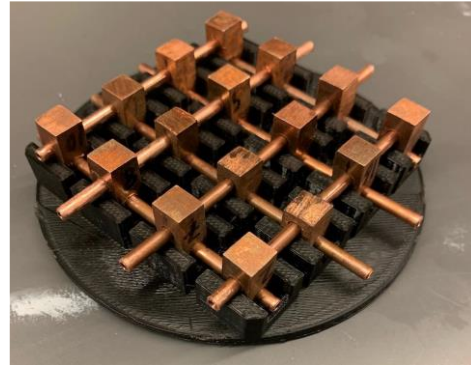


Figure 38: Prototypes for PowerTherm 1.0. (a) Single Si coupon with single block and tube (b) Array of blocks and tubes for 100 mm Si-IF testing (not finished as architecture discontinued)

only the steady-periodic regimes are included to calculate periodic averages. For each test, the average pulse temperature calculation is started from the last pulse and moved backwards in time to check the previous pulse average temperature until a difference of 1 °C in average temperature is observed. A similar assessment is performed with vacuum pressure (1 kPa) data and decide lowest common number of cycles. If the transient data falls under this category, the file is flagged as steady-periodic and further analysis is performed.

A simplified energy balance equation for the cooling architecture takes the form:

$$\dot{E}_{in}(t) = \dot{E}_{st}(t) + \dot{E}_{out}(t) = \dot{E}_{st}(t) + q_{nc}(t) + q_{rad}(t) + q_{fc}(t) \quad (39)$$

The energy input rate, \dot{E}_{in} , is due to the heating power, P , of the heater while the energy outflow rate, \dot{E}_{out} , is composed of three components: natural convection, q_{nc} , radiation, q_{rad} , and flash cooling, q_{fc} . The difference between the input and output energy constitutes the energy storage rate, \dot{E}_{st} , and produces a rate of change of temperature depending on the lumped mass, m , and heat capacity, C_p . Assuming that natural convection and radiation effects are combined and only depend on Si temperature, under steady-periodic conditions and starting with (39),

$$P = G_{loss}(\langle T_b \rangle)(\langle T_b \rangle - T_a) + \langle q_{fc} \rangle \quad (40)$$

The theoretical maximum cooling, $E_{max,p}$, with any flash cooling pulse is calculated based on the mass of methanol used, m_p , and the difference in enthalpy, Δh . The starting enthalpy, h_i , is calculated based on initial reservoir or steady-state conditions. The outlet enthalpy, $h_o = h(P_o, T_b > T_{sat})$, is calculated using outlet pressure and average temperature of the lumped mass of the prototype. This approach highlights the best-case scenario for a two-phase coolant to exchange heat with the chamber under specific experimental conditions at thermodynamic equilibrium. Thus, the obtained efficiencies are the limiting worst-case efficiencies for the flash pulses. The enthalpy calculations were performed with a Jupyter notebook accessing the Coolprop database.

$$\langle q_{max,p} \rangle = \dot{m} \Delta h = \frac{v_p}{t_p} \rho_i \Delta h = \frac{v_p}{t_p} \rho_i (h(\langle P_o \rangle, \langle T_b \rangle) - h_i) \quad (41)$$

For pulsed cooling, the cumulative efficiency, η , is calculated using the ratio of average cooling rate, $\langle q_{fc} \rangle$, of the pulse to the theoretical maximum from (41).

$$\eta = \frac{\langle q_{fc} \rangle}{\langle q_{max,p} \rangle} \quad (42)$$

3.4. Prototype results

The flow loop was used to test a single terminal block bonded to silicon die as shown in Fig. 38. The primary motivation is to understand the transient cooling characteristics of a single terminal block, which would help to scale-up to a full wafer. After initial tests on single blocks, arrays of 4x1 and 1x4 terminal blocks were planned. However, the bonding process for array did not work reliably, and efforts were diverted for improved architecture described in Chapter 4.

Hence, the discussion in this work is based on the results for a single terminal block attached to a silicon die.

The parameter space is critical to understand how each cooling architecture behaves in different

scenarios expected during the design and run-time for flash cooling of Si-IF. Section 3.3 provided information on the steady-periodic analysis. The input parameters used are shown in Table 5. The parameter space has an extra variable, compared to other prototype testing in subsequent chapters, that was introduced to observe the effects of different triggering temperatures for flash cooling.

A single pulse was first used as to demonstrate the pressure drop in temperature with respect to time for 2 ml of methanol and 6W of power supply. The heat load applied was to provide a near-steady temperature before flash cooling pulse was started. A significant temperature drop occurs as soon as the methanol is injected into the vacuum tube (indicated by peak in vacuum pressure). A considerable temperature drop is achieved over a period of few seconds (Fig. 39).

Flash cooling pulse cycle tests were performed with varying cycle time: 40s, 20s, 15s and 15s_70. Flash cooling was initiated when the silicon temperature reached 80°C except for last test

Table 5: Parameter selection for PT1 prototype

Parameter \ Selection	I	II	III
Power, P (W)	6	10	20
Volume, v_p (mL)	1	2	
Interval, t_p (s)	40	20	15
Flash cooling start temperature (°C)	80	70	

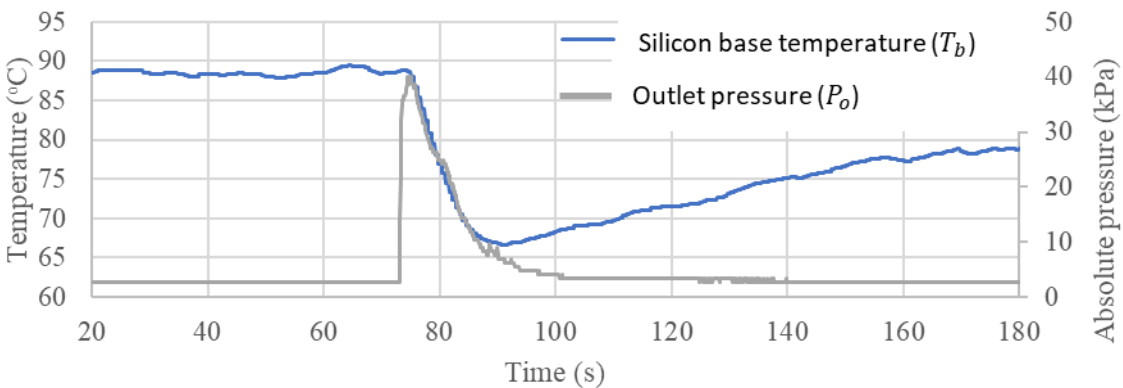


Figure 39: Single pulse cooling of silicon with terminal block (PT1 prototype) is demonstrated by the drop in T_b . The pulse is indicated by the outlet pressure jump indicated on the secondary axis.

where the flash cooling cycle was initiated earlier at 70 °C (Table 6). This test was done to see the effects of initiation temperature on the transition period leading to steady-periodic regime of the silicon die temperature. The common parameters for the experiments include a time delay assigned for opening and closing of valves for the whole loop of 0.5 s, which could be reduced to order of 100ms but during initial testing it was chosen to keep a safe observable margin. Hence, for a pulse cycle of flash cooling with 20 s period, the actual pulse cycle is 20.5 s. Methanol injection was limited to 1 ml/cycle for each cycle performed. The starting temperature of the system including the silicon, copper terminal block and copper tube was kept between 20-22 °C before heating started. A constant current of 5A was passed through the silicon die using the power supply to provide heat input. The average joule heating supplied in each test varied between 18.25 W and 19 W due to variation in resistance caused by the temperature variation. Data collection took place for 400 seconds at 10 Hz for each test after heating starts. The vacuum pressure, copper tube temperature and the silicon temperature for first three tests are shown in Fig. 40.

Each typical test starts with heating at 20°C, increases in temperature, followed by flash cooling at 80 °C (or 70 °C), and eventually the temperature should stop decreasing at a fast rate. However, it is seen that for each test, the first flash cycle is not cooling the copper tube as well as the silicon die. The reason being the existence of helium in the system which is used to displace air before each test that causes negligible methanol injection and thus no coolant flow. Each test shows another similarity, namely a steady-periodic temperature profile for copper tube and the silicon die. This is the point where average cooling provided by a flash cooling cycle has adjusted to the constant heat input to the system. Because each test has a different cycle time and requires different amount of time to achieve steady-periodic behavior, only the steady-periodic regimes are

included to calculate periodic averages. For each test, the average pulse temperature calculation is started from the last pulse and moved backwards in time to check the previous pulse average temperature until a difference of 1 °C in average temperature is observed. A similar assessment is performed with vacuum pressure (1 kPa) data and decide lowest common number of cycles. In

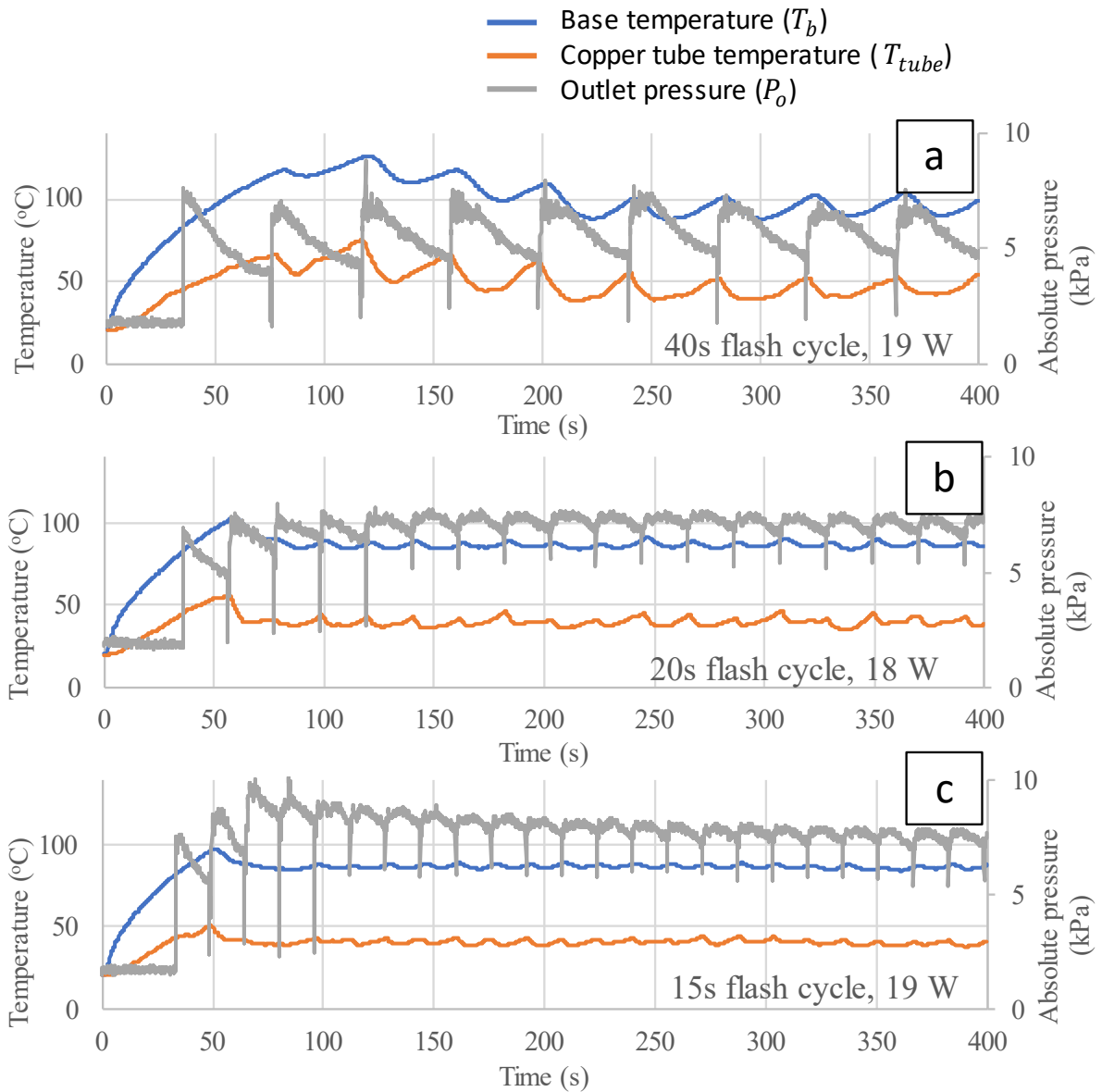


Figure 40: Temperature profile and pressure variation for different pulse cycles under constant heat load condition. (a) 40s flash cycle, (b) 20s flash cycle, (c) 15s flash cycle.

Table 6: Steady-periodic averaged data for PT1 prototype

Pulse time, t_p (s)	Base temperature, $\langle T_b \rangle$ (°C)	Base temperature variation, ΔT_b (°C)	Outlet pressure, P_o (kPa)
40	94	± 8	6
20	87	± 4	7
15	87	± 3	8
15_70	87	± 3	8

this way, last 5, 6, 19 and 20 cycles are included for calculating averages for 40s, 20s, 15s and 15s_70 tests respectively (Table 6).

The average absolute vacuum pressure, as expected, is lowest for the 40s cycle (6 kPa) where methanol has more time to absorb heat and the vacuum pump can pull more vapor out of the tube, followed by 7 kPa for the 20s flash cycle and 8 kPa for the 15s and 15s_70 cycle (Fig. 41). A comparison of silicon die temperature for each test indicates that the overall periodic average temperature is higher for the 40s (94.4 °C) flash cycle as compared to others. The 20s and 15s tests show similar average temperatures: 86.5 °C and 86.7 °C respectively. The 15s and 15s_70 tests have some liquid droplets coming out of the flashing tubes as compared to no droplets for 20s or 40s tests indicating a threshold on the heat to be taken out. There is a similarity between

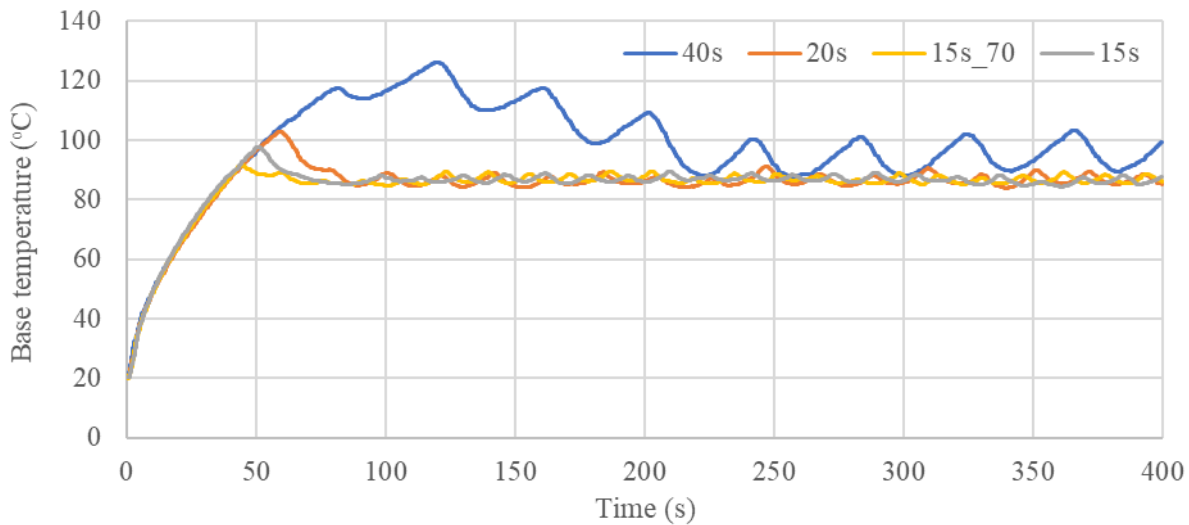


Figure 41: Comparison of different flash cooling pulse timing under the same heat load with PT1 cooling architecture.

15s and 15s_70 tests when the steady periodic averages are compared. However, 15s_70 test provided a much cooler highest temperature for the silicon die. The temperature variation on the silicon die, defined as the half-difference between maximum and minimum temperature during the steady periodic observation, is shown in Table 6. The 40s test shows the highest variation ($> \pm 5$ °C) which is unacceptable for the silicon die. However, the other three tests show much less temperature variation and thus represent better solution for steady heating.

Chapter 4: Wafer-scale cooling with pin-fin flash chamber

4.1. PowerTherm 2.0 (PT2)

4.1.1. Architecture

A co-designed architecture for combined power delivery and heat extraction was developed with a focus on the Si-IF backside (Fig. 42). A cooling chamber is created with a machinable AlN/BN ceramic (Shapal Hi-M soft, Precision Ceramics USA, Inc.) as the top surface, while the bottom and sides are made of polybenzimidazole polymer (Celazole® PBI). The inlet of cooling chamber is at the center, with larger outlets on the four sides allowing for quadrant symmetric cooling. The ceramic layer touches the Si-IF directly and thus serves as a dielectric medium between the active wafer and cooling chamber. The high thermal conductivity of the ceramic (92 W/mK) allows for efficient heat transfer from the Si-IF to the cooling chamber. The ceramic is machined to fit copper pin fins of 1.56 mm diameter.

The copper pin fins are thermo-compression bonded (TCB) to the backside of the Si-IF, which has a power redistribution layer that connects to through-wafer-vias allowing for back-side

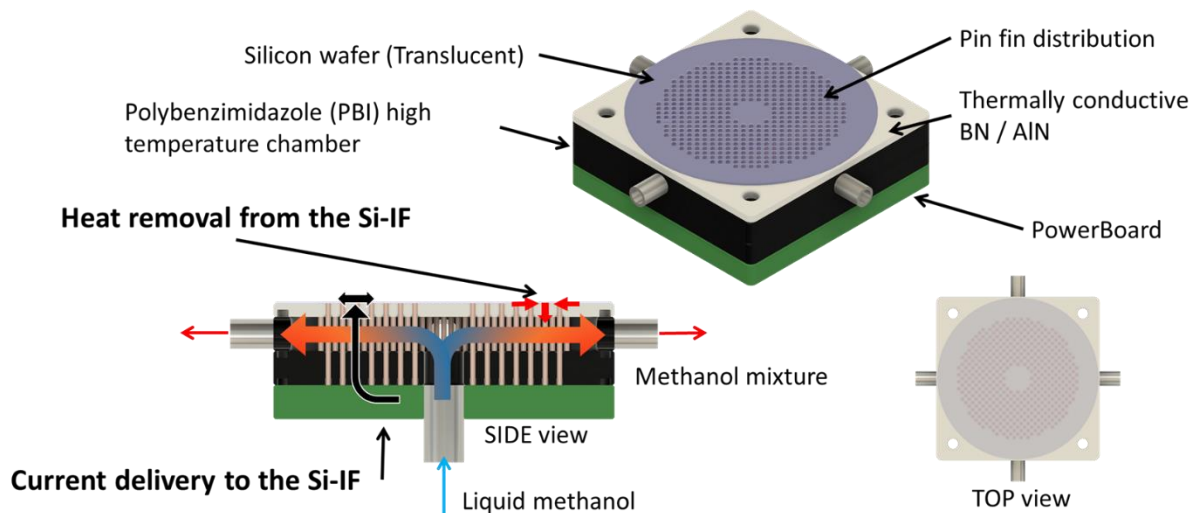


Figure 42: Architectural design of PowerTherm 2.0 [24] that incorporates a wafer-scale cooling chamber with pin-fins to enhance heat transfer for flash cooling.

power delivery as discussed in section 3.2. The pin fins are inserted into the ceramic top and polymer bottom and then sanded and polished (Fig. 43a). Then the copper pin fins are bonded to Si-IF with TCB in a vacuum environment as shown in Fig. 43b.

The structure itself acts as a supporting jig for the TCB process. The PBI has a service capability up to 399 °C in inert environments, allowing the structure to be used during the TCB process. The PBI has low thermal conductivity (0.4 W/m·K), and thus its sides also insulate the cooling chamber and maintain the surface temperature close to ambient. On the bottom side, the copper pin fins are attached to a power board (Fig 42) that supplies current at a target voltage (0.8-1 V) thus acting as power-ground terminal pins for the DC power supply. A detailed characterization of power delivery network (PDN) can be found in [48]. One important conclusion from the switching impedance of the PDN is that the length of the pin fins dictates the power losses and leads to high impedance (>100 mΩ for >1 Ghz) that sets a constraint on high-frequency devices in this Si-IF package.

Because the pin fins of the PDN are directly bonded to the Si-IF, they significantly enhance heat conduction into the cooling chamber due to higher base temperature and high thermal conductivity. The advantage of using combined back-side power delivery and cooling is that it frees the top side for other advanced components such as optical communication. Additionally, the top side can also be used for supplemental cooling. The dielets on Si-IF directly interface with a cooling chamber. The foundation for cooling is a high thermal conductivity copper baseplate (400 W/m·K) instead of a ceramic, as the thermal interface material used on the dielets is dielectric. This feature allows for efficient heat transfer into the cooling chamber. The top cover of the chamber can be determined based on structural requirements. For example, stainless steel provides good mechanical stability and allows for inlet tubes into the cooling chamber.

4.1.2. Prototype fabrication

A prototype cooling chamber (39 mm x 39 mm x 20 mm) along with a bonded silicon coupon acting as a passive Si-IF was constructed to perform electrical measurements and flash cooling tests (Fig. 43c). The inlet and outlets are tapped with 1/16th NPT threading, and Swagelok® fittings are used to create leak-proof connections to the thermal testbed described in Chapter 3.

4.2. Lumped capacitance analysis

A lumped capacitance-based energy balance is performed to provide a high-level interpretative model of flash behavior and performance. The simplified energy balance described in (39) is used as starting point for the analysis. The heat loss through natural convection depends on heat transfer coefficient, h , and surface area, A . Similarly, radiation heat loss depends on the emissivity, ϵ , Stefan-Boltzmann constant, $\sigma = 5.67 \times 10^{-8} \text{ W/m}^2 \cdot \text{K}^4$ and A . Thus, (39) can be written as:

$$P(t) = \langle mC_p \rangle \frac{dT_b(t)}{dt} + \langle hA \rangle (T_b(t) - T_a) + \langle \epsilon \sigma A \rangle (T_b(t)^4 - T_a^4) + q_{fc}(t) \quad (43)$$

$$P(t) = C_{th}(T_b, P) \frac{dT_b(t)}{dt} + G_{loss}(T_b)(T_b(t) - T_a) + q_{fc}(t) \quad (44)$$

The thermal capacitance and loss coefficients, C_{th} and G_{loss} respectively, are key unknowns that must be fitted to obtain the flash cooling provided at any given time.

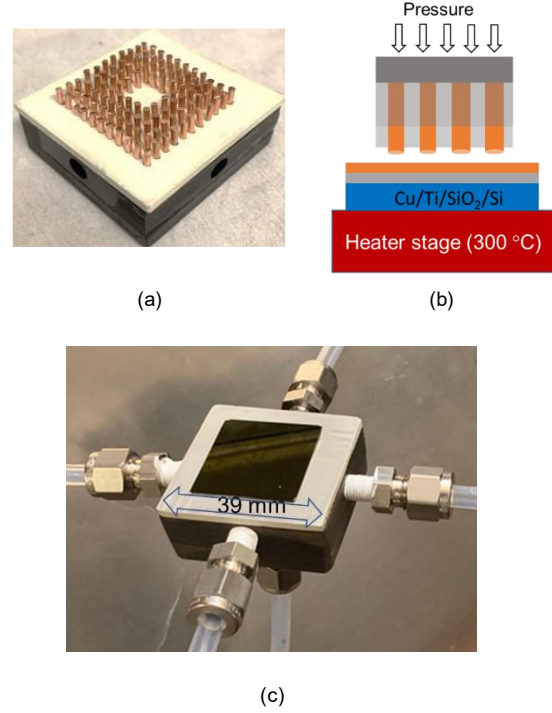


Figure 43: Prototype of pin fin cooling chamber. (a) Copper pins inserted into the top and bottom layers (b) Thermo-compression bonding of pins to Si-IF. (c) Prototype with fluid connections for thermal test bed.

4.3. Prototype results

For the pin fin chamber, all the coefficients were obtained with (44) using least-squares fitting of the constant heating curves until they reach steady-state temperatures. The obtained coefficients are $a = 33.52 \text{ J/K}$, $b = 0.11 \text{ W/K}$, and $c = 5.67 \times 10^{-10} \text{ W/K}^4$. The theoretical summation of individual thermal capacitances $\langle mC_p \rangle$ of heterogeneous components of the chamber predicts the value of $a = 30 \text{ J/K}$, which is close to the curve-fitted parameter from the experiments.

For pulsed-cooling experiments with the pin fin chamber, the chamber is first evacuated to below 6 kPa absolute pressure with the help of the vacuum pump. The outlet valve that connects to the pump is always open during experiments, thus pulling vacuum continuously. The prototype is then heated at constant power until the temperature reaches 40 °C at which point the flash cooling cycle starts. A specific amount of methanol (1.5 mL) is injected using calibrated solenoid valve timings and verified with reservoir volume monitoring. After injection, the inlet valve is opened at specified pulse times.

Periodic flash cooling experiments were performed (Fig. 44) for different heating powers ($P = 10, 15, 22 \text{ W}$) and different pulse times ($t_p = 20, 40, 60 \text{ s}$). The initial enthalpy is constant as the liquid reservoir is at 25 °C and 101.325 kPa ($h_i = -1.05 \times 10^5 \text{ J/kg}$, $\rho_i = 792 \text{ kg/m}^3$). The data are recorded for at least 400 s after initiation of cooling. The temperature of the silicon coupon is

Table 7: Parameters selected for flash cooling with PT2 prototype.

Parameter \ Selection	I	II	III
Power, P (W)	10	15	22
Volume, v_p (mL)	1.5		
Interval, t_p (s)	60	40	20

measured with a surface thermocouple placed on top of the coupon. The data were then processed with the Savitzky-Golay filter [49] in SciPy [50] using 2nd order reduction and six side-points to reduce random peaks in heat flux calculations due to high-frequency noise in

temperature data, without compromising the overall results. The flash cooling rate at any time, $q_{fc}(t)$, is evaluated by using (44) with this processed data.

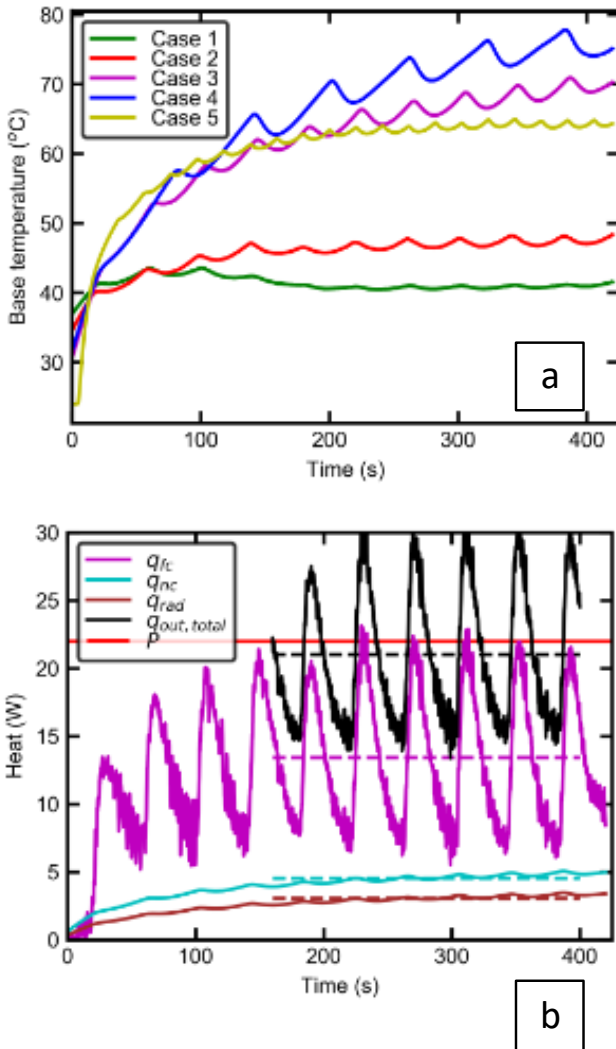


Figure 44: Continuous pulsed cooling with 1.5 mL methanol per pulse. (a) Temperature profiles for different heating power and duration of pulse (b) Heat estimations from natural convection, radiation and flash cooling based on (44) for case 3 (22 W, 40 s). The dashed line represents the periodic averages over 240s and tabulated in Table 8.

The averaged cooling rate is then substituted in (42) to obtain the cumulative efficiency of pulsed cooling. The table includes the average cooling rates and cumulative efficiencies for different cases. Fig. 44a shows the temperature profile from five cases with 22 W power and 40 s pulses as the base case. Fig. 44b highlights the different heat outputs associated with the base case. The convection and radiation heat losses are calculated from the recorded temperature and plotted along with flash cooling based on (44). The dashed lines represent the periodic averages obtained as described above. The average total heat out is about 21 W, and thus the periodic average temperature should still increase as can be seen in Fig. 44a.

The periodic averaged results for a period of 240 s (from 160 s to 400 s) after

flash cooling initiation are reported in Table 8. The average cooling rate is obtained by integrating the time-dependent cooling rates for each case and averaging over time:

$$\langle q_{fc} \rangle = \frac{\int_{t_i}^{t_f} q_{fc}(t) dt}{t_f - t_i}; t_i = 240 \text{ s}, t_f = 400 \text{ s} \quad (45)$$

The first three temperature profiles illustrate effect of different heating powers while same parameters are used for flash cooling. The silicon temperature rise exhibits a significant change in slope with the first pulse of flash cooling in all cases. The temperature profiles asymptote toward different steady-periodic temperatures as expected for 10 and 15 W conditions. However, the average cooling was insufficient to cool the 22 W heat input. The outlet pressures in Fig. 45a indicate that higher heat inputs produce higher peak pressures, indicating increased vapor generation at higher temperatures as time progresses.

The drop in pressure is also slower for higher heat fluxes, indicating further heterogenous boiling of remaining liquid in the chamber that produces the higher cooling rates observed in Fig. 45b. Another important feature

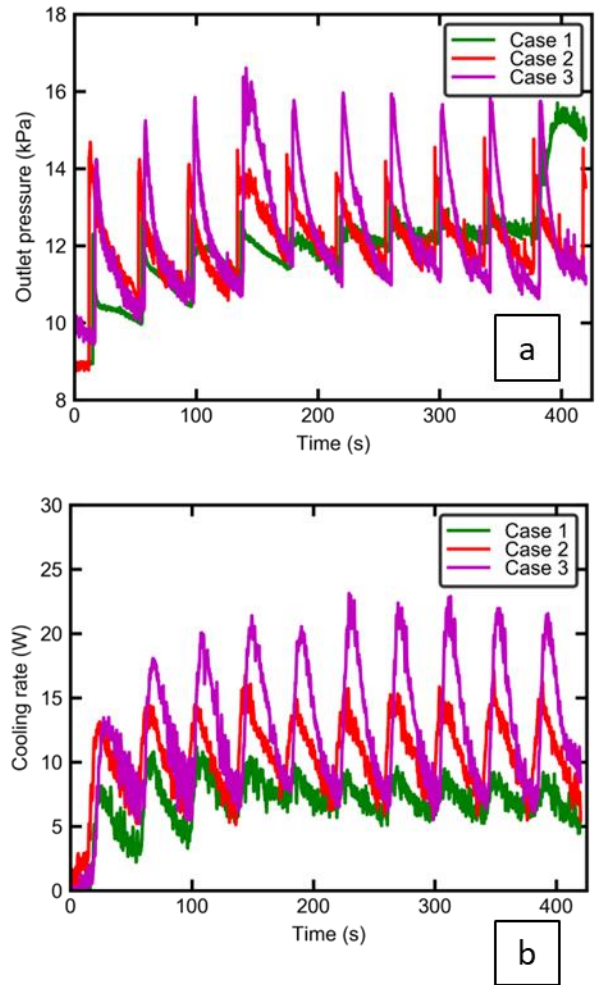


Figure 45: Continuous pulsed cooling with 1.5 mL methanol every 40s but different heating. (a) Outlet pressure indicating the chamber conditions over time (b) Cooling rate as calculated based on (44) from obtained temperature profiles in Fig. 44a.

is the faster evacuation of coolant with higher heat flux, allowing for higher cooling rates in subsequent pulses. The efficiency of cooling increases from 0.2 to 0.4 (Table 8) due to increases in both convection coefficient with increased vapor generation and temperature difference. Even though the 10 W condition appears steady- periodic at this low heating rate, the liquid methanol starts to pool in the chamber until a point where the actual flash process occurs primarily at the outlet of chamber rather than near the inlet tube or heat source. This phenomenon is evident from sudden increase in outlet pressure beyond 350s in Fig. 46a and visible liquid slug flow in the outlet during the experiments.

The last three temperature profiles in Fig. 46a compare the effect of pulse timing at a fixed heating condition. Increased mass flow rate is expected to increase cooling rate and decrease the periodic average temperature. The silicon temperature has significant and equal change in slope with the first pulse of flash cooling in all cases. It is evident from Fig. 46a and Fig. 46b that initial cooling rates are consistent for all three cases. For the 20s pulse, the average outlet pressure is higher even though the amplitude is smaller, indicating reduced flash efficacy. At the same time, this case has the least temperature and cooling

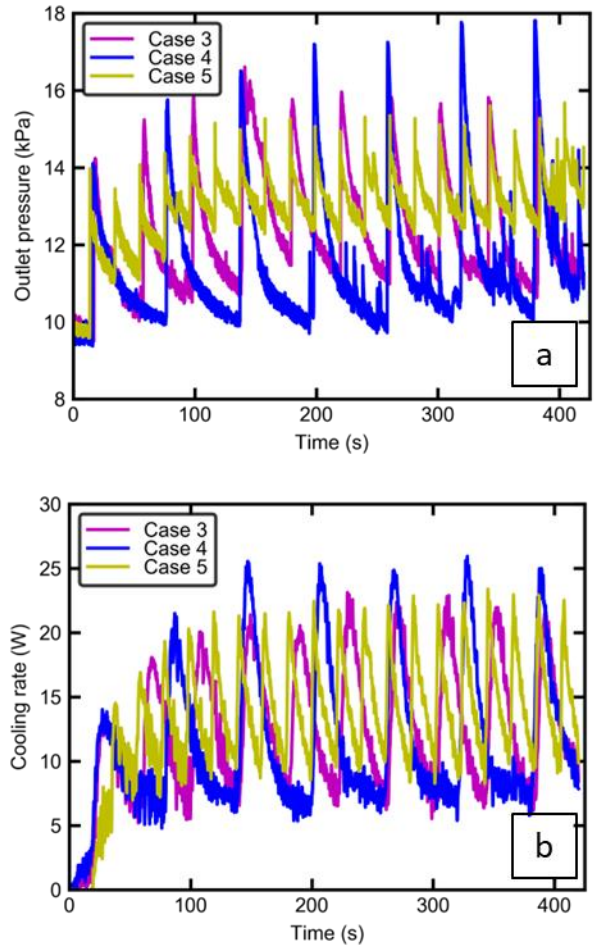


Figure 46: Continuous pulsed cooling with 1.5 mL methanol for heating power of 22 W. (a) Outlet pressure indicating the chamber conditions over time. (b) Cooling rate as calculated based on (44) from obtained temperature profiles in Fig. 44a.

Table 8: Periodic averaged observations and calculations. Data is collected for 240 s (t=160 s to 400 s) and thus incorporates complete pulses for all 5 cases.

Case	Power, P	Interval, t_p	Volume, v_p	Outlet pressure, $\langle P_o \rangle$	Base temperature, $\langle T_b \rangle$	Maximum enthalpy change, Δh	Theoretical maximum cooling, $\langle q_{max,p} \rangle$	Observed average cooling, $\langle q_{fc} \rangle$	Cumulative Efficiency, η
	(W)	(s)	(mL)	(kPa)	(°C)	(kJ/kg)	(W)	(W)	
1	10	40	1.5	12	41	1205	36	7	0.2
2	15	40	1.5	12	47	1214	36	11	0.3
3	22	40	1.5	13	67	1244	37	13	0.4
4	22	60	1.5	12	72	1253	25	12	0.5
5	22	20	1.5	13	64	1240	73	15	0.2

rate variation due to faster pulses. Similar to the discussion above, the efficiency increases with slower pulses due to reduced initial pressures and higher temperatures.

4.4. Thermal test vehicle

The next-generation electronic packaging techniques push the thermal limits of materials and systems. This leads to higher power densities along with high thermal gradients in the complex packaging structures.

To evaluate the thermal behavior of an electronic package in its preliminary stages, a thermal test vehicle can be used to validate the thermal design. Thermal test vehicles (TTVs) are made to match the demand of increasing power densities and thus they offer a reliable and cost-effective solution instead of prototyping with real and expensive dies. This work discusses the

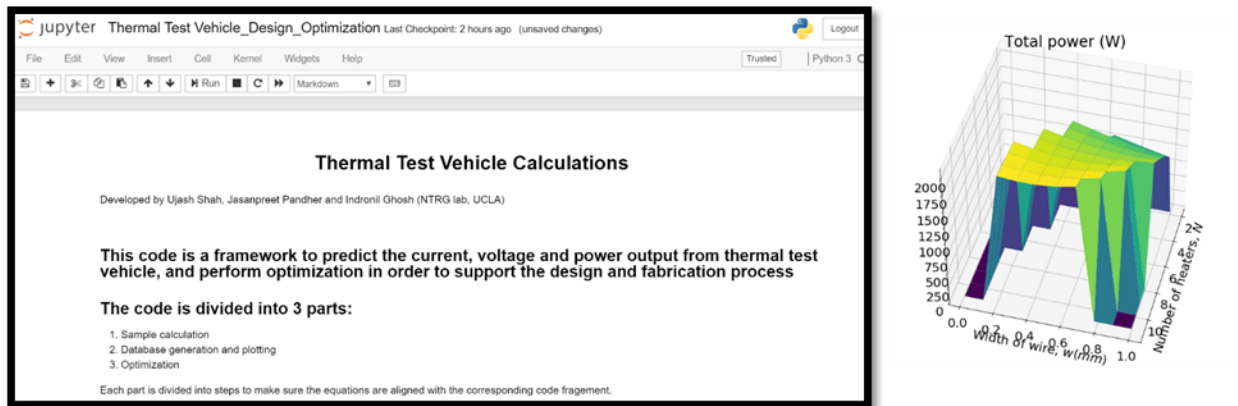


Figure 47: Optimization of thermal test vehicle with the help of Jupyter notebook. Single or double metal layer trace parameters are optimized for maximum joule heating given power supply and safety constraints.

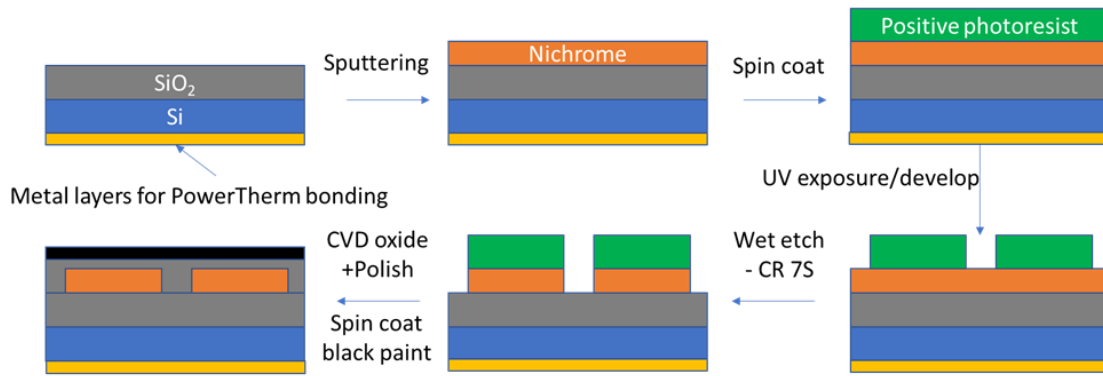


Figure 48: Nichrome TTV fabrication process flow for single metal layer nichrome deposition

design and analysis of a thermal test vehicle for Silicon Interconnect Fabric (SI-IF) - an innovative heterogenous integration platform.

A thermal test vehicle is designed and fabricated to achieve the highest maximum power given the fabrication, supply, and control constraints. The structure discussed in this work contains an array of nichrome heaters over a 100-mm wafer. To determine the placement and size of the heaters, a Jupyter based python framework (Appendix E) is developed to provide optimization needed to decide design parameters (Fig. 47).

A detailed LabVIEW program is developed which provides control of the power supply along with individual control for each heater. The code contains an in-built PID control to allow for different heating scenarios (Fig. 49). The software is also integrated with infrared imaging to visualize and collect temperature data over the whole vehicle with good resolution thus eliminating the to incorporate a sensor layer in fabrication process. The code is assessed with different heating conditions to enable support for variety of electronic package

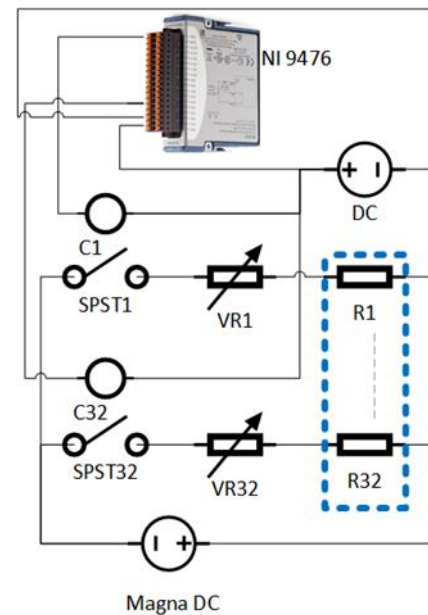


Figure 49: Two-step relay control for dynamic heating. The CompactDAQ can only support small current relays (<1.5A) so external relays are used to handle actual current flowing through the heaters.

cooling projects. There is also a two-step relay control setup for managing dynamic heating with variable resistances on the fabricated heaters as shown in Fig. 50.

Three different version of thermal test vehicle are fabricated with improvements in nichrome deposition process (Fig. 48). The nichrome based TTV is shown in Fig. 50c and Fig. 50d with initial IR imaging results (with and without

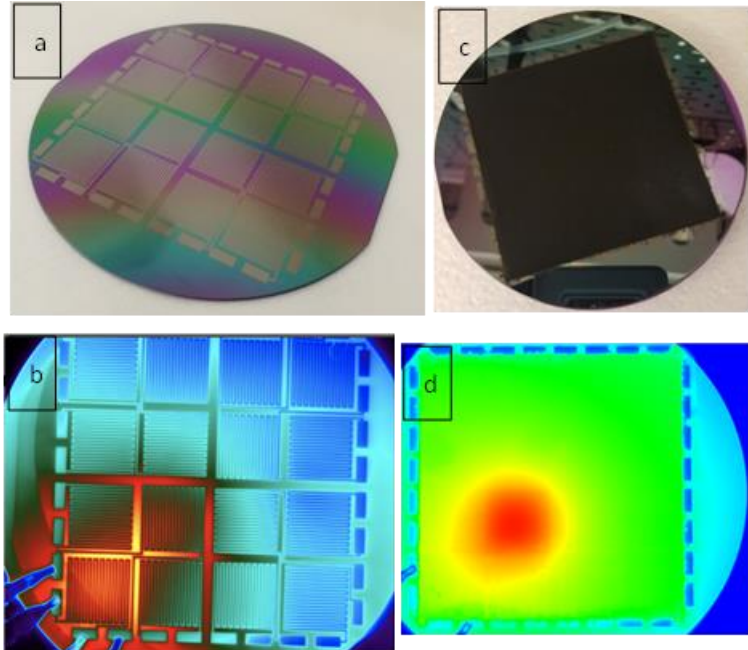


Figure 50: Nichrome based TTV; a) After nichrome deposition, b) IR imaging without emissivity adjustment, c) Black coat of about $30\ \mu\text{m}$ for uniform emissivity, d) IR imaging with uniform emissivity (Controlled heating is visible)

emissive coating). Due to fabrication limitations, the design only provided up to $0.1\ \text{W}/\text{mm}^2$ of heating.

An improved designed and process flow was developed with two metal process where copper was used for wiring and nichrome for resistive heating – providing 10×10 array of heaters (Fig. 51). However, the fabrication posed certain challenges including reliability of heater connections, expensive solder connections at $<200\ \mu\text{m}$ pitch, and limited heat flux of up to $0.3\ \text{W}/\text{mm}^2$.

Due to fabrication limitations at UCLA, a heater design was developed in collaboration with Stellar Industries Inc. to create a thick nichrome pattern of a ceramic substrate.

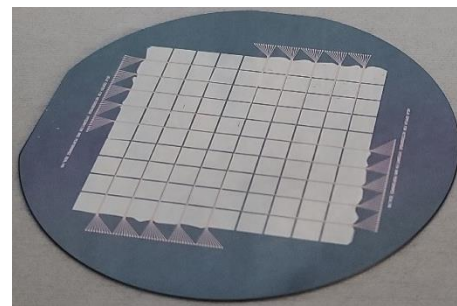


Figure 51: Nichrome heating layer with copper routing layer to act as thermal test vehicle providing up to $0.3\ \text{W}/\text{mm}^2$.

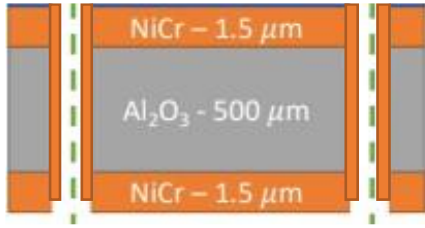


Figure 52: Double-sided nichrome deposition on Al₂O₃ ceramic substrate. Both sides are shorted with the help of nichrome coating in the lug area.

The design is shown in Fig. 53. The design power is 9000 W for a 6-in wafer. However, due to raw material delays, the heater was available towards the end of the scope of this work and thus, enough information is documented for future work.

Two ceramic wafers were received (Fig. 52) with nichrome deposition. The resistance measurement and electrical connectivity tests were performed using manual probe station. The resistances of each zone on individual wafers are shown in Fig. 54a and Fig. 54b, respectively. The connections between front and back side are acceptable in wafer 1, however, there are broken connections in wafer 2 – except zone 2. Since the TTV is

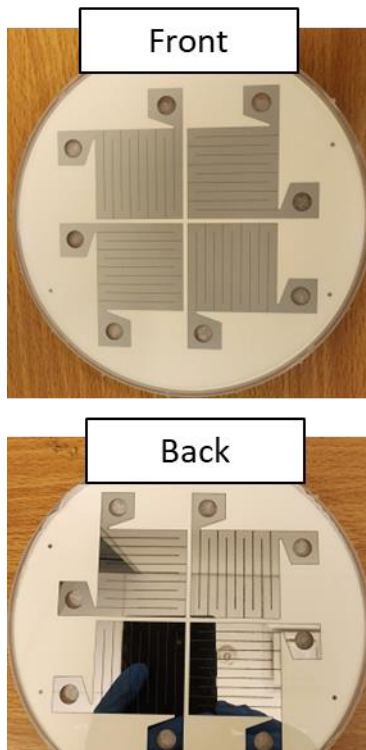


Figure 53: Images of nichrome TTV on ceramic wafers. Minor scratches visible when using a magnifying glass.

designed to use as 4 zones of individual high-heat flux heating substrates, it is recommended to laser cut wafer 2 and use individual heaters for testing smaller prototypes as seen in sections 3.4, 4.4, and 5.3. Consecutively, wafer 1 is recommended for simulating 100-mm Si-IF platform.

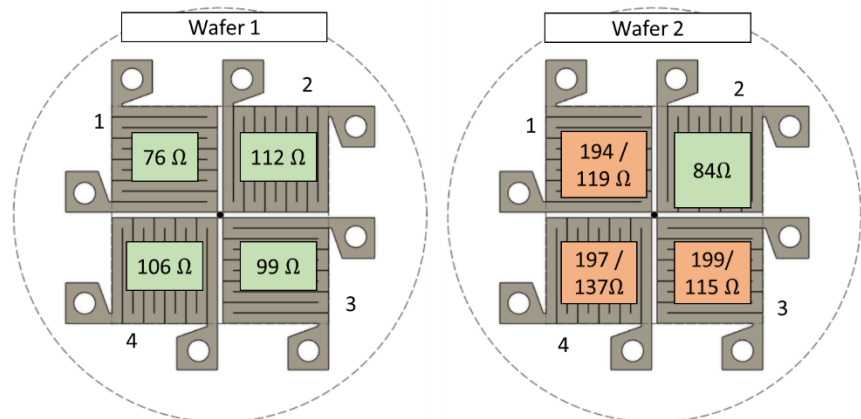


Figure 54: Resistance map of nichrome TTV on ceramic wafer. Green and red box indicates good and bad connection, respectively, between back and front side of the wafer.

Chapter 5: Segmented thermal management with array of pin-fin flash chambers

5.1. Thermal Dissipation Unit (TDU)

5.1.1. Architecture

The proposed segmented cooling architecture consists of an array of flash chambers or “cooling zones” or “thermal dissipation units” (Fig. 55). Each zone is cooled by on-demand flash cooling. A flash chamber consists of a copper heat sink with pin fins for enhanced heat transfer. There is one central inlet injecting the flashing fluid near the base plate and four outlets collecting the vapor dominant mixture with a radial symmetry. These heat sinks can either be individually fabricated or forged together as one unit. The heat sinks are closed for two-phase cooling with the help of a common stainless steel top plate. The top plate is bigger than the wafer and provides

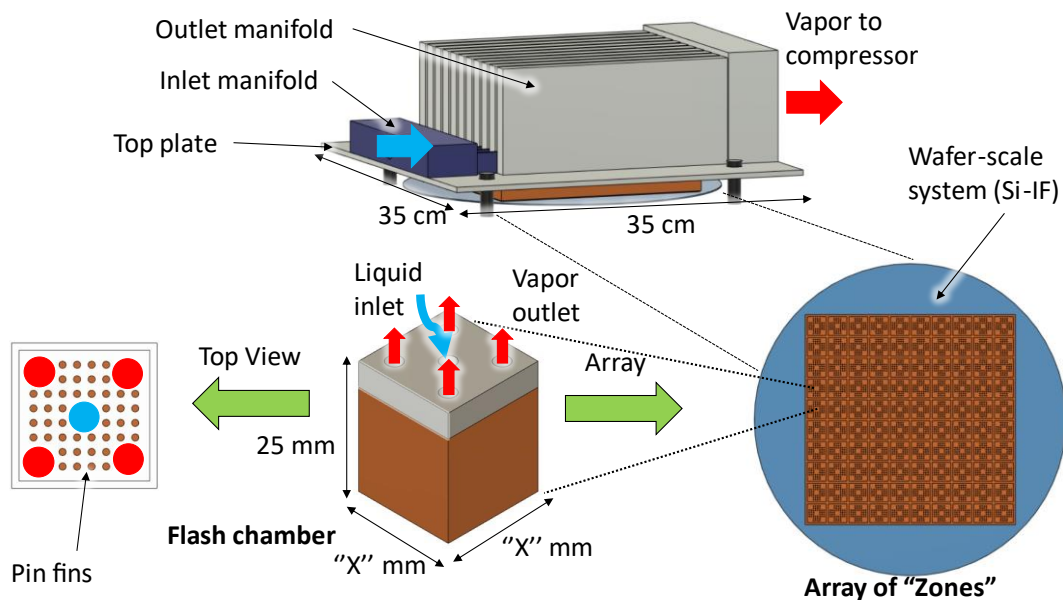


Figure 55: Description of the architecture for segmented thermal management with flash cooling zones. Each zone consists of a flash chamber with individual inlet and outlets. A top plate combines all zones into a common entity and connects them with the inlet and

mechanical support and allows for compression of heat sinks over the wafer for uniformity of the heat sinks with irregularly heighted dies (up to 200 μm) on the wafer-scale system with the help of thermal interface material. The top plate also provides fluidic connections to the individual heat sinks.

The size of inlet and outlet connections are determined based on the flow rate coolant. Standard NPT fittings are preferred for the outlets while the inlet tubes are recommended to be welded with the top plate to allow for deeper insertion without the space constraints of bulkhead fittings otherwise necessary. The overall assembly is designed to allow for rework ability without replacing any major components.

The inlet manifold consists of distribution hub, row-wise liquid tubes, and individual inlet manifolds. The inlet valves allow individual control of zoned by controlling the amount and interval of coolant supply. However, they require more than 7 mm x 7mm x 15 mm volume each, thus, the outlet manifold must be built around it. The outlet manifold shown in Fig. 55 consists of rectangular shaped outlet pathways. Each zone has a guideway leading to the pathway and thus reducing effects of surrounding outlet pressures. The dimensions shown in Fig. 55 are calculated based on 40 kW heat load for 300 mm Si-IF system.

5.1.2. Prototype fabrication

A single cooling zone prototype was constructed to optimize the process and perform flash cooling tests. A 40 mm x 40 mm size was chosen based on two factors – a zone of 64 5 mm x 5 mm dies can be expected in Si-IF and sufficient structural support for individual chamber. Forging a chamber based on exact specifications proved expensive and so a 2 mm copper sheet brazed around the side of a commercially available copper pin-fin sink (Enzotech MPC 40-21) as shown in Fig. 56a. Initially, a 6.35 mm aluminum plate is used as the top plate. Grooves (3 mm) are

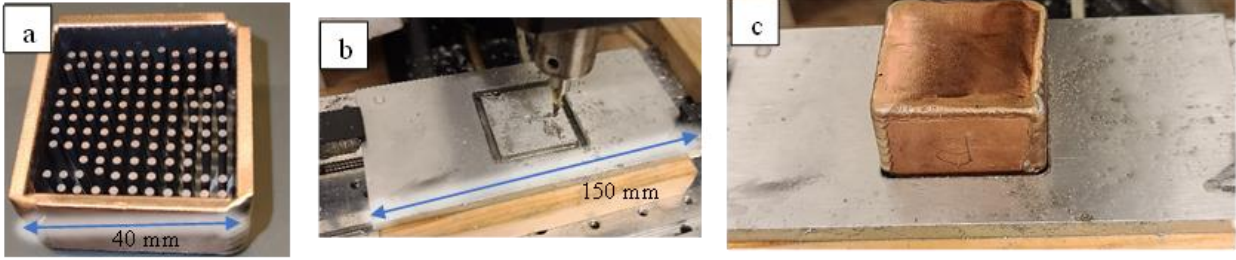


Figure 56: Construction of single flash chamber. (a) Walls attached to a commercial heat sink (b) Machining in top plate for grooves and holes (c) Assembly of copper heat sink with top plate via O-ring.

machined into the plate along with mounting holes on the corners (Fig. 56b). Then pilot holes are drilled for outlets followed by 1/8 in NPT thread tapping. Then a central hole of 1/4 in is drilled for the inlet.

The first step of assembly takes place by placing a 2 mm O-ring into the groove and attaching the copper heat sink into the groove (Fig. 56c). The assembly is flipped, and a surface thermocouple is placed on the backplate. Thermal grease or TIM is applied on the backplate, and the heater is attached. On top of the heater, several layers of insulating tape are applied. Afterwards, a bottom plate which provides as a platform is attached to the back of the heater. The assembly is flipped again, and 1/4-20 UNC bolts are utilized to hold the assembly together gently. The 4 corners bolts are then lightly tightened in rotation to apply uniform compression on the O-ring

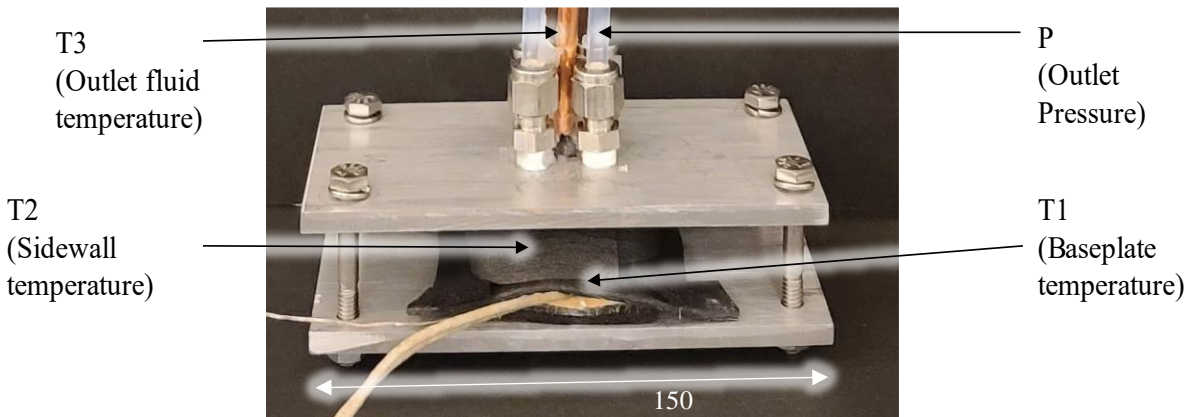


Figure 57: Assembled single flash chamber with inlet and outlet tubes, 3 temperature sensors, 1 pressure sensor, 1 heater cable, and 4 1/4-20 UNC bolts.

which forms the seal. Additionally, a layer of vacuum grease (Dow Corning®) is applied to aid in vacuum seal.

The sidewall thermocouple is attached through the side along with heater connections (Fig. 57). The inlet tube is then attached to the top plate with an epoxy-based sealant. After curing, the Swagelok® fittings are inserted into the tapped outlet holes. The prototype is then inserted into the flow loop described above along with an outlet flow thermocouple.

Several leak checks were performed to ensure that once it is under vacuum and disconnected from pump, the pressure ramp up is less than 0.2 kPa per minute. Some leaks were identified along the seal and threaded fittings and were rectified. As the sidewalls of the flash chamber are not exposed to the atmosphere in a wafer-scale array, the sidewalls were promptly insulated.

5.2. Steady-periodic averaged, effective heat transfer coefficient

At any instant, the heat flux due to flash cooling can be expressed as shown in section 2.2, equation 13, and with the simplification of lumped capacitance from section 4.2,

$$q''_{fc}(t) = h_{fc}(t)(T_b(t) - T_m(t)) \quad (46)$$

Additionally, in the absence of continuous information of $T_m(t)$, the heat flux can be expressed in the form of effective heat transfer coefficient as described in section 2.2,

$$q''_{fc}(t) = h_{eff}(t)(T_b(t) - T_{in}) \quad (47)$$

where T_{in} is the inlet temperature of methanol to the input valve. Since the test equipment is maintained at ambient conditions, it is assumed that T_{in} is constant 25 °C for all test cases. Application of steady-periodic averaging on (15) gives the following expression for averaged heat transfer coefficient:

$$\langle h_{eff} \rangle = \frac{\langle q_{fc} \rangle}{\langle T_b \rangle - T_{in}} \cong \frac{\langle q_{fc} \rangle}{\langle T_b \rangle - 25} \quad (48)$$

The average effective heat transfer coefficient is a useful metric to compare different flash cooling scenarios with required heat transfer coefficient and other cooling approaches for equivalent geometry (section 2.5). The steady-periodic averages combined with lumped capacitance analysis enables the calculation of these parameters for each individual pulse of flash cooling.

5.3. Prototype results

The heat loss was about 0.6 W/K before insulation and 0.4 W/K after insulation. The presence of aluminum on both sides of heat sink instead of stainless steel increases the heat loss as expected. The TDU prototype developed in previous section was tested under flash cooling with the parameters described in Table 9. The experimental procedure described in section 3.1 specified three input parameters for the experiments – Power supplied to the heater, P , volume of methanol injected per pulse, v_p , and time interval between consecutive pulses, t_p . Additionally, five sensor outputs are recorded at each time step at 10 Hz. Most important outputs for a surrogate model include T_b, P_o .

At steady-periodic conditions, the net q_{fc} obtained from equation 2 is an estimate for flash cooling. The details of steady-periodic conditions can be found in [13]. These test conditions also allow us to identify key limits for this flash cooling architecture including the transition to pool boiling at low heat fluxes. Each test run triggers

flash cooling specified as base temperature approaches 40 °C.

First, a 22 W heating condition is used to analyze the steady-periodic conditions and

Table 9: Parameter selection for flash cooling with TDU prototype

Parameter \ Selection	I	II	III	IV
Power, P (W)	10	22	44	
Volume, v_p (mL)	0.6	1	1.5	2
Interval, t_p (s)	40	20	10	

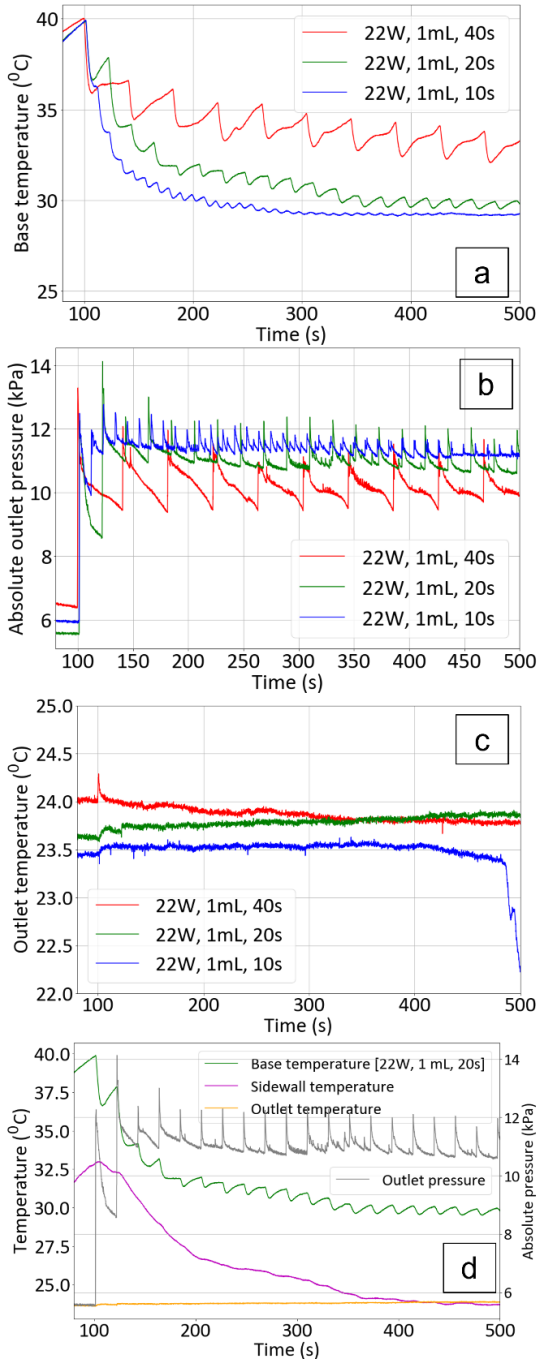


Figure 58: Steady-periodic pulse testing with 1 mL methanol. (a) Temperature profile for different pulse intervals for 22 W heating. (b) Outlet pressure indicating chamber conditions. (c) Outlet temperature clearly indicating pooling of liquid inside chamber for 10s pulse interval. (d) The plot shows behavior of sidewall temperature sensor for 20s pulse interval.

compare it at three different time intervals at a constant 1 mL volume condition (Fig. 58). The first cooling pulse itself causes significant decrease in temperature in all three cases. However, the outlet pressure is a bit higher for the 10s condition, thus influencing the second pulse. Similarly, as the pulses progress, the 20s condition also has slightly higher pressure that is similar to 40s condition. The temperature profiles asymptote toward different steady-periodic temperatures as expected. Even though the 10s condition appears steady-periodic at this low heating, the liquid methanol has started to pool in the chamber until a point where the actual flash process is happening at the outlet of chamber rather than near the inlet tube. This is visible from sudden temperature drop in the outlet fluid temperature (Fig. 58c).

Second, similar tests were repeated with 44 W heating. Similar to 22 W heating, at 10s pulse interval, liquid methanol starts to accumulate. Contrary to the 22 W cases, the

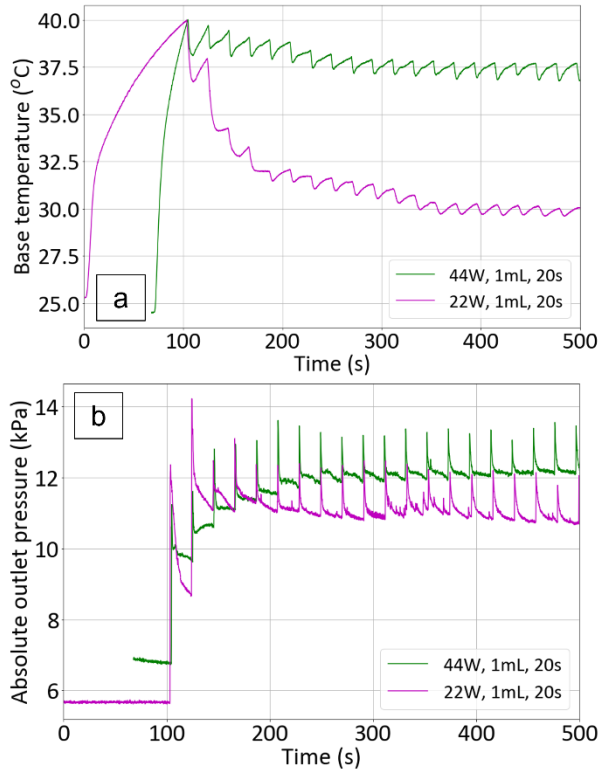


Figure 59: Comparison between 22W and 44W testing for similar cooling conditions

both reach steady-periodic conditions as shown in Fig. 59 with expected increase in base temperature for 44W.

Third, 44 W heating was studied with 20s intervals using different amount of methanol injections into the flash chamber (Fig. 60). At 0.6 mL per pulse, the temperature kept rising as expected due to the low volume of coolant, and at 1- and 1.5-mL condition it achieved steady-periodic conditions without significantly compromising outlet pressures; it is also noted

temperature is not steady-periodic for 40s frequency but increasing due to lack of sufficient cooling. When 20s pulse intervals are compared,

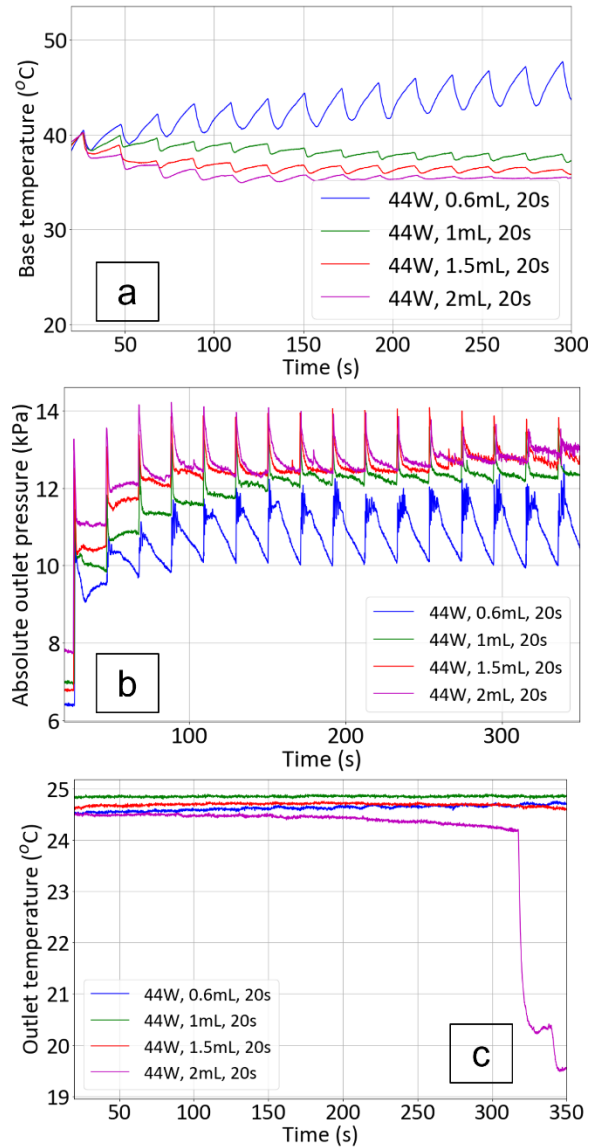


Figure 60: Different volume of methanol every pulse with 44 W heating and 20s interval.

- (a) Different steady-periodic temperatures observed.
- (b) Consistent pressure fluctuations.
- (c) With 2 mL methanol injection significant pooling of liquid in the chamber.

Table 10: Steady-periodic analysis with effective heat transfer coefficient calculations as described in sectioned 5.2

Case	Power, P	Interval, t_p	Volume, v_p	Outlet pressure, $\langle P_o \rangle$	Base temperature, $\langle T_b \rangle$	Effective heat transfer coefficient, $\langle h_{eff} \rangle$	Observed average cooling, $\langle q_{fc} \rangle$	Cumulative Efficiency, η
	(W)	(s)	(mL)	(kPa)	(°C)	(W/m ² K)	(W)	
1	22	40	1	Not Steady-periodic until 500s				
2	22	20	1	11	30.3	2968	20	0.29
3	22	10	1	11.4	29.4	3644	20	0.16
4	44	20	0.6	Not steady-periodic until 500s				
5	44	20	1	12.4	37.6	2444	39	0.56
6	44	20	1.5	12.8	36.2	2791	39	0.38
7	44	20	2	12.8	35.4	3032	40	0.29

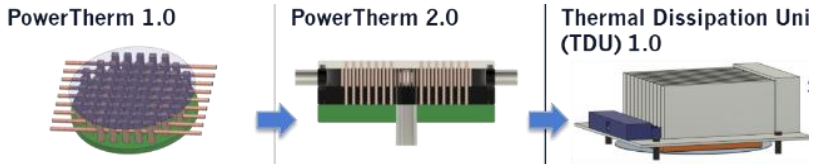
that the peak average temperatures for these conditions is low – only about 37 C. However, with 2 mL at 20s pulse intervals, similar trends are observed compared to 1mL at 10s pulse intervals leading to formation of a liquid pool in the chamber. Table 10 provides updated information on TDU preliminary data corresponding to section 5.2. The effective heat transfer coefficient is evaluated for each steady-periodic case. Chapter 6 introduces extensive testing and analysis for TDU prototype.

5.4. Comparison between cooling architectures

The preliminary results for the three architectures for Si-IF provide a comprehensive outlook of each architecture’s advantages and limitations (Table 11). By comparing the steady-periodic averages at similar input parameters, like the example shown in Table 12, an overall qualitative analysis is obtained.

PT2 architecture has several advantages over the PT1 architecture including lower operating temperatures and temperature fluctuations. However, PT2 does lack local control of cooling. TDU incorporates advantages of both designs and provides optimal solution. With similar power and heat flux input, TDU architecture shows significant reduction in average base temperature, average temperature fluctuation in steady -periodic condition, and response delay.

Table 11: Qualitative comparison of three architectures for flash cooling of the Si-IF



	PT1	PT2	TDU
Arrangement	Block and tube	Wafer-scale pin fin chamber	Array of segmented pin fin chambers
CTE mismatch	Medium	Low	High; gap between zones
Segmentation	No	No	Yes
Zonal control	Yes	No	Yes
Response time (s)	2 - 10	0.5 - 4	0.1 - 1
Base temperature, $\langle T_b \rangle$	High	Medium	Low
Temperature variations, ΔT_b	High	Medium	Low

The increase in cumulative efficiency and effective heat transfer coefficient highlights the improvement in cooling performance due to architectural changes in TDU. While increasing the power input to TDU (shown in Table 12, rows 3 to 5), the base temperature is increasing. Due to faster pulse timing the temperature fluctuations have significantly reduced. However, due to higher effective heat transfer coefficient, the cumulative efficiency is higher, and the average base temperature is within acceptable range.

Table 12: Comparison of steady-periodic averages observed at similar input parameters for different representative prototypes

Prototype	Case (P, v_p, t_p)	Average base temperature, $\langle T_b \rangle$ (°C)	Average temperature fluctuation, $\langle \Delta T_b \rangle$ (°C)	Cumulative efficiency, η	Delay (s)	Steady-periodic averaged, effective heat transfer coefficient, $\langle h_{eff} \rangle$ (W/m ² K)
PT1	(18 W, 1 mL, 20s)	87	3.6	0.2	4.6	500
PT2	(22 W, 1.5 mL, 20s)	64	1.2	0.2	1.7	500
TDU	(22 W, 1 mL, 20s)	30	0.5	0.4	0.9	4000
TDU	(100 W, 0.2 mL, 2s)	38	0.1	0.6	0.6	6000
TDU	(200 W, 1 mL, 5s)	48	0.1	0.7	0.6	7000

Chapter 6: Surrogate modeling for dynamic flash cooling

6.1. Dynamic flash cooling

Flash boiling from the injected liquid is inherently transient because the rate of phase change decays with time, and the pulse nature of cooling loop established in Chapter 3, makes it unique to implement dynamic cooling. The need for dynamic cooling is detailed in section 1.2. There are two components to implementation of dynamic cooling – adaptation to different heat flux inputs, and prediction capability to anticipate thermal response to mitigate transient spikes.

6.1.1. Anticipatory cooling

The flash cooling approach allows the possibility of anticipatory cooling – i.e., performing a flash slightly before the initiation of a heating spike to decrease peak die temperatures. Anticipation time is therefore an important metric for adaptive heat loads. The effect of anticipation is discussed in section 1.2, and it is shown that non-dimensional temperature peak should decrease with increase in anticipation time (Fig. 61). The validation of this phenomenon for the TDU prototype was done using a set of experiments with 22 W heating at room temperature

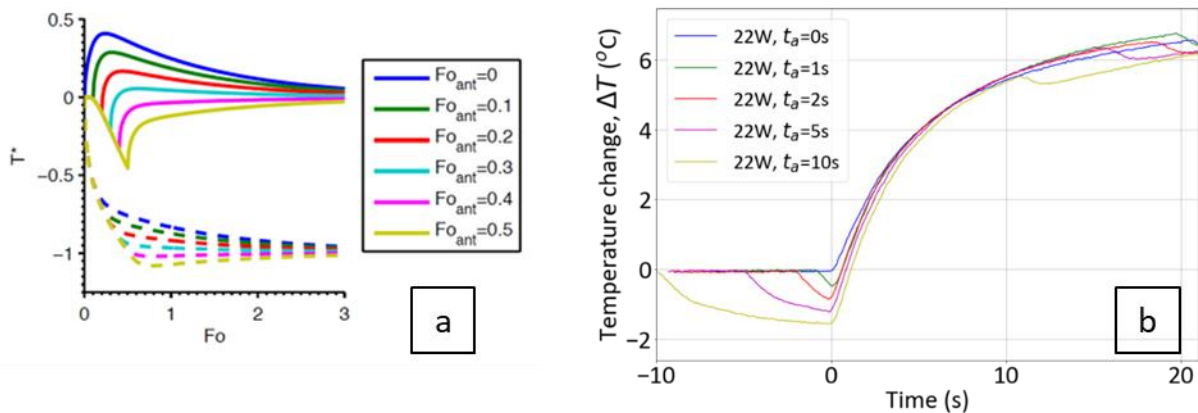


Figure 61: Demonstration of anticipatory cooling effect on the TDU prototype. (a) The expected non-dimensional plot as per discussion in section 1.1, Fig. 3 (reproduced from [2]). (b) Temperature change observed under different anticipation times for a 22 W heat input to the TDU prototype demonstrating the reduction in peak temperature observed due to anticipated flash pulse during heat ramp-up.

with 1 mL cooling pulses is explored with anticipation times of 0,1,2,5 and 10 s (Fig. 62). The cooling starts first and then heating is switched on after the anticipation time. For a given heating condition during first flash pulse, the temperature rise can be as high as 1 °C within a total rise of about 6 °C. For lower anticipation times, the reduction in the peak is within the thermocouple tolerance, and thus the first three curves are identical. However, the reduction in peak temperature with anticipation may lead to sub-cooling of a similar magnitude prior to the heating change. The peak temperature experienced by any hot die thus will be reduced due to the anticipation of additional heat load.

6.1.2. Adaptive cooling

The prototype results and architecture description in Chapters 3, 4 and 5, show the ability of flash cooling to operate at different heat fluxes without changes to hardware or requiring long transition time. Table 12 provides a good overview of the capabilities of same flash cooling loop and architecture to operate under different conditions. Section 6.3 will also introduce a detailed model that illustrates the adaptive nature of flash cooling with same architecture. The prototype results in section 5.2 also demonstrates the adaptive nature: Fig. 58, 59 and 60, show the capability to change pulse interval, manage different heat fluxes, and change the pulse volume respectively as needed to achieve steady-periodic conditions.

The test data gathered from 22 W and 44 W tests described in section 5.2 was utilized to design heating ramp-up tests (Fig. 62). The TDU prototype reaches a steady-

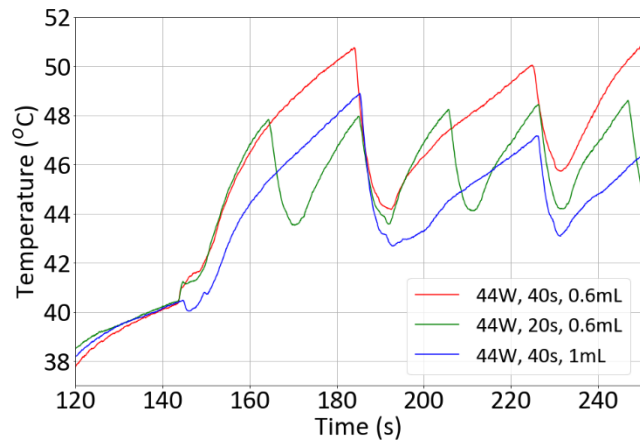


Figure 62: Ramp-up test from 22 W to 44 W under 3 different conditions

periodic condition at 22 W (0.6 mL, 40s) and then through the LabVIEW control, the heater is suddenly ramped up to 44 W. The temperature increases significantly in all three cases shown; however, as cooling conditions are changed simultaneously, we expect different steady-periodic temperatures. The maximum temperature observed by the dies is more significant than average temperature in such conditions. The increase in pulse interval to 20 intervals allows base temperature to stay below 48 °C as compared to 50 °C after the first pulse. Similarly, increasing the amount of methanol injected in the first pulse allows base temperature to remain below 49 °C. Also, the plot provides insight into the different initial slopes of two different cooling adaptations. Increasing the methanol amount led to a faster drop in temperature compared to decrease in pulse interval. However, due to higher pulse interval it leads to higher temperature over time. Thus, we have explored both ways of adapting the cooling method to heating in a crude yet insightful manner.

6.2. Implementation of surrogate modeling

The experimental procedure described in section 3.1 specified three input parameters for the experiments – Power supplied to the heater, P , volume of methanol injected per pulse, v_p , and time interval between consecutive pulses, t_p . Additionally, five sensor outputs are recorded at each time step at 10 Hz. Most important outputs for a surrogate model include the base temperature of the cooling architecture, T_b , and the outlet pressure, P_o (Fig. 63). Additionally, for the TDU prototype the sidewall temperature, T_s , and the outlet fluid temperature, T_o , are also monitored.

A surrogate model may be needed for system-design due to lack of simulation or experimental data, or in order to get first approximate prototype system. Since flash cooling is inherently transient, it requires processing of transient data under steady-periodic testing as specified in section 3.1 and developing a steady-periodic surrogate model using analysis in section

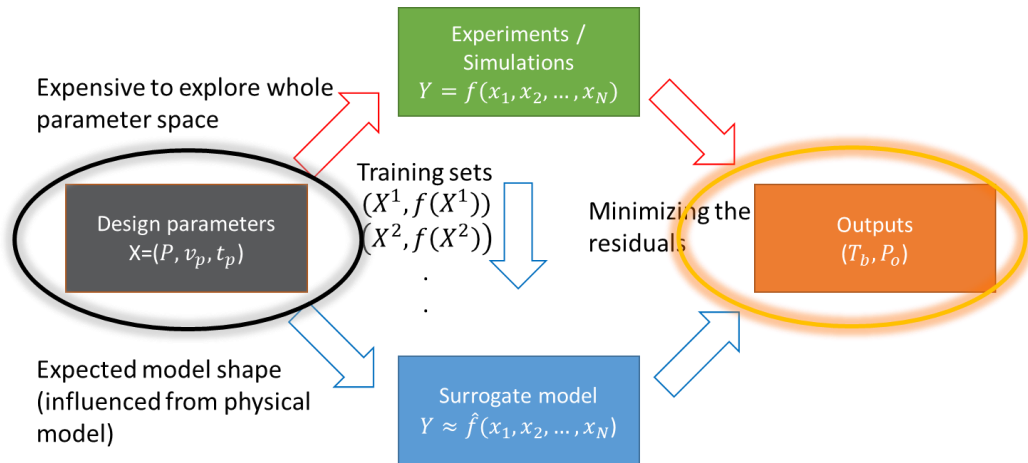


Figure 63: Surrogate model workflow for flash cooling experiments as adapted from the general workflow described in section 2.4.3, Fig. 26.

3.2. The details of processing the data are included in section 6.2.3. Additionally, the steady-periodic test data developed in the process can be utilized to generate an approximate transient model for flash cooling under steady-periodic conditions. The details are included in section 6.2.1.

A surrogate model may also be needed to understand the thermal dynamics involved with flash cooling architecture. It allows engineers to understand the transient characteristics and response of the system to different temporal scenarios. The dynamic cooling described in section 6.1 can be achieved with enough information to adapt the cooling parameters obtained from - system-design model, however, how, and when to adapt is determined by the transient models. Additionally, sensor information may not be accessible as fast as the analysis during system-design or prototyping, thus transient model also enables short prediction windows as shown in section 6.3.3.2.

6.2.1. Simplified steady-periodic models for system-design

The simplified surrogate model for system-design assumes steady-periodic conditions as described in the previous section. The surrogate model thus obtained provides a correlation between averaged outputs and input parameters. This can be further developed into a flash cooling

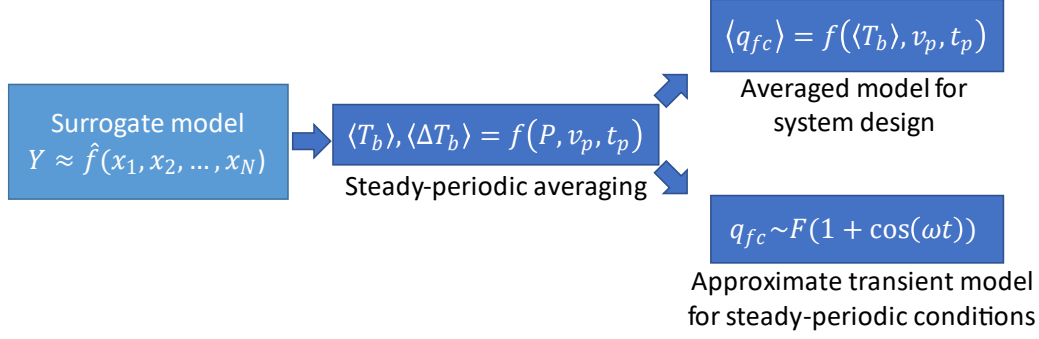


Figure 64: Steady-periodic surrogate modeling approach for system-design

model that predicts average cooling rate based on (40) and (41) as shown in Fig. 64. This process is applied to detailed analysis of TDU prototype in section 6.3. The prototype results of flash cooling shown in Chapter 3, 4 and 5 also employs steady-periodic averaging and the results are tabulated in Table 12.

6.2.1.1. Dominant frequency-driven model

Another approach explored in this work is assuming that steady-periodic conditions of flash cooling at constant heating can be treated as combination of cooling waves. It is therefore a forced function of flash cooling; however, this analysis assumes a single frequency for this forcing function. In dominant frequency-driven analysis, it is assumed that flash cooling is the driving force for the temperature changes in the heat sink and the device surface. Additionally, only the steady-periodic data as defined in section 3.3 is considered for this analysis. Starting with (43) and using $\Theta = T_b - T_a$, and assuming C_{th} and G_{loss} are constants over the range of each steady-periodic experiment,

$$P = C_{th} \frac{d\Theta}{dt} + G_{loss}\Theta + q_{fc} \quad (49)$$

Assuming $q_{fc} = F(1 + \cos(\omega t))$, and $m = \frac{G_{loss}}{C_{th}}$ = constant, the final solution obtained for the non-

homogeneous equation is:

$$T_b(t) - T_a = -\frac{F}{G_{loss} * \sqrt{1 + \left(\frac{\omega}{m}\right)^2}} \cos\left(\omega t - \arctan\left(\frac{\omega}{m}\right)\right) + \frac{P - F}{G_{loss}} \quad (50)$$

The experimental data includes transient data of the temperature (T_b) and the frequency is known as $\omega = 2\pi/t_p$. So the unknowns, F , G_{loss} and C_{th} can be fitted using curve-fitting.

The solution is of the form: $T_b(t) = A \cos(\omega t - \phi) + B$; $\phi = \arctan\left(\frac{\omega}{m}\right)$. When expressed in terms of observable averaged quantities,

$$\langle T_b \rangle = B = T_a + \frac{P-F}{G_{loss}}; \langle \Delta T \rangle = -2A = \frac{2F}{G_{loss} * \sqrt{1 + \left(\frac{\omega}{m}\right)^2}}; Delay = \phi * \left(\frac{t_p}{2\pi}\right) \quad (51)$$

where, delay is the response time between the start of a flash cooling pulse to the start of change in base temperature. For steady-periodic conditions with the dominant driving frequency assumption, delay is simply the lag caused due to the phase difference between driving flash cooling and the base temperature obtained through above equation.

Alternatively, the unknown variables can also be determined by utilizing already evaluated steady-periodic averages as described in section 3.3. Multiple data sets were analysed using both techniques, and the difference in parameters obtained was negligible. Thus, curve fitting approach is used independently for this analysis. Most important metric out of this analysis is the delay or the response time obtained for different prototypes and included in section 6.3.

6.2.2. Transient model for anticipatory control

For transient analysis, it is critical to obtain lumped capacitance parameters starting with (44). To determine the heat loss coefficient, G_{loss} , a set of steady-state heating experiments are

performed at different temperatures to obtain $G_{loss}(T_b)$. With absence of flash cooling and no change in temperature, the steady-state power, $P_{steady-state}$, is completely lost through loss as

$$P_{steady-state} = G_{loss}(T_b)(T_b - T_a) = \{a * T_b^3 + b * T_b^2 + c * T_b + d\}(T_b - T_a) \quad (52)$$

The coefficients a , b , c , and d are obtained by curve-fitting, and $G_{loss}(T_b)$ can be obtained for each prototype. Similarly, utilizing heating portions of each experiment at constant power, where $q_{fc}(t) = 0$, and dropping the dependence of time for representation on all physical variables,

$$P = C_{th}(T_b, P) \frac{dT_b}{dt} + G_{loss}(T_b)(T_b - T_a) = \{e * P + f * T_b + g * PT_b + h\} \frac{dT_b}{dt} + \{a * T_b^3 + b * T_b^2 + c * T_b + d\}(T_b - T_a) \quad (53)$$

By utilizing previously known function of $G_{loss}(T_b)$ from (49) and known power supplied to the heater, $C_{th}(P, T_b)$ is obtained by curve-fitting the coefficient e , f , g , and h . Thus, the magnitude of flash cooling at any time can be estimated as:

$$q_{fc} = f \left(P, T_b, \frac{dT_b}{dt} \right) \quad (54)$$

$$q_{fc} = P - \{e * P + f * T_b + g * PT_b + h\} \frac{dT_b}{dt} - \{a * T_b^3 + b * T_b^2 + c * T_b + d\}(T_b - T_a) \quad (55)$$

Different forms of transient model can be implemented depending on the specific architecture, lumped capacitance parameters and level of accuracy required. For demonstration of these tools, the fitting functions are kept simple with linear combination of physical parameters with respective exponents.

6.2.2.1. Run-time models

The prediction for $q_{fc}(t)$ for any experiment with given input parameters and sensor data but independent of heat input provided is critical for a run-time model. In the absence of input

power, the outlet pressure provides the information to assess the ability for flash cooling in that instant. Thus, the expression for flash cooling from equation A can now be written as

$$q_{fc}(t) = f(T_b, v_p, t_p, P_o)$$

$$q_{fc}(t) \approx h(T_b, v_p, t_p) * (T_b - T_{sat}@P_o) \quad (56)$$

A simple linear model is shown below that incorporates current input parameters to the system (v_p, t_p) and current outputs ($T_b(t), P_o(t)$) to predict current cooling -

$$q_{fc}(t) = (a_1 * T_b(t) + b_1) \left(c_1 * \left(\frac{v_p}{t_p} \right) + d_1 \right) (T_b(t) - (e_1 * P_o(t) + f_1)) \quad (57)$$

This model can then be used for run-time prediction combined with other data assimilation techniques described in section 2.3.4. Another model that can be utilized is dependent on the amount of time elapsed from the last pulse start ($t_e = t_{total} - t_{pulse,start}$),

$$q_{fc}(t_e)|_{pulse} = f(T_b, v_p, t_p, t_e, P_o) \quad (58)$$

This model considers the effect of the starting state of the pulse and the current pulse parameters to predict the behavior for rest of the pulse. However, this model is not explored further in this work.

6.2.3. Jupyter tools and file management

The analysis described under the surrogate modeling in this chapter is performed with the help of a file and data management plan, and python codes based on Jupyter notebook. The overall flow is shown in Fig. 65. The details of the sensor data and OneNote journal are detailed in section 3.1. The transient data is imported into a utility code (Appendix A) which performs following tasks:

- Data smoothening and calculate derivatives as per global control.

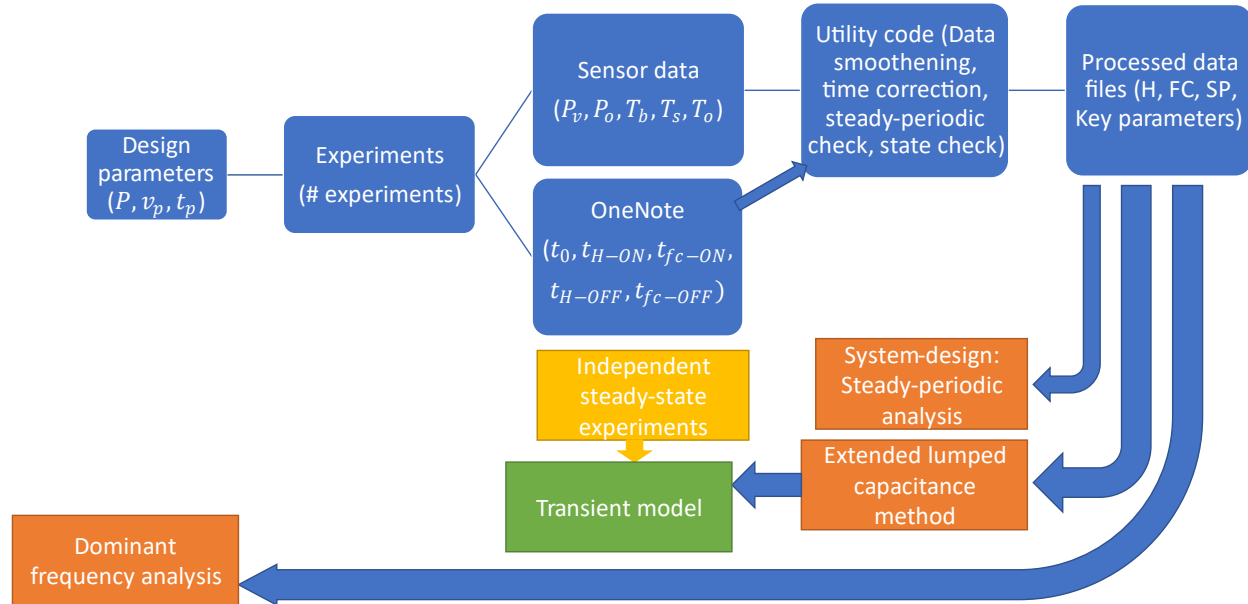


Figure 65: File and data management for surrogate modeling

- Data splicing into different zones: Heating only, heating and flash cooling, steady-periodic (if applicable).
- Correction of pulse timing based on pressure pulses and verification with OneNote data.
- Estimate heating and cooling ON/OFF times and verification with OneNote observations.
- Calculate average pulse values and verify if steady-periodic conditions are reached.
- Define the state of the experiment as detailed in section 6.3.1. The color scheme is followed throughout the detailed analysis results in section 6.3.

Once all the files for a certain prototype are passed through the utility code, the parameters file is used to collect key information from all the processed data files. This code (Appendix B) provides following information:

- Distribution of states as a function of input parameters

- Distribution of cooling parameters required as a function of either required operating temperature or required heat input.
- Steady-periodic analysis: Averages and efficiencies calculated from different utility files.

Following the steady-periodic analysis, an estimation code is used to determine the transient parameters with the help of curve-fitting (Appendix C). It provides following information:

- Provides correlated G_{loss} and C_{th} from all data files; subsequently providing $q_{fc}(t)$ as per (53).
- Estimation of $q_{fc}(t)$ as defined in (52) with coolant parameters and independent of power input.

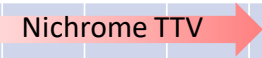
The dominant frequency-driven analysis is performed only on the data files that reached steady-periodic conditions, i.e., states 2 to 4. The code is embedded in Appendix D. The code evaluates the following information:

- F , G_{loss} , C_{th} , and delay/response time from curve-fitting and using steady-periodic data as required in (51).

6.3. Extensive testing and surrogate modeling of TDU prototype

The TDU stands out as the optimal architecture as per section 5.3. Thus, the detailed surrogate modeling is performed on TDU prototype. The data for the surrogate models with the techniques described in previous sections and covers the detailed parameters shown in Table 14. The total number of experiments performed and utilized for this analysis is 30. A wider range of parameters is selected for this analysis compared to prototype testing shown in previous chapters. The heating power is constrained by the availability of commercial heaters. The commercial

Table 13: Parameter space for detailed experiments and surrogate modeling of TDU prototype.

Parameter \ Selection	I	II	III	IV	V	VI	VII	VIII	IX	X
Power, P (W)	22	44	100	150	200	Nichrome TTV 				
Volume, v_p (mL)	1.2	1.1	1	0.9	0.8	0.7	0.6	0.5	0.3	0.2
Interval, t_p (s)	20	10	5	4	3	2	1	2	1	X

heaters described in section 4.4 include 22 W and 200W rates heaters. Thus, maximum heating supplied in the experiments was limited to up to 200W. Several thermal test vehicles designed for this purpose were discussed, however, unavailability of the nichrome on ceramic TTV limited the heating power. The thermal data from these experiments is included in Appendix F.

Similarly, wide range of pulse volume and pulse intervals were considered. It was observed that pulse interval below 1-s produce inconsistent data and run the risk of equipment / control delays significantly altering the analysis. Pulse volume above 1.2 mL was not considered as it led to pooling of water. Overall, the restrictions included maximum heater power limit and fastest pulse interval while still correctly estimating coolant pulse time.

Table 14: Definition and conditions for state of cooling

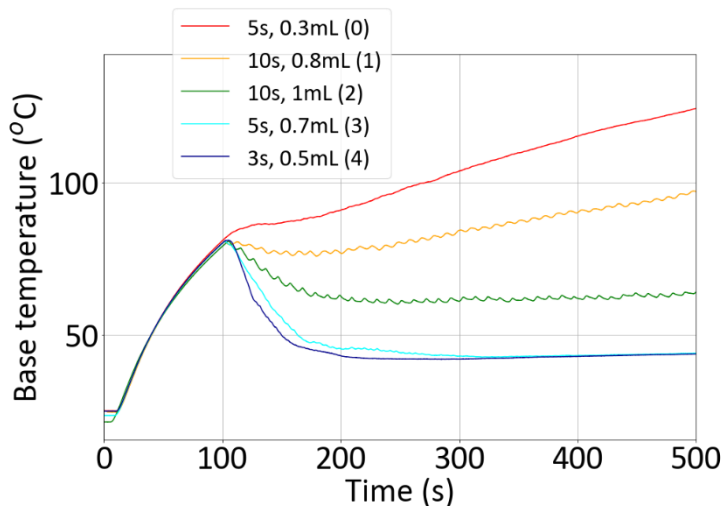
#	State	Condition	Remark	Data used for steady-periodic surrogate model
0	Under-cooling	$T_b > 140^\circ\text{C}$ over 1200s	Conditions not recommended	
1	Marginal under-cooling	$T_b < 140^\circ\text{C}$ over 1200s, $\langle T_b \rangle \neq \text{Steady}$	Acceptable for short duration if $T_b < T_{max}$	
2	Steady-periodic	$\langle T_b \rangle = \text{Steady}$	Higher efficiency, η , but possible ΔT_b	Yes
3	Marginal over-cooling	$\langle T_b \rangle = \text{Steady}$, Liquid droplets	Efficiency, η , is compromised	Yes
4	Over-cooling	$\langle T_b \rangle = \text{Steady}$, Bulk flow	η is compromised Not feasible for continuous operation	Yes

6.3.1. State of cooling

Each experiment outputs data files as detailed in section 6.2.3. The temperature response of the base, T_b , is considered as first filter to understand the behavior and efficacy of flash cooling for that particular set of input parameters. There are 5 categories to bin the set of experiments as mentioned in Table 14. An illustration of the five different categories is provided in Fig. 66. Five pulse volume and pulse interval combinations are used to cool 150 W of heater power.

The color coding and state numbers are kept consistent for all following figures. The case of under-cooling, combination where not enough cooling provided for the TDU, is marked as red (state 0). The acceptable cooling conditions are 2 to 4 where average base temperature is stabilized and flash cooling can be evaluated effectively for the steady-periodic test conditions.

The distribution of states of cooling for the total number of experiments is shown in Fig. 68 with respect to the input parameters. The 3D scatter plot in Fig. 67a provides qualitative trends of distribution of states. As we would expect at higher power powers, more cooling is required to maintain steady-periodic conditions. Density of state of cooling is represented in Fig. 67b. Since



the goal is to understand the limitations of cooling at different conditions, a good spread of states is observed especially for higher input powers.

Figure 66: Sample results for 150 W heating power (0.12 W/mm^2) and with varying coolant parameters showing all 5 different states.

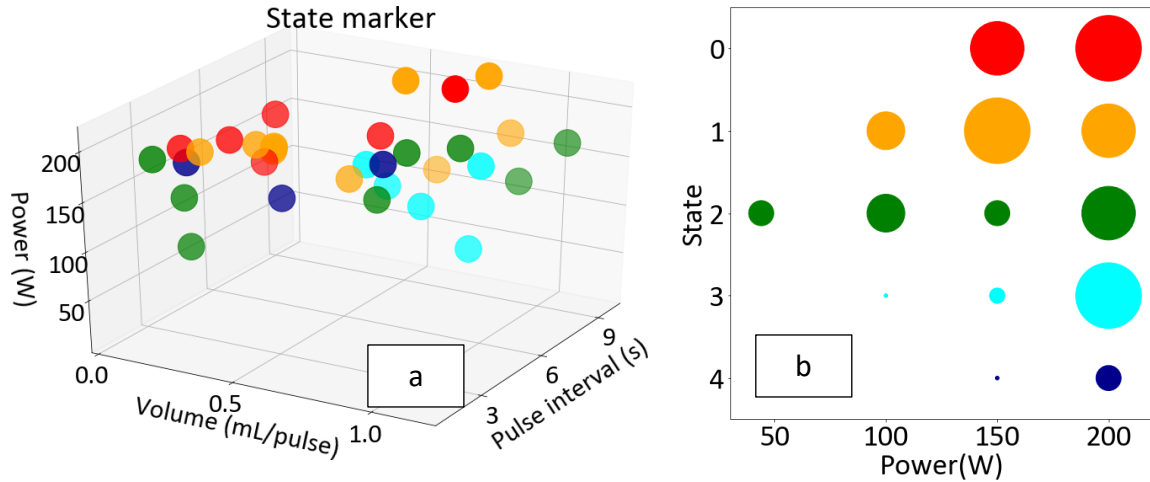


Figure 67: Distribution of State of cooling against input parameters (a) 3D scatter plot highlighting qualitative trends (b) Density of scatter point reflects the relative number of experiments at each power level.

If a specific power level, for example 200 W (Fig. 68a), is chosen and the state markers seen as a function of v_p and t_p (Fig. 68b), then a qualitative trend is observed that higher methanol volume and lower pulse interval provides sufficient cooling. However, the respective combination of the same is not a linear function as would be expected with a flow rate comparison as seen in Fig. 69. It reasserts the importance of understanding the impact of both pulse volume and pulse interval separately for flash cooling as opposed to the standard practice of using flow rate as control parameter for steady-state cooling techniques.

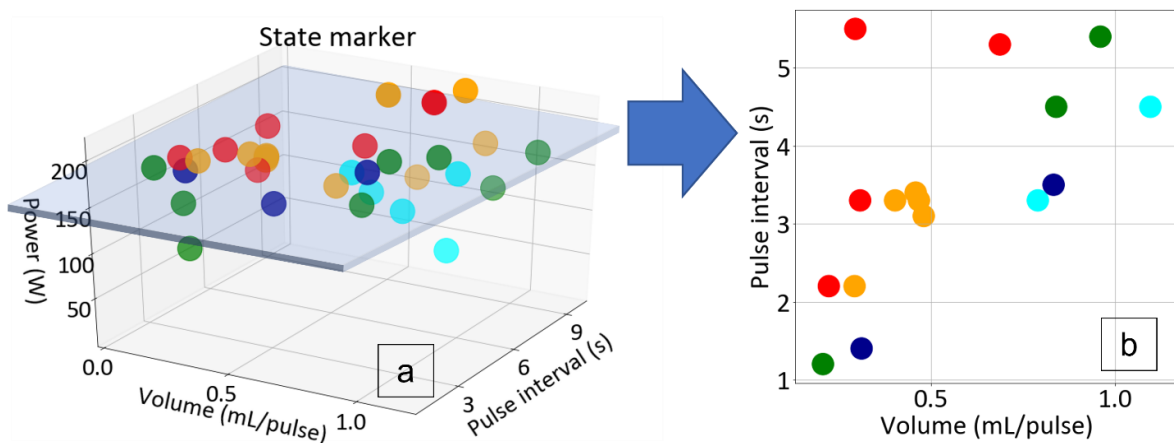


Figure 68: Distribution of state markers at 200 W. (a) Plane cross-section (b) Function of v_p and t_p

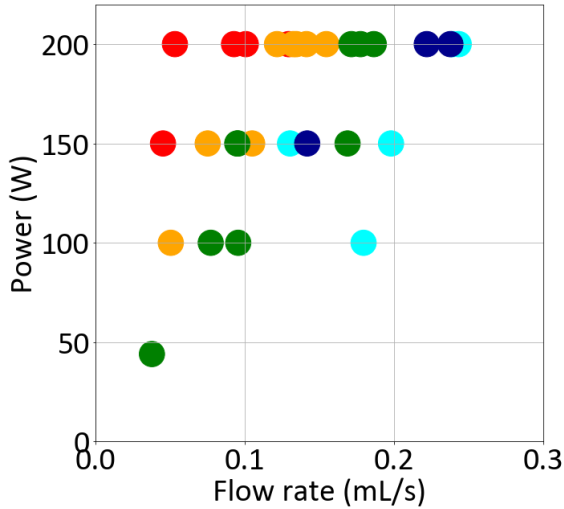


Figure 69: State of cooling at different flow rate and different input power. This data is obtained from the parameter file (Fig. 66).

6.3.2. Steady-periodic model

The data from utility and parameter codes is utilized to perform steady-periodic analysis. This section discusses the states providing steady-periodic conditions, i.e., states 2 to 4. The steady-periodic average base temperature is plotted against input powers (Fig. 70a). The increase in average base temperature is expected with increase in input power. Additionally, several over-cooled cases are also observed that reduce the base temperature further. The variation in base temperature under steady-periodic conditions is considerably high (>1.75 °C) at higher pulse intervals as expected (Fig. 70b). However, below 5-s pulse interval, the variation is fairly consistent. This

cases are also observed that reduce the base temperature further. The variation in base temperature under steady-periodic conditions is considerably high (>1.75 °C) at higher pulse intervals as expected (Fig. 70b). However, below 5-s pulse interval, the variation is fairly consistent. This

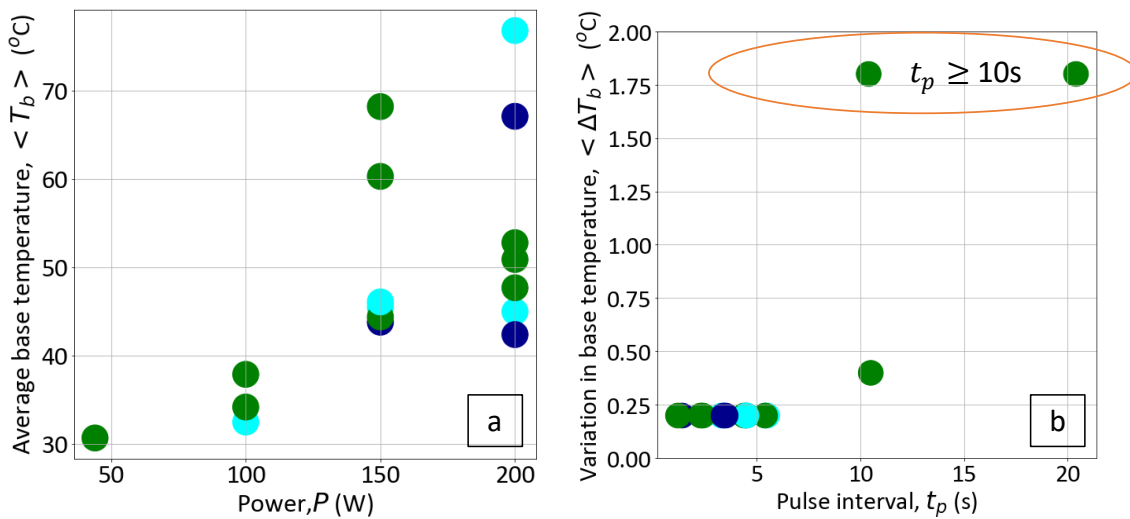


Figure 70: Average base temperature and its fluctuations. (a) Function of power levels (b) function of file number

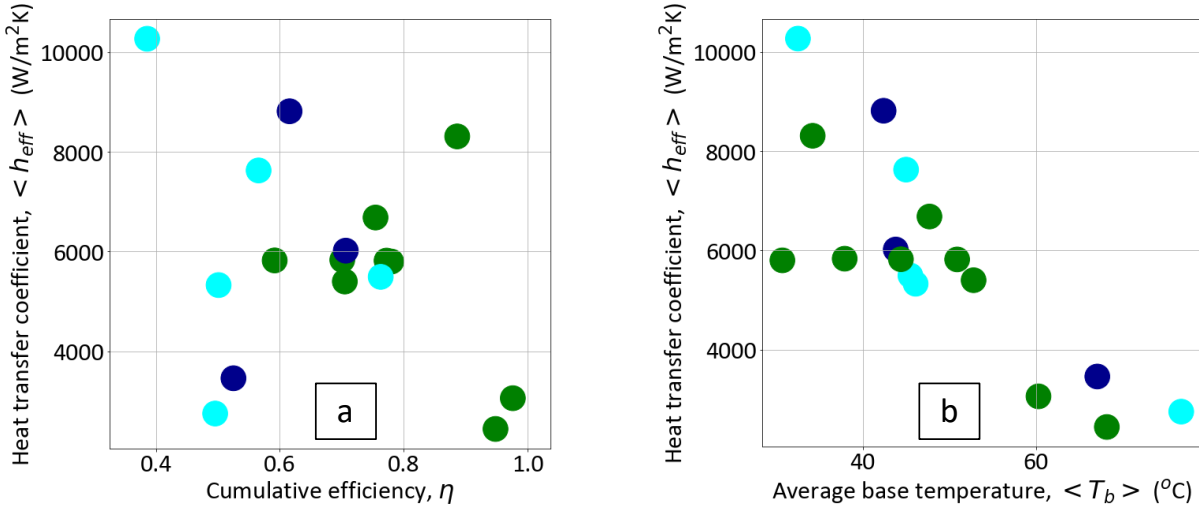


Figure 71: Effective heat transfer coefficient evaluated from steady-periodic averaging is shown here. (a) Higher heat transfer coefficients are obtained at lower cumulative efficiencies for limited power input. (b) The higher base temperature cases indicate lower heat transfer coefficient.

variation is inherent to the transient characteristics of this TDU prototype. Thus, this tolerance should be built within any system-design margins considering that peak temperature $T_b + \Delta T_b$ is less than maximum allowed base temperature for Si-IF.

The average effective heat transfer coefficient obtained by assuming steady-periodic averages as described in sections 3.3 and 6.2 is illustrated in Fig. 71. The cumulative efficiency, the ratio of average cooling rate to the theoretical maximum from the fluid, of each data set can be calculated following steady-periodic averaging as described in section 3.3. The cases that generate higher heat transfer coefficient while retaining high efficiency (Fig. 71a) should be recommended for operation. No general trend can be observed between state of cooling and heat transfer coefficient. There is a clear indication in Fig. 71a that steady-periodic

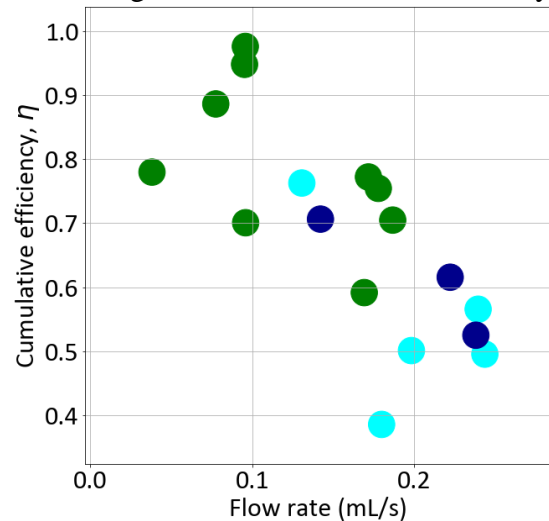


Figure 72: Cumulative efficiency from steady-periodic data compared to effective flow rate obtained.

cases (state 2) have higher efficiency in general compared to over-cooled cases (state 3 and 4). However, in some scenarios the overcooled conditions have the capability to deliver higher heat transfer coefficient. This can be effective in handling larger than expected heat loads for small duration without causing significant effect on overall flow loop. Figure 71b demonstrates that cases with least heat transfer coefficient led to highest average base temperature as expected. The flow rates for over-cooled cases are higher than equivalent steady-periodic cases (Fig. 72), thus leading to lower cumulative efficiency (due to higher theoretical maximum).

A general steady-periodic surrogate model is developed with the help of curve fitting the steady-periodic data as discussed in section 6.2.1. The curve-fitted expression for average flash cooling (independent of input power):

$$\langle q_{fc} \rangle_{general} \approx (47.7 + 0.23 * (\langle T_b \rangle - 25)) * (1.54 + 7.88 * \left(\frac{v_p}{t_p}\right)) \quad (59)$$

This expression is developed with cases in the range of input power from 100 W to 200 W. Fig. 73a demonstrates the curve-fitted surrogate model along with calculated average flash cooling

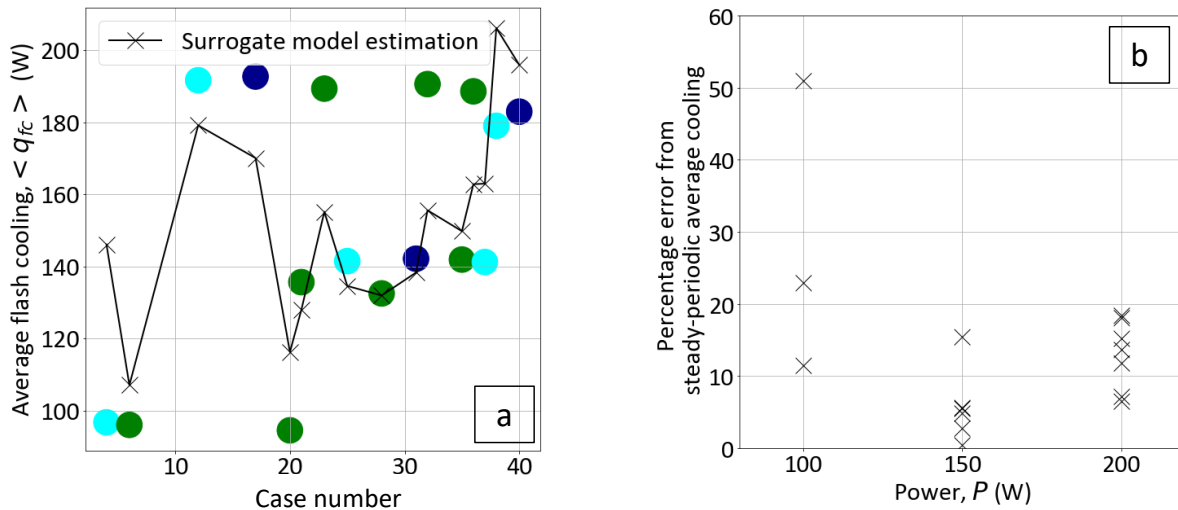


Figure 73: Comparison of average flash cooling between developed surrogate model to the actual values obtained through data averaging. (a) Comparison for states 2, 3 and 4. (b) Percentage error of the surrogate model at different power inputs to the heater.

rates for different cases. Figure 73b shows the percentage error of the surrogate model at different input power. This model consistently predicts the average flash cooling rate within 20% for all cases with ≥ 150 W input power.

6.3.2.1. Dominant frequency-driven model

The dominant frequency-driven surrogate model is introduced in section 6.2.1. The approximate transient model obtained from steady-periodic data is useful to estimate additional parameters that are not available directly through the steady-periodic averaging. The average response time obtained through this frequency-based model can be crucial during design-phase of the system to determine anticipatory controls. A specific example (Case 20) is shown Fig. 74 with steady-periodic model overlapping the original data. The values of curve-fitted variables for this particular case are as follows: $F=93.34$ W, $A=0.15$ °C, and $B=37.1$ °C.

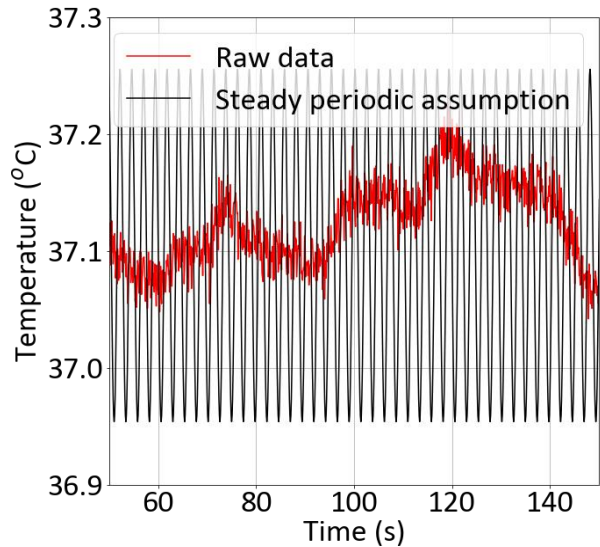


Figure 74: Comparison of base temperature data from dominant frequency-driven steady-periodic model and original data.

The unknowns can also be obtained using steady-periodic averages as described in section 6.2.1.

The variables obtained are shown in Table 15 and are equivalent to those obtained from curve-fitting above.

Table 15: Variables obtained for frequency-driven analysis using steady-periodic averages for a specific experiment (case 20).

Experiment number	Power, P (W)	Pulse interval, t_p (s)	Volume per pulse, v_p (mL)	State	Corrected t_p (s)	Cooling frequency, ω (rad)
20	100	2	0.2	3	2.4	0.42
$\langle T_b \rangle$ (°C)	$\langle \Delta T_b \rangle$ (°C)	B(°C)	F(W)	A(°C)	ϕ (radians)	Delay(s)
37.9	0.1	37.9	93.29	-0.1	1.57	0.6

The dominant frequency-driven model described here provides a good foundation, however, more realistic implementation would require extending the theory to include harmonics. This is a good future direction stemming from the demonstration in this work that can be very useful for design and operation of flash cooling for different architectures.

6.3.3. Transient model

The transient analysis described in section 6.2.2 involves unknown expression for 3 quantities, G_{loss} , C_{th} and q_{fc} . The determination of G_{loss} and C_{th} are facilitated by running separate steady-state heating experiments in absence of flash cooling. In these experiments, the loss through natural convection and radiation are combined as described in section 4.2.

6.3.3.1. Steady-state experiments to determine G_{loss}

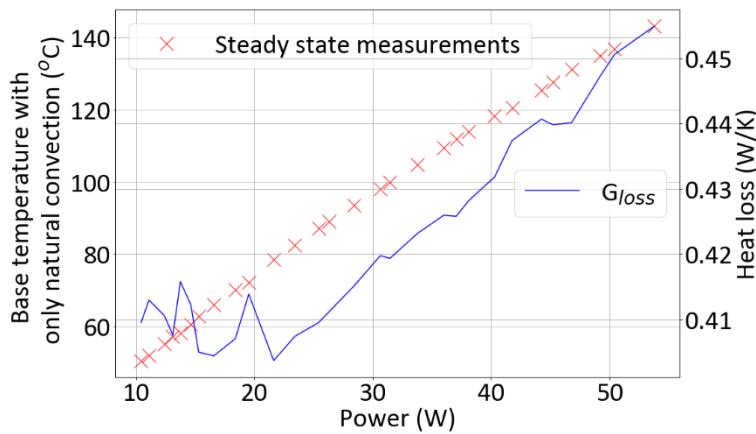


Figure 75: Steady state experiments to determine G_{loss} .

For these experiments, the voltage across the resistive heater is increased in gradual steps. At each step, the base temperature is allowed five minutes to achieve steady-state conditions. The power supplied to the heater is the input parameter as

shown in Fig. 75. The base temperature recorded is shown on the primary y-axis. The increase in temperature is monotonic as expected with increasing power input. The secondary y-axis shows the heat loss coefficient calculated at each step. This data is then curve-fitted to obtain the following relation for G_{loss} :

$$G_{loss}(T_b) = -7.7 \times 10^{-8} (T_b)^3 + 3.0 \times 10^{-5} * (T_b)^2 - 3.1 * 10^{-3} * (T_b) + 0.5 \text{ W/K} \quad (60)$$

The temperature ramp-up data for each step is considered in developing the curve-fitted value of thermal capacitance from (49) and (53):

$$C_{th} = 0.14 * P + 5.21 * T_b - 0.01 * P * T_b + 21 \text{ J/K} \quad (61)$$

6.3.3.2. Estimation of transient cooling rate and heat transfer coefficient

Utilizing the known expressions for the first two terms, flash cooling obtained at any given time, $q_{fc}(t)$, is obtained by using (55):

$$q_{fc}(t) = P - \{0.14 * P + 5.21 * T_b - 0.01 * P * T_b + 21\} \frac{dT_b(t)}{dt} + \{-7.7 \times 10^{-8} (T_b)^3 + 3.0 \times 10^{-5} * (T_b)^2 - 3.1 * 10^{-3} * (T_b) + 0.5\} (T_b - 25) \text{ W} \quad (62)$$

The transient flash cooling based on (62) is graphed for a sample experiment (Case 25) in Fig. 76a. The zoom inset (Fig. 76b) provides an insight on the oscillating nature of flash cooling during individual pulses. The heat transfer coefficient at any point can then be estimated as:

$$h_{eff}(t) = h_{fc}(t) = \frac{q_{fc}(t)}{A(T_b(t) - 25)} \quad (63)$$

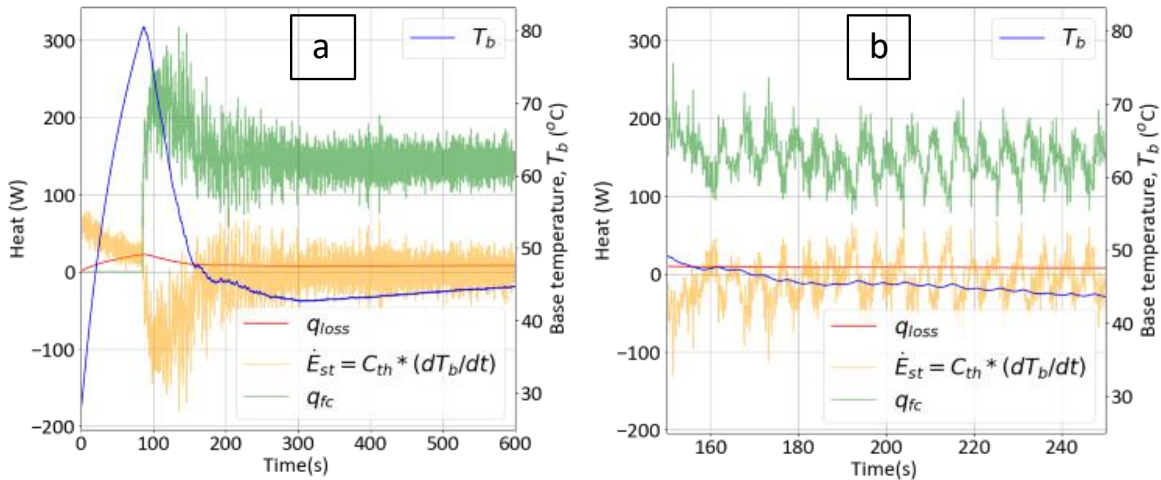


Figure 76: Estimation of flash cooling with curve-fitted parameters at a given input combination. (a) Heat components for complete experiment are shown along with recorded base temperature. (b) Focusing near 200-s timestamp, better visualization of individual pulses.

These calculations enable the calculation of peak heat transfer coefficient provided by flash cooling both during initial transients, and during steady-periodic conditions. The sample case used to show the calculation of transient flash cooling rate is also used to demonstrate the calculation shown above. The plot for effective heat transfer coefficient at any given instant using the transient model shows the large variation of the parameter throughout the experiment (Fig. 77a). The initial transients are large as flash cooling is initiated only after the base temperature has reached a certain threshold, allowing to provide additional cooling. The transient nature of the heat transfer coefficient during individual pulses can be seen in Fig. 77b. The peak initial cooling provided for each case is presented in Fig. 78.

Each flash cooling pulse starts with a high value when methanol is injected into the flash chamber, and then reduces over time as the coolant leaves the chamber until the next pulse. This behavior is more consistent under steady-periodic circumstances, and for all the cases mentioned in previous section where a steady-periodic condition was achieved, a steady-periodic averaged effective heat transfer coefficient was calculated. Utilizing the transient model for $h_{fc}(t)$ with (48)

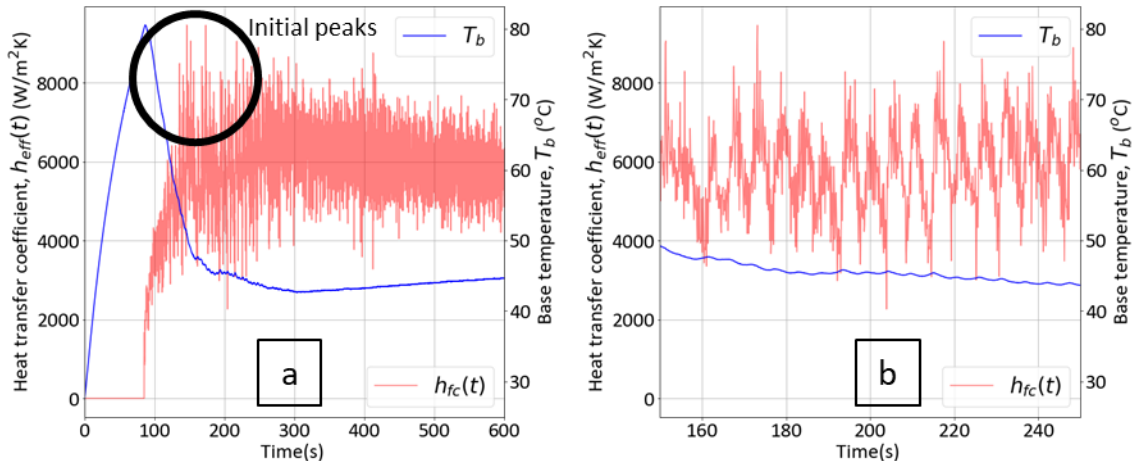


Figure 77: Estimation of effective heat transfer coefficient based on the transient model. (a) Data for first 600-s of experiment, highlighting the initial peaks obtained at higher temperature. (b) Focusing near 200-s timestamp to understand the behavior for individual pulses.

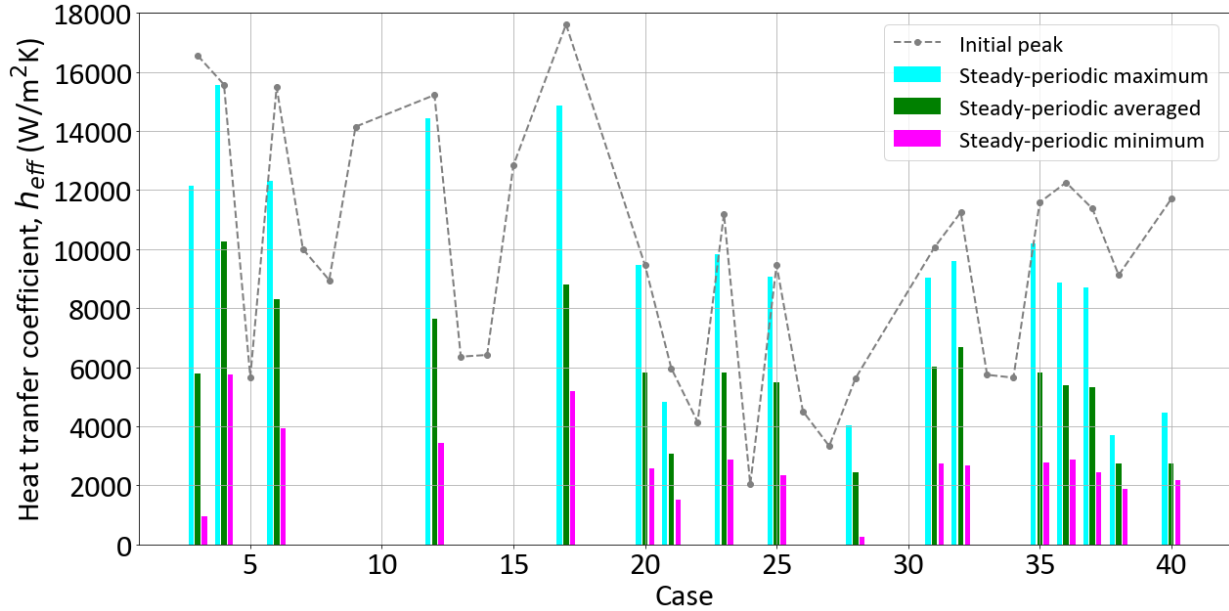


Figure 78: Estimated effective heat transfer coefficient utilizing both steady-periodic and transient models as applicable (section 6.1) for each case.

for $\langle h_{eff} \rangle$, maximum and minimum values for each pulse, and for the entire steady-periodic data in each case, can also be evaluated. The values are provided in Fig. 78 and indicate the expected trend of wide gap between the maximum and minimum heat transfer coefficients for each steady-periodic case. Several cases (3, 21 and 28) show very low minimum heat transfer coefficient indicating the lack of coolant during the later stages of the pulse. This indicates that the flow conditions are moving towards dry out condition (section 2.1) and lead to higher average base temperatures to attain sufficient cooling rates.

Under constant heating condition with heater power at 200-W, a monotonic trend is observed between the steady-periodic averaged heat transfer coefficient and base temperature as expected (Fig. 79). This provides information to select the cooling conditions, volume per pulse and pulse interval, that would provide the highest heat transfer coefficients. The information provided for initial peak coefficients would be very useful to provide short interval high-heat flux cooling while the steady-periodic information is utilized for steady conditions. The peak effective

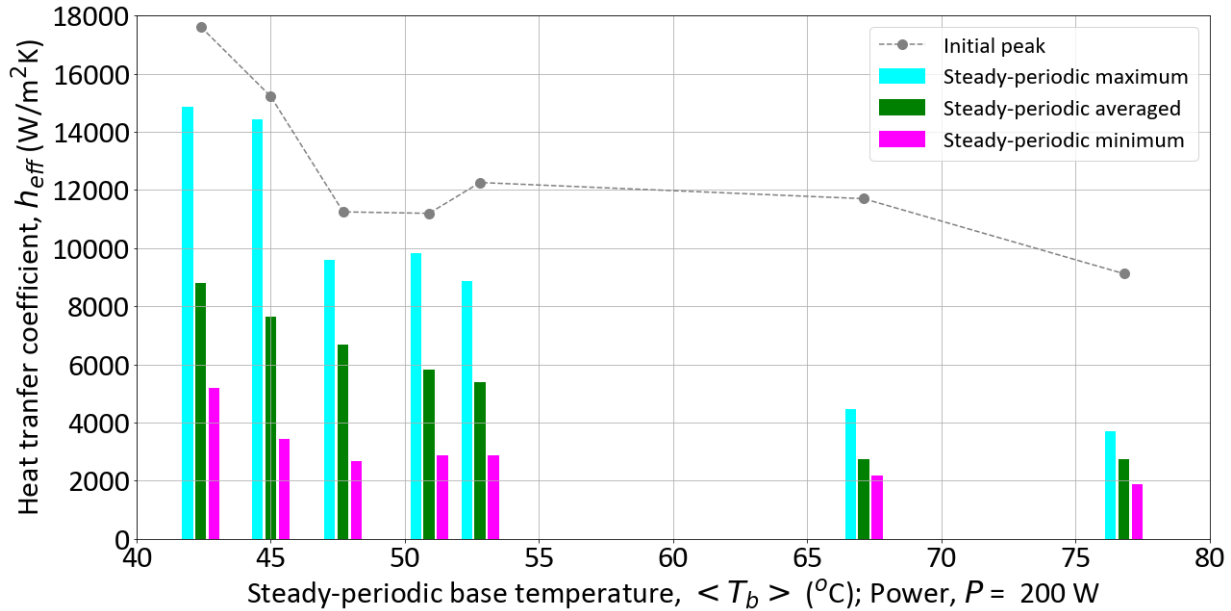


Figure 79: Estimated effective heat transfer coefficient compared to the steady-periodic base temperature at constant heat input of 200-W.

heat transfer coefficients evaluated during the extensive testing performed is as high as $\sim 18,000$ $\text{W}/\text{m}^2\text{K}$ even at lower heat flux conditions of up to 0.2 W/mm^2 . The cooling effect is higher high flow rate cooling with single phase water with pin fin configuration. However, due to limited heat flux available due to testing, the steady-periodic averages are limited to $\sim 10,000$ $\text{W}/\text{m}^2\text{K}$ which is comparable to high flow rate water cooling solution. However, since the base temperature is still significantly lower than upper limit of 85 $^{\circ}\text{C}$, and low flow rate (with high cumulative efficiency), the results indicate that flash cooling in this configuration can handle much larger heat flux in future work.

6.3.3.3. Sample run-time model

A sample run-time model is also developed for the same experiment (case 25) as above. A curve-fitted expression is developed for flash cooling that is independent of incoming heat by collecting data from all the experiments as shown in (57):

$$q_{fc}(t) = (1.7 \times 10^{-2} T_b(t) + 7.1) \left(-1.1 \times 10^{-2} \left(\frac{v_p(mL)}{t_p(s)} \right) + 0.1 \right) * (T_b(t) + (7.0 \times 10^{-3} P_o(Pa)(t) - 65.3)) \quad (64)$$

Utilizing this expression, we can create a predictive model of flash cooling dependent on current sensor data (Fig. 80). The prediction for base temperature at the next timestep ($T_{b,n+1}$) a simplified backward differential form is used on (44) at any timestep n:

$$\frac{T_{b,n+1} - T_{b,n}}{dt} = \frac{P_n - q_{fc,n} - G_{loss}(T_{b,n})(T_{b,n} - T_a)}{C_{th}(T_{b,n})} \quad (65)$$

where $q_{fc,n}$ is evaluated using (64) at timestep n.

The prediction critical when the sensor data is unavailable at every time step for run-time control of flash cooling. Intermediate values can be approximated using this run-time model. Thus, additional plots are added with sensor data available at every 10- and 100-time steps at 10 Hz operation. It is observed that error in estimation is less than 1 °C even with a 10 s sensor data gap. Thus, the run-time model is useful in scenarios where sensor data collection frequency is smaller

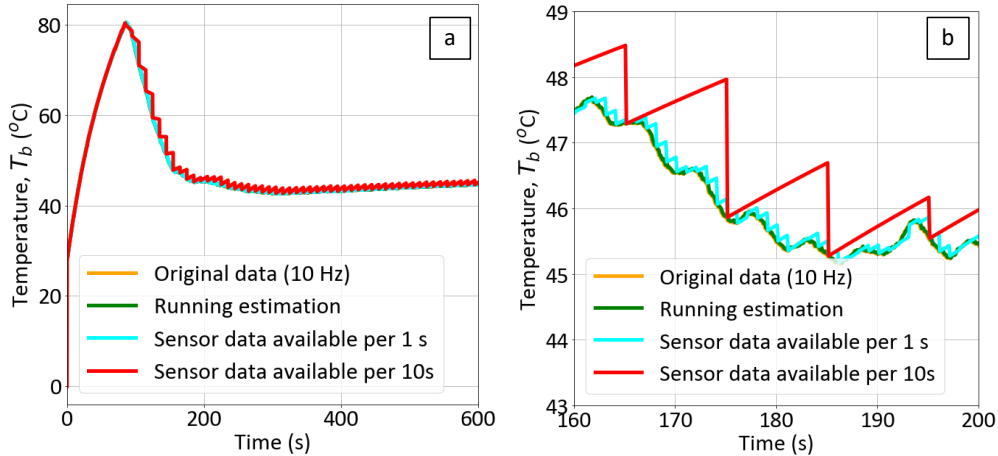


Figure 80: (a) Comparison of original temperature data with predicted temperature from fitted flash cooling expression. (b) Looking around time=180 s, the reduction in sensor data frequency may lead to incorrect cooling decisions below 1 Hz.

than the workload changes or flash cooling controls. However, the prediction could be improved to correctly predict the transient behavior with limited sensor information.

6.4. Improved heat sink and smaller ceramic heater

6.4.1. Improved heat sink with tube inserted

The TDU architecture (Configuration 0) includes a specific heat sink design restricted by availability of copper heat sinks with pin-fins. However, a modified prototype was created by pushing away pin-fins from the center of the heat sink to allow inlet tube to be about 4 mm from

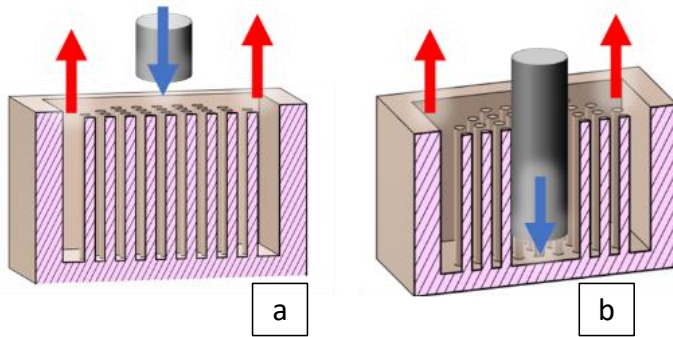


Figure 81: Representative CAD cut-sections for TDU. (a) Configuration 0 with fluid inlet at the top plate. (b) Configuration 1 with fluid inlet close to copper base.

the bottom of the heat sink (Configuration 1) (Fig. 81). The difference in results obtained from similar input parameters are shown in Table 16. The average temperatures have reduced due to higher effective heat transfer coefficients obtained during steady-periodic pulses, and thus new configuration is recommended for

exploration in future work.

Table 16: Reduction in operating temperature with configuration 1. The extension of inlet tube closer to base surface reduces bypass and enhances overall heat transfer for flash cooling.

Power, P (W)	Interval, t_p (s)	Volume, v_p (mL)	Average base temperature, $\langle T_b \rangle$ ($^{\circ}\text{C}$)		Steady-periodic averaged, effective heat transfer coefficient, $\langle h_{eff} \rangle$ ($\text{W}/\text{m}^2\text{K}$)	
			Configuration 0	Configuration 1	Configuration 0	Configuration 1
150	2	0.3	60	35	4000	12000
200	5	1	48	39	7000	12000
200	1	0.3	42	37	10000	13000

The following work in sections 6.4.2, and 6.4.3, has been designed and performed with Rishi Pugazhendhi, a Graduate Student Researcher at University of California, Los Angeles under Professor Timothy S. Fisher's guidance.

6.4.2. Smaller ceramic heater

The biggest limitation of the extensive testing with TDU prototype has been the unavailability of high heat flux heater for a large area of $\sim 1600 \text{ mm}^2$. An alternative path is to use a smaller heater while treating the heat sink as a flash chamber with heat spreading. This should allow testing at higher localized heat fluxes as well as pushing the total heat removal from the flash chamber.

The heater selected for this purpose is a specialty heater from Thermal Devices, Inc., Maryland, USA with part number CER-1-01-00001 [51]. It is a rectangular heater with dimensions $25 \times 15 \text{ mm}^2$ that can be heated up to 580 W of nominal power. This ceramic heater is made aluminum nitride and has an internal K-type thermocouple embedded that indicates the operating condition of the heater, with maximum operating range up to $400 \text{ }^\circ\text{C}$ for continuous operation. A CAD image of the heater is shown in Fig. 82. A resistance and power calculators are generated by

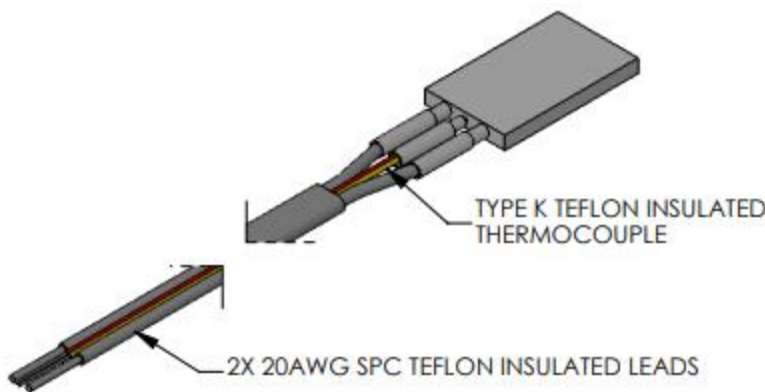


Figure 82: Watlow Ultramic 600 Advanced Ceramic Heater provided by Thermal Devices, Inc [51]. The heater dimensions are $25 \times 15 \text{ mm}^2$.

Rishi utilizing the thermal coefficient of resistance of $0.00150/^\circ\text{C}$ provided by the vendor.

The assembly of this heater with the configuration 1 of TDU described in previous section is performed with the help

of two base thermocouples on either side of the long edge of the heater, a side thermocouple (similar to extensive testing), Arctic MX-5 thermal interface material [52], and thick insulation pads to sustain high back temperature of the ceramic heater. The base temperature is analyzed by averaging the readings from both base thermocouples. The flash cooling tests were performed utilizing the flash cooling testbed (section 3.1) and utilizing similar test parameters as described in sections 5.3 and 6.3.

6.4.3. Preliminary results

The demonstration testing with the smaller ceramic heater is performed with four different combinations of power input to the heater, volume per pulse and pulse interval. The heat flux at the heater is varied from 0.2 W/mm^2 to 1 W/mm^2 which corresponds to 79 W to 372 W (Fig. 83). The heat input to the TDU is significantly higher than the 200 W heat input provided during the

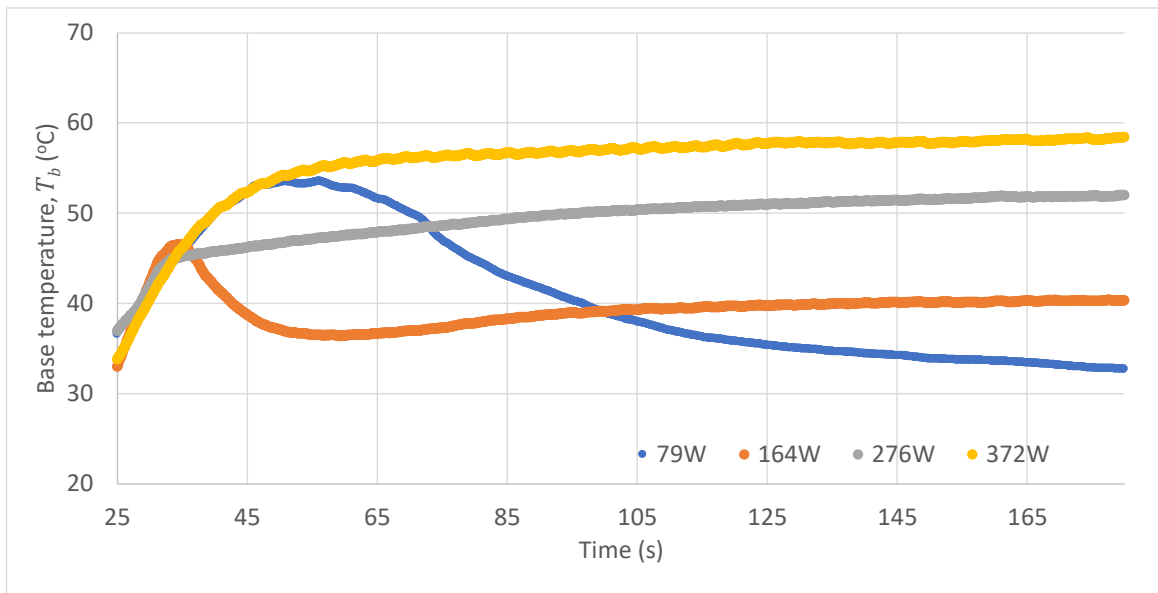


Figure 83: Averaged base temperature is recorded over time for four demonstration experiments performed with the smaller ceramic heater.

testing described in section 6.3. However, the demonstration testing was kept short due to the open loop operation of the methanol loop with high flow rates required at higher power levels. Due to

Table 17: Preliminary data for demonstration tests with the assembly of improved heat sink with smaller ceramic heater. The data is compared at 170-s test time is considered as an example.

Experiment (Data considered at 170s)	Power, P	Interval, t_p	Volume, v_p	Base temperature, T_b	Heat flux at heater, " q_{heater} "	Heater area / Heat sink base area, $\frac{A_{heater}}{A_{heat-sink}}$	Assuming perfect heat spreading over the heat sink area, $h_{eff.adjusted}$	Cumulative efficiency, η
	(W)	(s)	(mL)	(°C)	(W/mm ²)		(W/m ² K)	
1	79	5	0.65	33	0.21	0.24	6082	0.61
2	164	2	0.91	40	0.44	0.24	6757	0.36
3	276	2	0.82	52	0.74	0.24	6437	0.66
4	372	3	2.35	58	0.99	0.24	6941	0.46

the short nature of the experiments, they could not be categorized as steady-periodic and thus, the analysis is limited. However, the parameters are instead evaluated at 170-s test time for all four experiments. The heat transfer coefficient obtained for the heat sink is obtained by assuming perfect heat spreading in the copper base of the heat sink – thus, the entire base is at base temperature, T_b . This allows calculation of effective heat transfer coefficient from (63) and obtaining the G_{loss} from (60):

$$h_{eff,adjusted}(t) = \frac{A_{heater}}{A_{heat\ sink}} * \frac{q_{fc}(t)}{A_{heater} (T_b(t) - 25)} \quad (66)$$

Important to note is that due to difference in size of the heater from MINCO heater used in Chapter 4 and 5, and the heat sink area being 4 times the area of the smaller heater, adjusted heat flux and effective heat transfer coefficient are also evaluated. The adjustment assumes perfect heat spreading for the heat sink with the whole base at a single temperature represented by the average of two base thermocouples. The results of this analysis are included in table 17. It is seen that heat input of 372 W is cooled down to 58 °C base temperature, which represents significantly higher heat removal. The trend follows the inference from surrogate model results from section 6.3. These preliminary results provide more confidence in future work directions recommended in Chapter 8.

Chapter 7: Flash cooling in a vapor chamber

7.1. Flash vapor chamber (F-VC)

Vapor chambers are integral to modern high-performance electronic systems for both commercial and defense applications. However, a limitation of the vapor chamber is to handle large heat flux gradients. Several applications requiring high initial transient heat flux and a steady-state vapor chamber cooling later in [18]. The implementation of flash cooling for vapor chamber is different such that a large amount of liquid methanol is injected into the vapor chamber prior to application. When high initial transients are needed, an exit valve from the vapor chamber is opened to a low-pressure environment, thus forcing flash boiling at the interface of pressure gradient as discussed in Chapter 2. Since the steady-state operation of vapor chamber is thoroughly studied in literature, this work focused on understanding the thermal transients of initiating flash cooling within the vapor chamber. The prototype vapor chamber used is detailed in [24]. This prototype is called the flash vapor chamber (F-VC).

7.2. Extension of testbed and analysis tools for vapor chamber application

A modified flash cooling loop was used for evaluating flash vapor chamber as shown in Fig. 84 and described in detail in [18]. The testing conditions for this setup primarily focus on flash vapor chamber cooling for two different heat loading conditions. The first heat loading condition consists of a constant heat load (used to achieve steady-state initial conditions in the vapor chamber prior to flashing) that is maintained before and after flash initiation. These circumstances correspond to an initial low level of heating that is spread throughout the vapor chamber without increasing the fluid temperature beyond its boiling point, followed by a flash event that promotes rapid phase change. The second heat loading condition consists of a step-change in heat load

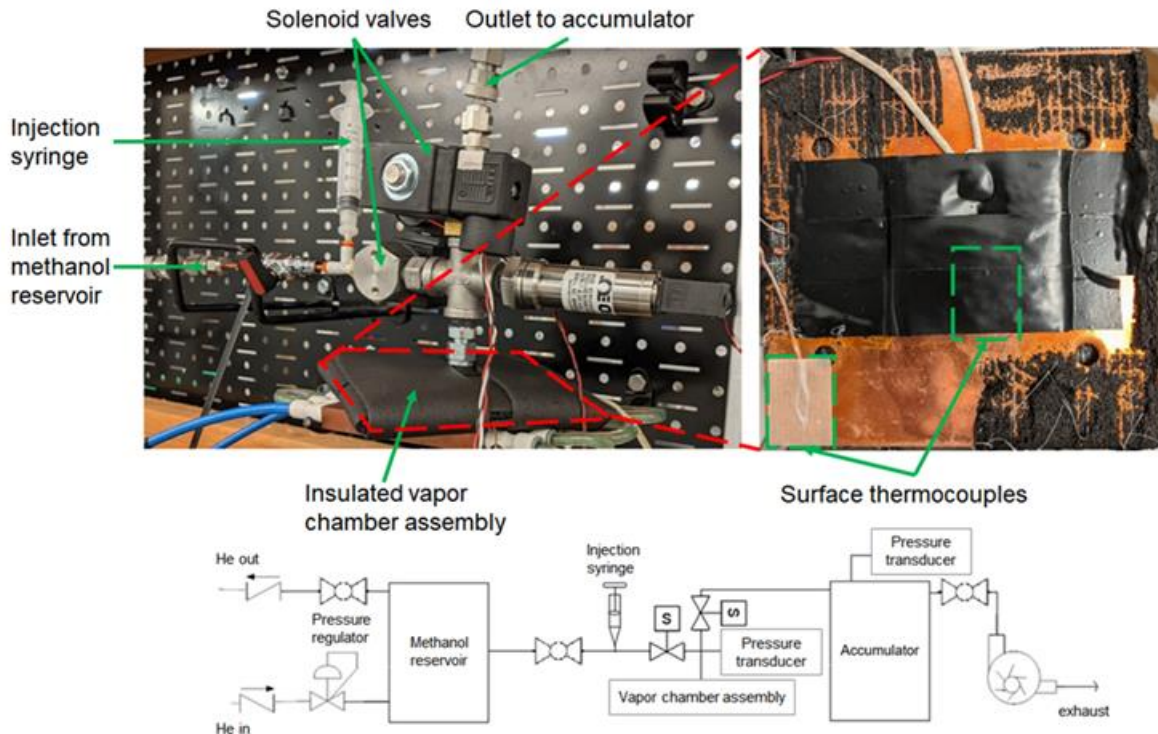


Figure 84: Experimental flash vapor chamber setup with corresponding P&ID. An injection syringe is added to the testbed for filling procedure of methanol [24].

applied simultaneously with flash initiation, hereafter denoted as a step heat load. For this case, flash initiation and change in heat load are applied after steady-state initial conditions in the vapor chamber are met. These circumstances correspond to impulsive, transient heat loads. To help quantify flash cooling rate, the temperature of the vapor chamber was averaged over two thermocouples: one placed on the top side of the vapor chamber near the discharge port, and one placed on the bottom side, towards the edge, as shown with the magnified inset view in Fig. 84. The initial equilibrium setting was achieved by ensuring a temperature drift of no more than 0.2 °C/min for a given heat load. Primary variables of interest include a. the amount of working fluid, expressed as a filling ratio, which is defined as the volume of liquid methanol divided by the volume of the internal volume of the vapor chamber, and b. initial temperature.

To conduct experiments, the chamber is first evacuated to soft vacuum with the help of the vacuum pump. Afterwards, a specific amount of methanol is introduced using the injection syringe as shown in Fig. 84. Brief perturbation on the exterior of the vapor chamber is necessary to minimize liquid deposition within the dead volume inside the tubing. Heat was then applied to the bottom of the vapor chamber to create elevated steady-state temperature conditions with minimal temperature drift. During the heating process, a ball valve connected to the open ambient is periodically controlled to maintain an internal pressure of 101 kPa. At steady state, the solenoid valve connected to the accumulator is opened, allowing flashing to begin.

7.2.1. Surrogate model

The lumped capacitance model introduced in section 4.2 is extended to incorporate the vapor chamber as a single lumped mass with considerations for a single pulse as opposed to a steady-periodic test. The radiation effects are ignored for this analysis. For F-VC prototype testing described in previous section, the simplified model is developed with these coefficients: $C_{th}=77.2$ J/K and $G_{loss}=0.2$ W/K. The parameters were found to have small dependence on test parameters so constant values were acceptable from curve fitting. Overall flash cooling model from (44) becomes:

$$q_{fc}(t) = P(t) - 77.2 * \left(\frac{dT_b(t)}{dt} \right) - 0.2 * (T_b - T_a) \quad (67)$$

The steady-periodic averaging from Chapter 3 is also extended for single pulse of F-VC. The theoretical maximum cooling, $E_{max,p}$, with any flash cooling pulse is calculated based on the mass of methanol used, m_p , and the difference in enthalpy, Δh . The starting enthalpy, h_i , is calculated based on initial reservoir or steady-state conditions. The outlet enthalpy, h_o , is calculated using

outlet pressure and average temperature of the lumped mass of the prototype. The enthalpy calculations were performed with a Jupyter notebook accessing the Coolprop database [37]:

$$E_{max,p} = m_p \Delta h \quad (68)$$

The enthalpy change is dominated by the methanol's latent heat of vaporization, but the enthalpy change computation also includes minor sensible heating contributions. The use of Coolprop enthalpy lookups simplifies the process of calculating the theoretical maximum cooling, incorporating both effects.

The total energy dissipated, E_p , by a single pulse is calculated by integrating the cooling rate over a specified time (60 s):

$$E_p = \int_{t_i=0}^{t_f=t} q_{fc}(t) dt ; t < 60 \text{ s} \quad (69)$$

In the case of the vapor chamber setup, h_i is a constant for each individual run and depends only on the initial steady-state temperature for each experimental trial and initial atmospheric pressure. Concurrently, the cumulative efficiency, η , of a flash pulse is calculated by comparing total cooling energy or power over a certain time interval, E_p , to the theoretical maximum:

$$\eta = \frac{E_p}{E_{max,p}} \quad (70)$$

7.3. Prototype results

The amount of methanol in the vapor chamber was varied from 2.0 mL to 3.5 mL while the heat input of 6.2 W remained constant for all tests. Averaged data over several identical experiments for the change in vapor chamber temperature is shown in Fig. 85a. Observation is that 3-5 s after depressurization, the rate of cooling is similar for all cases and independent of the amount of methanol. The exponential decay-like evolution of the change in temperature for the

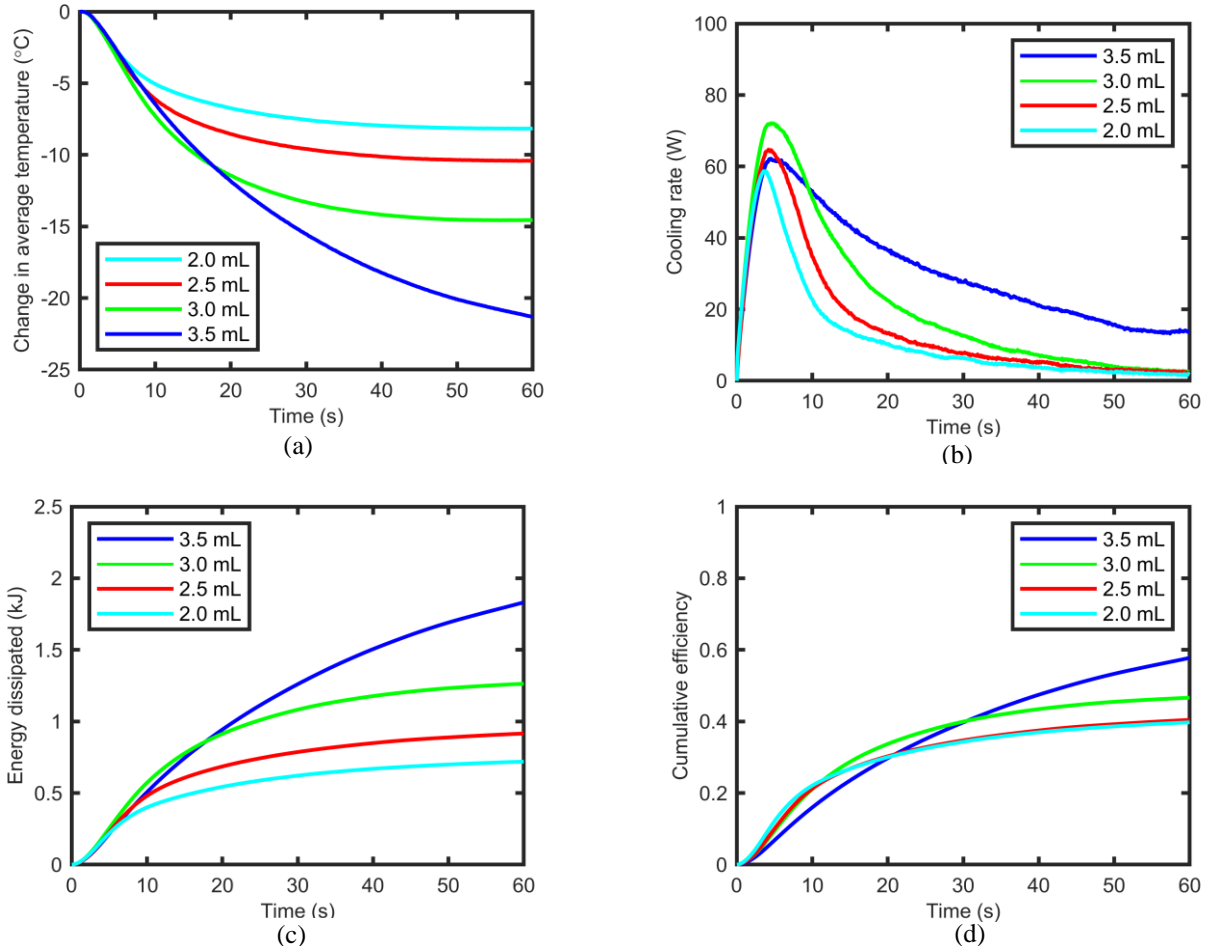


Figure 85: Flash vapor chamber results with different initial volume of methanol in the vapor chamber (a) Change in average vapor chamber temperature vs. time for different amounts of methanol under constant 6.2 W heat input. (b) Results for transient cooling rate of vapor chamber with a constant heat load (c) Cumulative energy dissipation of vapor chamber due to flash cooling. (d) Cumulative phase-change efficiency based on (61).

entire flash duration is also in agreement with prior work [7]. The internal methanol temperature was not directly measured; however, the methanol present in the vapor chamber after initial depressurization should have a lower temperature than the outside of the vapor chamber. As a result of the decrease in methanol temperature, the liquid superheat is reduced, subduing the flashing phenomenon.

Additionally, pressure increase due to vapor generation during flash increases local pressure which also tends to decrease the rate of vaporization. Local pressure inside the vapor

chamber is shown in Fig. 14, in which the change in sharp drop in pressure is due to rapid vaporization of methanol, and corresponding periods of initial pressurization due to vaporization are circled. The combined effect of decreased liquid temperature and increase in local pressure hinder the boiling process, causing a reduction of cooling flux with time after peak cooling is reached. Additionally, after 3 s, rate of temperature change is heavily influenced by methanol amount, as the transient cooling curves in Fig. 85a asymptote earlier for smaller amounts of methanol, signaling a shorter duration of cooling. The rapid, transient nature of flash cooling is illustrated in Fig. 85b, as the cooling rate, $q_{fc}(t)$, are calculated by using (67) and processed temperature data. The cooling rate peaks early after depressurization creating an initial peak. For cases of 2.0 mL, 2.5 mL, and 3.0 mL, the onset of peak cooling rate is directly proportional to methanol amount. Maximum cooling rates for 2.0 mL, 2.5 mL, and 3.0 mL are attained at 3.6 s, 4.3 s, and 4.8 s, respectively. After peak cooling, all cooling rates decay to zero, signaling the complete vaporization of all methanol initially present in the vapor chamber. We observe that for the case of 3.5 mL of methanol, the trend of both increase in cooling rate and onset of peak cooling with methanol amount is no longer followed, demonstrating adverse effects of excess thermal mass on cooling performance.

The total energy dissipated over time by a single pulse for different cases is shown in Fig. 85c. The cumulative efficiency over time was calculated by evaluating (69) at every time step (Fig. 85d). The curve for 3.5 mL falls below the others until 20 s, at which time additional methanol present in the vapor chamber allows for prolonged boiling and thus prolonged cooling at the expense of a decrease in peak cooling rate. The trend of increased energy dissipation with methanol amount is expected.

Additionally, for cases in which the initial temperature is varied under constant methanol volume, an increase in peak cooling rate with temperature is observed, shown in Fig. 86. These results support the notion that increased heat load helps induce more rapid phase-change, as heat must be absorbed for vaporization to occur. Also, an increase in initial temperature due to increased heat load

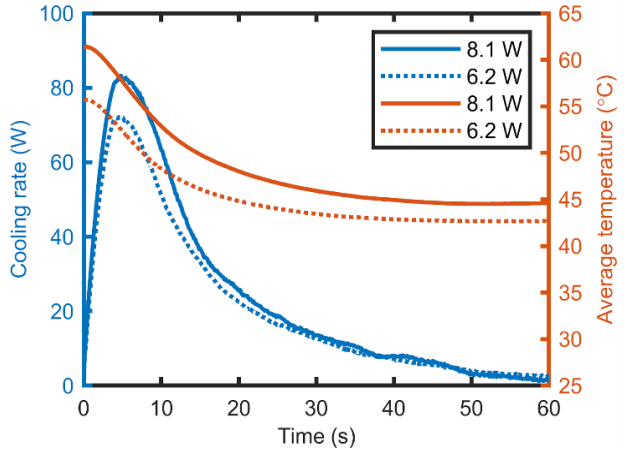


Figure 86: Results for transient cooling rate of the vapor chamber for various heat loads with constant working fluid volume of 3 mL.

corresponds to a larger superheat after depressurization. From the viewpoint of thermally controlled boiling theory, increases in superheat correspond to higher heat removal rates. In this regard, to maximize superheat, high initial temperatures and low accumulator pressures are desirable parameters when using flash to maximize peak transient cooling.

7.3.1. Comparison with TDU

A comparison between TDU and the flash vapor chamber is made by comparing average cooling provided by the flash chamber and the TDU. An example comparison is shown in Table 18. Both experiments show similar efficiency and average cooling for similar number of coolants. However, due to larger amount of initial methanol within the vapor chamber arrangement, much higher initial peak is observed than with steady-periodic pulses.

Table 18: Comparison of steady-periodic averages of TDU with flash vapor chamber observed at similar input parameters.

Prototype	Case (P, v_p, t_p)	Operating temperature (post 60s or $\langle T_b \rangle$) (°C)	Peak cooling rate (W)	Average cooling rate (over 60s) (W)	Cumulative efficiency, η
TDU	(22 W, 1 mL, 20s)	23	23	20	0.4
F-VC	(6 W, 3mL, 60s)	42	73	21	0.4

Chapter 8: Conclusions

The primary contribution of this work is the development of a thermal testbed for continuous, convective flash cooling and demonstration of adaptive capability of flash cooling. The experimental testbed presented in Chapter 3 is a dynamically controlled flow loop for flash cooling of high-heat-flux components. It has been designed to be flexible and robust to adapt to a variety of cooling architectures and devices required high-performance electronic systems. This work also includes the selection process of methanol as the optimal coolant for lab-scale testing, whereas refrigerants are recommended for large scale systems above 15kW. An extensive LabVIEW eco-system is developed with heating and flash cooling controls, run-time IR imaging of a device and recording transient data from thermocouples and pressure sensors. The testbed is connected to a large DC power supply and a dedicated chiller for steady-state operation up to 7.5 kW with 25 kW peak power. The importance of a thermal test vehicle for wafer-scale applications in order to simulate dynamic next generation workloads is highlighted. Due to limited availability of commercial heaters in this parameter space, several wafer-scale thermal test vehicles are optimally designed and fabricated.

The development of surrogate models from the transient thermal data generated from the testbed serves as a critical component in enabling flash cooling for electronics applications. The output data is analyzed with the help of several methods as described in Chapters 3, 4 and 5. The iterative understanding developed from these chapters in terms of steady-periodic and transient characteristics of flash cooling plays a key role in development of several surrogate models as described in Chapter 6. A combination of input power, volume of methanol per pulse and the interval between consecutive pulses is consistently used to understand the transient behavior. The steady-periodic averaging, and the resulting surrogate model, provide necessary information for

system-design of flash cooling with specific cooling architectures. For any system-design engineer, it is important to know the parameters to use for flash cooling for specified heat flu or total power and maximum operating temperature. An approximate transient model based on the dominant frequency of flash cooling is also developed to provide more information about the system such as the response time of the cooling architecture.

The transient surrogate models are developed for three purposes - understanding the transient dynamics for system-design, providing a simplified physical model that can assist with run-time anticipatory cooling, and approximating thermal envelope during operation between consecutive sensor inputs. The lumped capacitance analysis introduced in Chapter 4, and the verification with theoretical constraints of the analysis, establishes the foundation for transient models. Several example models are provided that serve as surrogates depending on available sensor and control data for particular system.

The surrogate models thus developed demonstrate the adaptability and dynamic control of flash cooling. The prototype developed to understand the thermal dissipation unit architecture, as discussed in Chapter 5, is used to perform a large set of experiments, and generate thermal data for these surrogate models. The sample models shown in Chapter 6 with this prototype are applicable for large range of input parameters and provide fairly accurate run-time. A sample anticipatory case is also shown to demonstrate the effect of anticipation in flash cooling. However, the surrogate models are limited to 200-W input power due to heater limitations. The steady-periodic model developed in section 6.3.2 shows the expected pulse-averaged cooling rate produced by given flow input parameters and current base temperature of the heat sink. This example model is able to estimate the cooling rate within 20% for all steady-periodic and over-cooled cases for 150- and 200-W input power.

The secondary objective of this work was to explore, design and test cooling architectures that utilize flash cooling efficiently for thermal management of Silicon Interconnect Fabric. Three cooling architectures are discussed in detail in Chapter 3, 4 and 5 – each of which are coherently designed with a larger system team, especially with power delivery experts. The first architecture is a tube and block structure (PowerTherm 1.0) that provides coolant through the tubes and delivers power through the blocks. The second architecture (PowerTherm 2.0) is a wafer-scale structure with pin-fins for power delivery and higher heat transfer coefficient. The third architecture (Thermal Dissipation Unit) is a segmented cooling chamber derived from the second architecture with significant improvement in thermal performance and provides controlled scale up for a large system as shown in Chapter 5. The prototypes for each architecture are fabricated and preliminary flash cooling tests are performed. This provides foundational data for system-design of flash cooling for prototyping of commercial applications and further research on specific applications.

The efficacy of flash cooling is also evaluated with different architectures by calculating the cumulative efficiency of cooling provided compared to the theoretical maximum heat transfer. The effective heat transfer coefficients were calculated for each architecture as per calculations described in section 5.2. The Thermal Dissipation Unit has following advantages over the other architectures:

- It provides highest efficiency cooling and highest heat transfer coefficient at similar heating and flow inputs.
- The response time, the delay from start of flash cooling to change in base temperature, is significantly reduced to 0.6 s (10X improvement from PowerTherm 1.0).

- Reduced temperature fluctuations as low as 0.1 °C in steady-periodic cooling compared to 3.6 °C for PowerTherm 1.0.
- Demonstrated higher efficiency and heat transfer coefficient at higher heat flux.

Another comparison is included between configuration 0 and configuration 1 of the TDU in section 5.4.1. The preliminary results indicate that configuration 1 demonstrates higher cooling rates by enabling insertion of flashing liquid closer to the base of the heat sink.

Chapter 7 introduces implementation and experimentation of flash cooling for a different architecture and different application – that requires high initial transients for vapor chamber applications. The analysis tools introduced for different architectures for Si-IF are also implemented for this single pulse application. A comparison of preliminary results with the TDU results in section 7.3 indicates the equivalent cooling efficacies obtained under similar conditions, however, the peak cooling rate produced is significantly for flash vapor chamber.

8.1. Future work

A vital limitation of this work is the constraint on the heat flux supplied by the available commercial heaters for the form factor of the prototypes. The thermal test vehicle (section 4.4) built with nichrome on a ceramic wafer would allow expansion of this work by demonstrating higher efficiency of flash cooling for higher heat fluxes. The ceramic wafer is designed to be used either as a whole for 80 x 80 mm² active area or cut into 4 individual heaters of 40 x 40 mm² each. For preliminary testing with single TDU, it is recommended to laser cut the heater and use individual heater. Additionally, a set of thin copper lugs are recommended in order to connect the wafer with high current power supply to minimize the stress on the wafer in the assembly. The soft nature of copper should also reduce effects of thermal expansion localized near the lug connection.

The alternative approach to demonstrate the efficacy of flash cooling at higher heat fluxes is to utilize a smaller ceramic heater as introduced in section 6.4. The smaller size of the heater, and corresponding lower power requirement for similar heat flux, allows easier fabrication. Several commercial heaters are available in the range of 20 mm size, out of which, a 25x15 mm² is chosen in section 6.4 and is recommended to continue further testing. The demonstration tests already show the capability to cool high heat flux from the smaller heater. However, this would require construction of smaller TDU prototypes to demonstrate the high heat transfer coefficients needed without heat spreading on Si-IF.

A direct improvement from the detailed set of experiments described in this work with the pin-fin flash chamber (labeled as “Configuration 0”) is to perform a similar set of experiments with improved design (labeled as “Configuration 1”). This flash chamber design is introduced in section 5.4.1 where the inlet tube is inserted close to the bottom of the heat sink. Preliminary results included in this study clearly indicate the advantage in increased effective heat transfer coefficient obtained from configuration 1 as compared to configuration 0.

The surrogate models developed in this work are limited to input power of 200 W which corresponds to up to 0.2 W/mm². Thus, critical next step with the high heat flux testing is to modify the surrogate models for broader range of heat fluxes. For steady-periodic model, a more complex model should be used compared. Inclusion of higher harmonics would improve the frequency-driven model. Even though a good correlation is seen with steady periodic averaging with only the considering the dominant frequency, it fails to predict the transient behavior of cooling rates limiting its functionality. Similarly, inclusion of side-wall temperature in the lumped capacitance model could improve transient response for the transient models. The transient model based on polynomial curve-fitting with lumped capacitance example is able to demonstrate the varying heat

transfer coefficient within individual pulses that is not captured with the steady-periodic averaging. However, the transient model used for run-time model along with finite difference discretization has limited information about the current pulse and thus creates a linear prediction. This linear prediction deviates when sensor information is not available frequently as demonstrated in section 6.3.3. with sensor frequency at 10 Hz. Two upgrades recommended involve either utilizing pulse information and adapt the model for each pulse (section 6.2.3) or utilizing data assimilation techniques instead of relying completely on the physical model for prediction (section 2.3.4). A sample test plan with application of Kalman filter to a surrogate model is also discussed in Chapter but could not be implemented in this work. The surrogate models developed in this work should provide a good foundation for these recommended models for future work and successful adoption of flash cooling for transient scenarios.

For understanding the transient behavior of flash cooling a piece of information in this work is the measurement of mean fluid temperature within the flash chamber at any time. The implementation of temperature measurement without intrusion to the flow behavior is a challenging task. The focus on system level implementation of flash cooling for Si-IF did not permit use of fluid temperature sensors. It is recommended to use at least two fluid thermocouples inserted with the help of through holes in the sidewall or the top plate. This information should provide more accurate calculations of heat transfer coefficient that correlate better with existing understanding of this metric. This approach will significantly enhance the quality of surrogate model developed; however, this parameter cannot be used for run-time prediction models as in-application implementation would lead to disruption of system-level cooling.

A combination of the three directions of future work discussed above – implementation of ceramic heater or small heater, validation of improved configuration 1 heat sink, and

improvements in surrogate models, can be performed by implementing the extension of TDU testing with the ceramic heater wafer and utilizing configuration 1 flash chamber. This approach enables the following:

- Estimation and validation of configuration 1 compared to configuration 0 at similar heat fluxes described in this work.
- Demonstration of the ceramic heater designed in this work.
- Development of surrogate model similar to this work for configuration 1 with expected higher cooling rate for similar flow conditions.
- Extension to higher heat flux cases with the ceramic heater.
- Followed by extension of surrogate models to higher heat fluxes. The large heat flux range may require more complex surrogate models compared to the polynomial-based models utilized in this work.

Thus, this combined approach is recommended to improve this work in multiple directions.

The surrogate models can be utilized to develop more fundamental understanding of flash cooling by modifying the models described in Chapter 6 by including fluid state variables as described in Chapter 2. However, the test setup would need to be modified from cooling an actual device to cooling a single tube imitating the device. The thermal testbed can be adapted to perform these experiments and thus, this creates another opportunity to expand this work and develop deeper understanding into the transient characteristics of flash cooling in alignment with primary objective of this work. However, this approach requires a deviation from the application of wafer-scale electronics cooling but rather focuses on fundamental understanding of flash cooling.

Appendix A: Utility code for processing transient data

Utility code for initial processing of transient experimental data

Developed by Ujash Shah [Fisher lab (MAE) + CHIPS lab (ECE) UCLA]

- Also has ability to compare the obtained profiles with lab notes for verification

Version: 1.4

Update date: August 28, 2021

Change log:

- Section 1: Basics: Data import (single file at a time), smoothing with SGDD, derivative array, pulse time calculations (Moved to section 2)
- Section 2: Slicing data, plotting and comparison with notes
- Section 3: Analysing steady-periodicity and calculating averages
- Section 4: Exporting processed data to respective output files

Section 1: Basics

1.1. Initialize

Include any tips/file-handling etc

1. All parameters are in SI units
2. Temperature calculations are performed with $^{\circ}C$ everywhere.

In []:

```
import numpy as np
from numpy import loadtxt
import matplotlib.pyplot as plt
from scipy.optimize import minimize
from scipy.optimize import curve_fit
from scipy.signal import savgol_filter
from mpl_toolkits import mplot3d
```

1.2. File import and smoothening

In []:

```
Filenumber=5
Power=100 #in W
Collection=0.01 #in seconds
vp=0.522 #mL/pulse
tp=10 #s
Condition=1 #0=UC,1=MUC,2=SP,3=MOC,4=OC

IN = loadtxt("raw/%s.txt" %Filenumber, delimiter="\t")
print(IN[:,1], "\n", np.size(IN,0), np.size(IN,1))
DATA=np.zeros((5+5, np.size(IN,1)))
print(np.size(DATA,0), np.size(DATA,1))
total_time=np.size(DATA,1)
print(total_time)
for i in range(10):
    if i<5:
        DATA[i,:] = savgol_filter(IN[i,:], 3, 2, mode='nearest')
    else:
        DATA[i,:] = 10*savgol_filter(IN[i-5,:], 3, 2, deriv=1, mode='nearest')
```

1.2.1. Plotting and verification

In []:

```
#Base temperature
plt.figure(figsize=(15,10))
#plt.xlabel('Time (s)')
plt.ylabel('Temperature ( $^{\circ}$ C)')
plt.plot(IN[3,:], 'r', label='Raw data')
plt.plot(DATA[3,:], 'k', label='Processed data')
plt.legend()

ax2=plt.twinx()
ax2.plot(DATA[8,:], 'blue', label='Derivative')
ax2.set_ylabel('Temperature/time ( $^{\circ}$ C/s)')
#plt.plot(DATA[8,:], 'b', label='Derivative')
plt.grid()
plt.legend(loc=7)
plt.rcParams["font.family"] = "Calibri"
plt.rcParams["font.size"] = "24"
```

In []:

```
#Outlet Pressure
plt.figure(figsize=(15,10))
plt.xlabel('Time (s)')
plt.ylabel('Absolute pressure (kPa)')
plt.plot(IN[1,:], 'r', Label='Raw data')
plt.plot(DATA[1,:], 'k', label='Processed data')
plt.legend()

ax2=plt.twinx()
#ax2.plot(DATA[6,:], 'bLue', Label='Derivative')
ax2.set_ylabel('Absolute pressure/time (kPa/s)')
plt.plot(DATA[6,:], 'b', label='Derivative')
plt.grid()
plt.legend(loc=7)
plt.rcParams["font.family"] = "Calibri"
plt.rcParams["font.size"] = "24"
plt.xlim(500,1000)
```

1.2.2. Exploration of pressure fluctuation for pulse time decision

In []:

```
#Outlet Pressure
plt.figure(figsize=(15,10))
plt.xlabel('Time (s)')
plt.ylabel('Absolute pressure/time (kPa/s)')
plt.plot(IN[1,:], 'r', Label='Raw data')
plt.plot(DATA[6,:], 'blue', label='Processed data')
plt.xlim(8150,8200)
plt.ylim(0,10)
plt.legend()
```

Section 2: Data slicing, plotting and comparison with notes

2.1. Data slicing into 4 zones

1. Heating only: array H
2. Heating + Flash cooling: array FC
3. Heating off - cooling only: array C

In []:

```
#1
Hstart=0

for i in range(np.size(DATA[8,:])):
    if DATA[8,i]>(Power/130):
        Hstart=i
        break
print(Hstart)
```

In []:

```
#2
FCstart=0

for i in range(np.size(DATA[6,:])):
    if DATA[6,i]>(10):
        FCstart=i-1
        break
print(FCstart)

H=DATA[:,Hstart:FCstart]
print(np.size(H,0),np.size(H,1))
```

In []:

```
#3
Hend=0

for i in range(np.size(DATA[8,:])):
    if DATA[8,i]<(-1):
        Hend=i
        break
if Hend==0:
    Hend=np.size(DATA[8,:])
    C=0
else:
    C=DATA[Hend,np.size(DATA[8,:])]

print(Hend)

FC=DATA[:,FCstart:Hend]
print(np.size(FC,0),np.size(FC,1))
#print(np.size(FC,1)+np.size(H,1)+np.size(C)+Hstart)
```

2.1.1. Pulse timing calculation

-- Uses data from FC array

In []:

```
start=(np.zeros((2000,1),dtype=int))
duration=np.zeros((2000,1))
startmax=0
for i in range(np.size(FC[6,:])):
    if FC[6,i]>=20 and (i-start[startmax-1])>50:
        start[startmax]=i
        duration[startmax]=0.1*(i-start[startmax-1])
        startmax=startmax+1

number_pulse=startmax-1
average_pulse=int(round(10*np.average(duration[1:number_pulse])))
print("Average pulse time is", "%.1f" %(average_pulse/10), "(seconds)")
print("Number of pulses is ", number_pulse)
```

Section 3: Steady-periodic conditions check, array and average calculations

Steady-periodic zone: array SP (special part of HFC) -Calculated after H and HFC Current conditions:

Pulse to pulse average changes less than 0.5 oC and 0.5 kPa

3.1. Calculation of averages based on pulse duration

In []:

```
average_Tb=np.zeros((number_pulse,1))
average_Ts=np.zeros((number_pulse,1))
average_To=np.zeros((number_pulse,1))
average_Po=np.zeros((number_pulse,1))
average_Tbv=np.zeros((number_pulse,1))

for i in range(number_pulse):
    start_pulse=int(start[i])
    end_pulse=int(start[i+1])
    average_Tb[i]=np.average(FC[3,start_pulse:end_pulse])
    average_Ts[i]=np.average(FC[2,start_pulse:end_pulse])
    average_To[i]=np.average(FC[4,start_pulse:end_pulse])
    average_Po[i]=np.average(FC[1,start_pulse:end_pulse])
    average_Tbv[i]=(np.max(FC[3,start_pulse:end_pulse])-np.min(FC[3,start_pulse:end_pulse]))

## Testing averages by plotting
plt.figure(figsize=(15,10))
plt.xlabel('Pulse number')
plt.ylabel('Average wihtin the pulse')
plt.plot(average_Tb,'blue',label='<math>\langle T_b \rangle</math>')
plt.plot(average_Ts,'k',label='<math>\langle T_s \rangle</math>')
plt.plot(average_To,'m',label='<math>\langle T_o \rangle</math>')
plt.plot(average_Po,'r',label='<math>\langle P_o \rangle</math>')
plt.plot(average_Tbv,'g',label='<math>\Delta T_{b,v}</math>')

#plt.xlim(3,5)
#plt.ylim(0,10)
plt.legend()
plt.grid()
```

3.2. Checking steady-periodic conditions

In []:

```
##SP checks
start_SP=0
end_SP=0
counter=0
countermax=0
reset=0

for i in range(1,number_pulse):
    if abs((average_Tb[i]-average_Tb[i-1]))<0.5:
        if abs((average_Ts[i]-average_Ts[i-1]))<0.5:
            if abs((average_To[i]-average_To[i-1]))<0.5:
                if abs((average_Po[i]-average_Po[i-1]))<0.5:
                    counter=counter+1
                    #print(average_Tb[i]-average_Tb[i-1],average_Ts[i]-average_Ts[i-
1])
                if counter>=countermax:
                    countermax=counter
                    start_SP=i-(counter-1)
                    end_SP=i
            else:
                #print("reset")
                counter=0
        #print(start_SP,end_SP,countermax)

if countermax>10 and ((countermax*average_pulse/10)>100):
    print("Steady periodic conditions exist between pulse number %d and %d for %d pulses"
%(start_SP,end_SP,countermax))
    start_SP_time=(FCstart)+(start[start_SP])
    end_SP_time=(FCstart)+(start[end_SP])
    print("Steady periodic conditions exist between time %.1f (seconds) and %.1f (seconds)for %d pulses"
%(start_SP_time/10,end_SP_time/10,countermax))
else:
    print("SP not achieved")
    start_SP_time=0
    end_SP_time=0
```


4.2. Processed data

In []:

```
processed=np.savetxt('processed/%d.txt' %Filenumber,DATA,delimiter='\t')
heating=np.savetxt('H/H%d.txt' %Filenumber,H,delimiter='\t')
cooling=np.savetxt('FC/FC%d.txt' %Filenumber,FC,delimiter='\t')

if countermax>10 and ((countermax*average_pulse/10)>100):
    steadyperiodic=np.savetxt('SP/SP%d.txt' %Filenumber,SP,delimiter='\t')
```

Appendix B: Parameter code and steady-periodic analysis

In [1]:

```
import numpy as np #Parameters for C0
from numpy import loadtxt
import matplotlib.pyplot as plt
from scipy.optimize import minimize
from scipy.optimize import curve_fit
from scipy.signal import savgol_filter
from mpl_toolkits import mplot3d
from mpl_toolkits.mplot3d.art3d import Poly3DCollection
from matplotlib import cm
import CoolProp.CoolProp as cp
from scipy import interpolate
from cycler import cycler
#from IPython.display import display
```

In [2]:

```
PARA=open('P/ALL.txt','w')
PARA.write('#\t P(W)\t t_col (s)\t v_p\t t_p\t State\t t_total\t t_HON\t t_FCON\t
          + 't_HOFF\t t_pc\t #_p\t t_SPON\t t_SPOFF\t #_pSP\t t_bSP\t T_sSP\t T_oSP\t
P_oSP\t t_pSP\t SP_Tbv\n')
for i in [3,4,5,6,7,8,9,12,13,14,15,17,20,21,22,23,24,25,26,27,28,31,32,33,34,35,36,3
7,38,39,40,41,42]:
    file=loadtxt('P/P%d.txt'%i,delimiter='\t')
    PARA.write('%d\t%d\t%.3f\t%.3f\t%.1f\t%.1f\t%.1f\t%.1f\t%.1f\t%.1f\t%.1f\t%.1f
\t%.
              + '1f\t%.1f\t%.1f\t%.1f\t%.1f\t%.1f\n'%tuple(file))
PARA.close()
```

In [3]:

```
ALL=loadtxt('P/ALL.txt',delimiter='\t')
#print(ALL[0,:])
print(np.size(ALL,0),np.size(ALL,1))
```

33 21

In []:

```
plt.figure(figsize=(15,10))
plt.xlabel('Collection time (s)')
plt.ylabel('Average measured volume (mL/pulse)')
plt.plot(ALL[:,2],ALL[:,3], 'xr', label='Measurements', linestyle='none')
plt.rcParams["font.family"] = "Calibri"
plt.rcParams["font.size"] = "28"
plt.grid()
plt.legend(loc=7)
t='Methanol'
```

In []:

```
plt.figure(figsize=(10,10))
plt.xlabel('Specified pulse interval(s)')
plt.ylabel('Average measured pulse interval (corrected) (s)')
#plt.plot(ALL[:,4],ALL[:,10], 'xr', Label='Measurements', linestyle='none')
plt.scatter(ALL[:,4],ALL[:,10],c='blue',s=1000)
plt.rcParams["font.family"] = "Calibri"
plt.rcParams["font.size"] = "28"
plt.grid()
plt.figure(figsize=(10,10))
plt.xlabel('Power(W)')
plt.ylabel('Condition marker')
plt.legend(loc=7)
#print(ALL[:,10])
```

In []:

```
SIZE=np.size(ALL,0)
Qf=np.zeros((SIZE,1))
Density=np.zeros((5,2))
Density[:,0]=[44,100,150,200,300]
color=['r', 'orange', 'green', 'cyan', 'darkblue']
for i in range(5):
    for j in range(SIZE):
        if ALL[j,1]==Density[i,0]:
            Density[i,1]=Density[i,1]+1
print(Density)
Density=0.5*Density
col=[]
for i in range(SIZE):
    col.append(color[int(ALL[i,5])])
    Qf[i]=ALL[i,3]/ALL[i,10]

#print(Qf)
plt.figure(figsize=(10,10))
plt.xlabel('Power(W)')
plt.ylabel('State')
plt.scatter(ALL[:,1],ALL[:,5],s=40*Density,c=col)
plt.xlim(30,320)
plt.ylim(4.5,-0.5)
#plt.legend()
plt.rcParams["font.family"] = "Calibri"
plt.rcParams["font.size"] = "48"
plt.rcParams["axes.prop_cycle"]=cycler('color',['r', 'orange', 'green', 'cyan', 'darkblue'])
#plt.grid()
#plt.legend(loc=2,fontsize='small')
```

In []:

```
plt.rcParams["font.family"] = "Calibri"
plt.rcParams["font.size"] = "36"
plt.figure(figsize=(15,15))
X,Y,Z=(ALL[:,10],ALL[:,3],ALL[:,1])
ax = plt.axes(projection='3d')

ax.scatter(X, Y, Z, c=col,s=1000)
#ax.plot_surface(X, Y, Z) #rstride=1, cstride=1,cmap='viridis', edgecolor='none')
ax.set_title('State marker');
ax.set_ylabel('Volume (mL/pulse)',labelpad=20) #Corrected
ax.set_xlabel('Pulse interval (s)',labelpad=20) #Corrected
ax.set_zlabel('Power (W)',labelpad=20)
major_ticks = [50,100,150,200,250,300]
ax.set_zticks(major_ticks)
major_ticks = np.arange(0.1,1.2,0.2)
ax.set_yticks(major_ticks)
major_ticks = np.arange(0,10,1)
ax.set_xticks(major_ticks)
plt.xlim(10,1)
plt.ylim(0,1.2)
#ax.set_zlim(80,120)
ax.view_init(30,30)
#ax.view_init(azim=0, elev=90)
```

In []:

```
plt.rcParams["font.family"] = "Calibri"
plt.rcParams["font.size"] = "48"
#plt.figure(figsize=(15,15))
plt.figure(figsize=(10,10))
plt.scatter(Y/X,Z,c=col,s=1000)
plt.xlabel('Flow rate (mL/s)')
plt.ylabel('Power (W)')
plt.grid()
```

In []:

```
t='Methanol'
print("Case\tP(W)\tt_p(s)\tv_p(mL)\tQ(mL/s)\tT_bSP\tP_oSP\tState\tT_oSP\t\Delta T_b")
for i in range(np.size(ALL,0)):
    if ALL[i,1]==150:# or ALL[i,5]==3:# and ALL[i,1]==150: # or ALL[i,1]==200 or ALL
[i,1]==300:
        #Tsat=(cp.PropsSI('T','P',ALL[i,18]*1000,'Q',1,t)-273.15)
        #ho=(cp.PropsSI('H','P',ALL[i,18]*1000,'T',ALL[i,15]+273.15,t))
        print("%d\t%d\t%.1f\t%.2f\t%.3f\t%.1f\t%.1f\t%d\t%.1f\t%.1f\t\n"
              %(ALL[i,0],ALL[i,1],ALL[i,10],ALL[i,3],ALL[i,3]
                /ALL[i,10],ALL[i,15],ALL[i,18],ALL[i,5],ALL[i,17],ALL[i,20]))
        #t%.1f
```

In []:

```
ALLC=(ALL[:,5]>=2)
ALLD=ALL[ALLC,:]
plt.rcParams["font.family"] = "Calibri"
plt.rcParams["font.size"] = "32"
#plt.figure(figsize=(15,15))
plt.figure(figsize=(10,10))
col=[]
for i in range(np.size(ALLD,0)):
    col.append(color[int(ALLD[i,5])])
temp=ALLD[:,3]/ALLD[:,10]
plt.scatter(ALLD[:,1],ALLD[:,15],c=col,s=1000)
plt.xlabel('Power,$P$ (W)')
plt.ylabel('Average base temperature, $<T_b>$ ($^oC$)')
plt.grid()
```

In []:

```
ALLC=(ALL[:,5]>=2)
ALLD=ALL[ALLC,:]
plt.figure(figsize=(10,10))
col=[]
for i in range(np.size(ALLD,0)):
    col.append(color[int(ALLD[i,5])])
temp=ALLD[:,3]/ALLD[:,10]
plt.scatter(ALLD[:,1],ALLD[:,15],c=col,s=1000)
plt.xlabel('Power,$P$ (W)')
plt.ylabel('Average base temperature, $<T_b>$ ($^oC$)')
plt.grid()
```

In []:

```
ALLC=(ALL[:,5]>=2)
ALLD=ALL[ALLC,:]
plt.figure(figsize=(10,10))
col=[]
for i in range(np.size(ALLD,0)):
    col.append(color[int(ALLD[i,5])])
temp=ALLD[:,3]/ALLD[:,10]
plt.scatter(ALLD[:,0],2*ALLD[:,20],c=col,s=1000,alpha=1)
plt.xlabel('File number')
plt.ylabel('Variation in base temperature, $<\Delta T_b>$ ($^oC$)')
plt.ylim(0,2)
plt.grid()
```


In []:

```
ALLC=(ALL[:,5]>=2)
ALLD=ALL[ALLC,:]

Ti=25 # in C
Pi=1.01325e5 # in Pa
hi=cp.PropsSI('H','T',273.15+Ti,'P',Pi,t) #J/kg
di=cp.PropsSI('D','T',273.15+Ti,'P',Pi,t) #kg/m3
di=di*1e-6 #kg/mL
print(di)
t='Methanol'
def HLOSS(x):
    return((-7.7e-8*x*x*x)+(3e-5*x*x)+(-3.1e-3*x)+0.5)*(x-25)
def DH(x,xx): #x= Tb, y = vp, z= tp, xx=Po
    homax=cp.PropsSI('H','T',273.15+x,'P',xx,t) #J/kg
    return(homax-hi)

qfc=np.zeros((np.size(ALLD,0),1))
qmax=np.zeros((np.size(ALLD,0),1))
eta=np.zeros((np.size(ALLD,0),1))

qfc=(ALLD[:,1])-(HLOSS(ALLD[:,15]))

for i in range((np.size(ALLD,0))):
    Tx=ALLD[i,15]
    Qp=ALLD[i,3]/ALLD[i,4] #mL/s
    mp=di*Qp #kg/s
    qmax[i]=1.5*mp*DH(Tx,ALLD[i,18]*1000)
    eta[i]=qfc[i]/qmax[i]
    print(ALLD[i,15],HLOSS(ALLD[i,15]),qfc[i],qmax[i],eta[i])
```

In []:

```
#plt.figure(figsize=(10,10))
plt.rcParams["font.family"] = "Calibri"
plt.rcParams["font.size"] = "32"
#plt.figure(figsize=(15,15))
plt.figure(figsize=(10,10))
col=[]
for i in range(np.size(ALLD,0)):
    col.append(color[int(ALLD[i,5])])
#temp=ALLD[:,3]/ALLD[:,10]
plt.scatter(ALLD[:,0],eta,c=col,s=1000,alpha=1)
plt.xlabel('File number')
plt.ylabel('Cumulative efficiency,  $\eta$ ')
plt.ylim(0,1)
plt.grid()
```

In []:

```
# X1 = Tb, X2=vp,X3=tp, R=q
#ALLC=(ALL[:,5]>=2)
#ALLD=ALL[ALLC,:]
X1=ALLD[:,15]
X2=ALLD[:,3]
X3=ALLD[:,10]
R=qfc[:]
print(X1,X2,X3,R)
```

In []:

```
def fit(x,a,b,c):
    return(((a+(b*(x[0]-25)))*x[1]/x[2])+c)

Y=R
#print(X,Y)
popt, pcov = curve_fit(fit,[X1,X2,X3],Y,method='lm')#,absolute_sigma=True) #Least square (lm) method
print(popt) #,pcov)
residuals = Y- fit([X1,X2,X3], *popt)
ss_res = np.sum(residuals**2)
ss_tot = np.sum((Y-np.mean(Y))**2)
r_squared = 1 - (ss_res / ss_tot)
print("\nR^2 value is %f" %r_squared)
plt.plot(residuals)
```

Appendix C: Transient estimation code

1. Problem description and formulation

1.1. Description

The flash chamber prototype is considered a lumped capacitance (verification to follow later). This code focuses on estimating the losses from this lumped capacitance at any operating temperature. Range of temperatures considered: $25^{\circ}C$ to $150^{\circ}C$

1.2. Energy balance

The calculations are performed from separate experiments performed in the absence of flash cooling (but under vacuum conditions similar to flash cooling experiments). The sample is heated at incremental powers until two steady state criterion are satisfied.

$$P = G_{loss}(T_b - T_{\infty}); T_{\infty} = 25^{\circ}C$$

Criteria 1 (Short range): $0.4^{\circ}C/min$ Criteria 2 (Long range): $1^{\circ}C/(5min)$

Compare with:

1. Critical dT/dt from scaling analysis: $0.2^{\circ}C/min$
2. Sensor fluctuations: $0.2^{\circ}C/s$

1.3. Data file format

- Import (I,T_{SS}) Total 36 experiments were performed. Starting with 1W/step and ramping to 2W/step while maintaining average 1 data point/ $5^{\circ}C$

1.4. Fitting parameters

The assumed form of G_{loss} is a order-3 polynomial to incorporate all losses including radiation effects.

$$G_{loss} = ax^3 + bx^2 + cx + d$$

1.5. Sample calculation with estimated curve from 2.4 later

In []:

```
Tb=31
Gloss=(-6.70e-7*(Tb**3))+(2.04e-4*(Tb**2))+(-1.92e-2*Tb)+9.67e-1
P=Gloss*(Tb-25)
print(Tb,Gloss,P)
```

2. File import, calculations and publish

2.1. File import

In []:

```
IN = loadtxt("IvsT.txt", delimiter="\t")
#print(IN[30,1])
```

2.2. Calculations

Assuming $R_{heater} = 2.1\Omega$, $P = I^2R$ DATA file format = $[I, T, P, G_{loss}]$

In []:

```
GDATA=np.zeros((np.size(IN,0),2+2))
GDATA[:,0]=IN[:,0]
GDATA[:,1]=IN[:,2]

for i in range(0,np.size(IN,0)):
    GDATA[i,2]=IN[i,0]*IN[i,0]*2.1
    GDATA[i,3]=GDATA[i,2]/(GDATA[i,1]-25)
print(np.size(GDATA),GDATA)
```

2.3. Curve fitting for G_{loss}

In []:

```
def fit(x,a,b,c,d):
    return((a*(x**3))+(b*(x**2))+(c*x)+d)

X=GDATA[6:,1]
Y=GDATA[6:,3]
#print(X,Y)
popt, pcov = curve_fit(fit, X,Y,method='lm')#,absolute_sigma=True) #Least square (l
m) method
print(popt) #,pcov)
residuals = Y- fit(X, *popt)
ss_res = np.sum(residuals**2)
ss_tot = np.sum((Y-np.mean(Y))**2)
r_squared = 1 - (ss_res / ss_tot)
print("\nR^2 value is %f" %r_squared)
plt.plot(residuals)
```

2.4. Final curve to use for other codes

In []:

```
print("$G_{loss}= %.2e (T_b)^3+ %.2e *(T_b)^2+ %.2e *(T_b)+ %.2e$" %tuple(popt))
```

In []:

```
X1=np.linspace(30,100,100)
Y1=np.linspace(30,100,100)
Z1=np.linspace(35,100,100)
for i in range(len(Y1)):
    Y1[i]=(-7.71e-8*(X1[i]**3)+(3.05e-5*(X1[i]**2))+(-3.12e-3*X1[i])+5.99e-1)
    Z1[i]=Y1[i]*(X1[i]-25)
plt.plot(X1,Y1)
plt.xlabel('Base temperature, $T_b$ ($^oC$)')
plt.ylabel('$G_{loss}$ (W/K)')
plt.xlim(37.8,38)
plt.ylim(0.52,0.525)
```

In []:

```
plt.plot(X1,Z1)
plt.xlabel('Base temperature, $T_b$ ($^oC$)')
plt.ylabel('Heat loss (W/K)')
plt.xlim(37.8,38)
plt.ylim(5,9)
```

3. Estimation for Cth

In []:

```
DATA=loadtxt('P/ALL.txt',delimiter='\t')
HDATA=np.zeros((27,np.size(DATA,1)))
#print(DATA)

j=0;
for i in [3,4,5,6,7,8,9,12,13,14,15,17,20,21,22,23,24,25,26,27,28,31,32,33,34,35,36]:
    for k in range(np.size(DATA,0)):
        if DATA[k,0]==i:
            HDATA[k,:]=DATA[k,:]
#j=13
#for i in [3,4,5,6,7,8,9,12,13,14,15,17,20,21,22,23,24,25,26,27,28,31,32,33,34,35,36,37,38,39,40,42]:
    file=loadtxt('H/H%d.txt'%i,delimiter='\t')
    r2=file[3,:]
    r3=file[8,:]
    size=np.size(r2,0)
    #print(size)
    r1=HDATA[j,1]*np.ones((size,1))
    if j==0:
        R1=r1 #P
        R2=r2 #Tb
        R3=r3 #DTb
    else:
        R1=np.append(R1,r1)
        R2=np.append(R2,r2)
        R3=np.append(R3,r3)
    j=j+1
#print(np.size(R1),R2,R3)
R1=np.transpose(R1)
R2=np.transpose(R2)
R3=np.transpose(R3)
#print(R1[0])
#R1=np.array(R1,dtype='float64')
plt.figure(figsize=(15,15))
#print(HDATA)
plt.plot(R3)
```

In []:

```
# Cth = (p-(Gloss*(Tb-25)))/DTb
R4=np.zeros((np.size(R1,0),1))
print(np.shape(R4))

R4=(R1-((-7.7e-8*(R2**3))+3.0e-5*(R2**2))+(-3.1e-3*(R2))+0.5)*(R2-25))/R3
#R4=(R1-(0.43)*(R2-25))/R3
plt.ylim(0,1000)
#R4=np.transpose(R4)
np.shape(R4)
R4.dtype
#plt.plot(R4)
#np.size(R1)
RP=R3>0
#RP=R2>60
R1P=R1[RP]
R2P=R2[RP]
R4P=R4[RP]

plt.plot(R4P)

RF=R4P<400
R1F=R1P[RF]
R2F=R2P[RF]
R4F=R4P[RF]

RR=R4F>40
R1R=R1F[RR]
R2R=R2F[RR]
R4R=R4F[RR]
plt.plot(R4R)
```

In []:

```
def fit(x,a,b,c,d):
    #return(a)
    return((a*x[0])+(b*(x[1]))+(c*x[0]*x[1])+d)

Y=R4R
#print(X,Y)
popt, pcov = curve_fit(fit,[R1R,R2R],Y,method='lm')#,absolute_sigma=True) #Least square (Lm) method
print(popt) #,pcov)
residuals = Y- fit([R1R,R2R], *popt)
ss_res = np.sum(residuals**2)
ss_tot = np.sum((Y-np.mean(Y))**2)
r_squared = 1 - (ss_res / ss_tot)
print("\nR^2 value is %f" %r_squared)
plt.plot(residuals)
```

In []:

```
cf=(0.14*R1R)+(5.21*(R2R))+(-0.01*R1R*R2R)+21
#print(cf)
plt.scatter(R2R,cf,alpha=0.7)
plt.scatter(R2R,R4R,alpha=0.05)
```

In []:

```
X1=np.linspace(100,100,1)
Y1=np.linspace(37.8,38,2)
X1, Y1 = np.meshgrid(X1, Y1)
Z1=(0.14*X1)+(5.21*(Y1))-(0.01*X1*Y1)+21

plt.rcParams["font.family"] = "Calibri"
plt.rcParams["font.size"] = "24"
plt.figure(figsize=(15,15))
ax = plt.axes(projection='3d')
surf = ax.plot_surface(X1, Y1, Z1, cmap=cm.coolwarm,linewidth=0, antialiased=False)

ax.set_ylabel('Base temperature, $T_b$ ($^{\circ}$C)',labelpad=15) #Corrected
ax.set_xlabel('Power, $P$ (W)',labelpad=15) #Corrected
ax.set_zlabel('$C_{th}$= <math>C_p</math> (P,T_b) $ (W/K)',labelpad=15)

plt.show()
```


4. Estimation for q_{fc}

In []:

```
FCDATA=np.zeros((28,np.size(DATA,1)))

j=0;
for i in [3,4,5,6,7,8,9,12,13,14,15,17,20,21,22,23,24,25,26,27,28,31,32,33,34,35,36,37]:
    for k in range(np.size(DATA,0)):
        if DATA[k,0]==i:
            FCDATA[k,:]=DATA[k,:]

    file=loadtxt('FC/FC%d.txt'%i,delimiter='\t')
    r2=file[3,:]
    r3=file[8,:]
    r8=file[0,:]
    size=np.size(r2,0)
    r1=FCDATA[j,1]*np.ones((size,1))
    r6=FCDATA[j,3]*np.ones((size,1))
    r7=FCDATA[j,10]*np.ones((size,1))
    r5=np.zeros((size,1))
    for k in range(1,size):
        r5[k]=r5[k-1]+0.1
    if j==0:
        R1=r1 #P
        R2=r2 #Tb
        R3=r3 #DTb
        R5=r5 #t
        R6=r6 #vp
        R7=r7 #tp
        R8=r8 #Po
    else:
        R1=np.append(R1,r1)
        R2=np.append(R2,r2)
        R3=np.append(R3,r3)
        R5=np.append(R5,r5)
        R6=np.append(R6,r6)
        R7=np.append(R7,r7)
        R8=np.append(R8,r8)
    j=j+1
print(j)
R1=np.transpose(R1)
R2=np.transpose(R2)
R3=np.transpose(R3)
R5=np.transpose(R5)
R6=np.transpose(R6)
R7=np.transpose(R7)
R8=np.transpose(R8)
plt.plot(R3)
```

In []:

```
def CTH(x,y):
    return((0.15*x)+(5.74*y)+(-0.01*x*y)+6.0)
def HLOSS(x):
    return((-7.7e-7*x*x*x)+(3e-5*x*x)+(-3.1e-3*x)+0.5)*(x-25)

R4=np.zeros((np.size(R1,0),1))
print(np.shape(R4))
R4=R1-(CTH(R1,R2)*R3)-HLOSS(R2)
np.shape(R4)
RP=(abs(R3)>0)

R1P=R1[RP]
R2P=R2[RP]
R3P=R3[RP]
R4P=R4[RP]
R5P=R5[RP]
R6P=R6[RP]
R7P=R7[RP]
R8P=R8[RP]

RF=R4P>0
R1F=R1P[RF]
R2F=R2P[RF]
R3F=R3P[RF]
R4F=R4P[RF]
R5F=R5P[RF]
R6F=R6P[RF]
R7F=R7P[RF]
R8F=R8P[RF]

RR=R4F<400
R1R=R1F[RR]
R2R=R2F[RR]
R3R=R3F[RR]
R4R=R4F[RR]
R5R=R5F[RR]
R6R=R6F[RR]
R7R=R7F[RR]
R8R=R8F[RR]
R8R=R8R*1000
plt.plot(R4R)
```

In []:

```
R10R=R4R/(R2R-25) #hfc
```

In []:

```
def fit(x,a,b,c,d,e,f,g,h,i,j,k,l):
    return((c*x[1]+d)*(x[1]-e*x[2]+f)*((g*x[3]/x[4])+h))

Y=R4R
#print(X,Y)
popt, pcov = curve_fit(fit,[R1R,R2R,R8R,R6R,R7R],Y,method='lm')#,absolute_sigma='True') #Least square (lm) method
print(popt) #,pcov)
residuals = Y- fit([R1R,R2R,R8R,R6R,R7R], *popt)
ss_res = np.sum(residuals**2)
ss_tot = np.sum((Y-np.mean(Y))**2)
r_squared = 1 - (ss_res / ss_tot)
print("\nR^2 value is %f" %r_squared)
plt.plot(residuals)
```

Appendix D: Dominant frequency-driven analysis

Dominant frequency analysis

Developed by Ujash Shah (UCLA)

Version: 1.3

Update date: August 9, 2021

Change log:

- Section 1: Problem definition
- Steady-periodic equation with one dominant frequency
- Section 2: Sample calculations and parameter evolution
 - v1.1
- Plot T vs t (Identified error in q_{fc} assumption
 - v1.2
- Update q_{fc} assumption and adapt the solution ($q_{fc} = F(1 + \cos(\omega t))$)
 - v1.3
- Verified the equations
- Generated equation suitable for Curve-fitting / optimization algorithms

Initialization of the code

Include any tips/file-handling etc

1. All parameters are in SI units

In []:

```
import numpy as np
import math as math
import matplotlib.pyplot as plt
from scipy.optimize import minimize
from scipy.optimize import curve_fit
from scipy.signal import savgol_filter
from mpl_toolkits import mplot3d
```

1. Problem description and formulation

1.1. Description

The flash chamber prototype is considered a lumped capacitance (verification to follow later). The analysis focuses on steady-periodic conditions obtained with transient flash cooling - with a constant heat input and pulsed flash cooling. The design of flash chamber is shown in Figure 1. We assume that all the heat dissipating from the heater goes in to the flash chamber as the heater is well insulated on the back side. The analysis also assumes that properties do not change with temperature.

1.2. Energy balance

Overall energy balance on the lumped flash chamber:

$$\dot{E}_{in} + \dot{E}_g = \dot{E}_{st} + \dot{E}_{out}$$

- Since, no heat generation occurs within the flash chamber,

$$\dot{E}_g = 0$$

- The storage term for a lumped mass can be expressed as

$$\dot{E}_{st} = MC \frac{dT(t)}{dt}$$

where mC is overall capacitance of the flash chamber

- The heating power, P , enters the flash chamber from the heater underneath and so we can write

$$\dot{E}_{in} = P(t)$$

- Similarly, heat is lost in the form of natural convection, q_{nc} , and radiation, q_{rad} , from the surface area, A .
- Since, the surface is insulated and the surface temperature of the insulation are small, the radiation term can be combined with the natural convection (as a standard practice). The combined heat loss can then be expressed with the help of a common heat transfer coefficient, h . We also assume that surrounding temperature, T_s , is the same as ambient temperature, T_a .
- The flash cooling is considered as q_{fc} . Even though traditionally, convective cooling is expressed in terms of coefficient and bulk temperature, flash process is highly transient with varying bulk temperature and thus, we take a different approach.
- Combining the heat flow out from natural convection, radiation, and flash cooling, we can write:

$$\dot{E}_{out} = q_{nc} + q_{rad} + q_{fc} = hA(T(t) - T_a) + q_{fc}(t)$$

Thus, the equation can be written as:

$$P(t) = MC \frac{dT(t)}{dt} + hA(T(t) - T_a) + q_{fc}(t)$$

1.3. ODE formulation

The equation can now be simplified with the use of $\Theta = T - T_a$ and dropping (t) as it is the only variable the equation depends on. Then, equation is

$$P = MC \frac{d\Theta}{dt} + hA\Theta + q_{fc}$$

1.3.1. Assumed cooling profile

We assume for simplicity and as a starting point that flash cooling can be described by $q_{fc} = F(1 + \cos(\omega t))$ where F is a constant.

Then the equation becomes (with some re-arranging),

$$MC \frac{d\Theta}{dt} + hA\Theta = P - (F(1 + \cos(\omega t)))$$

Since we assumed properties are constant, we can simplify the equation by assuming $m = hA/MC$, $n = -F/MC$ and $p = (P - F)/MC$. Then the equation becomes:

$$\frac{d\Theta}{dt} + m\Theta = p + n\cos(\omega t)$$

1.3.2. Nonhomogeneous equations

We will be assuming that the steady-periodic equation obtained from above expression has a general solution and a particular solution. Thus, $\Theta = \theta(t) + \theta_p$. So, General equation:

$$\frac{d\theta}{dt} + m\theta = n\cos(\omega t)$$

Particular equation:

$$\frac{d\theta_p}{dt} + m\theta_p = p$$

1.3.3. Particular solution

Since, particular solution is independent of time, we know that $\theta_p = \text{constant}$. Plugging it in the equation, we get

$$m\theta_p = p$$

Thus,

$$\theta_p = \frac{P - F}{mMC} = \frac{P - F}{hA}$$

1.4. General solution using exp(iwt)

We know that $\cos(\omega t) = \frac{e^{i\omega t} + e^{-i\omega t}}{2}$ and we assume that solution θ is a superposition of two solutions:

$$\theta = \theta_1(t) + \theta_2(t) = \hat{\theta}_1 e^{i\omega t} + \hat{\theta}_2 e^{-i\omega t}$$

If θ_1 and θ_2 are the solutions then they satisfy the general equation such that,

$$\begin{aligned} \frac{d\theta_1}{dt} + m\theta_1 &= n \frac{e^{i\omega t}}{2} \\ \frac{d\theta_2}{dt} + m\theta_2 &= n \frac{e^{-i\omega t}}{2} \end{aligned}$$

1.4.1. Solution for θ_1 and θ_2

$$i\omega \hat{\theta}_1 e^{i\omega t} + m\hat{\theta}_1 e^{i\omega t} = n \frac{e^{i\omega t}}{2}$$

Thus,

$$\hat{\theta}_1 (i\omega + m) = n/2$$

Rearranging,

$$\hat{\theta}_1 = \frac{n}{2} \frac{m - i\omega}{m^2 + \omega^2}$$

Similarly, for θ_2 , we get

$$\hat{\theta}_2 = \frac{n}{2} \frac{m + i\omega}{m^2 + \omega^2}$$

1.4.2. General solution

Combining both the solutions we get,

$$\theta = \frac{n}{2} \frac{m - i\omega}{m^2 + \omega^2} e^{i\omega t} + \frac{n}{2} \frac{m + i\omega}{m^2 + \omega^2} e^{-i\omega t}$$

Simplification leads to

$$\theta = \frac{n}{m^2 + \omega^2} [m \cos(\omega t) + \omega \sin(\omega t)]$$

1.4.3. Simplification in terms of ϕ

We define the phase lag in the solution from flash cooling, $\phi = \arctan(\omega/m)$. Integrating this in the general solution we get,

$$\theta = \frac{n}{m^2 + \omega^2} \frac{m}{\cos(\phi)} [\cos(\phi) \cos(\omega t) + \sin(\phi) \sin(\omega t)]$$

Since, $\cos(-\phi) = \cos\phi$, and $\sin(-\phi) = -\sin\phi$,

$$\theta = \frac{n}{m^2 + \omega^2} \frac{m}{\cos(\phi)} [\cos(\phi) \cos(\omega t) - \sin(\phi) \sin(\omega t)]$$

Using trigonometric identity for $\cos(x - y)$;

$$\theta = \frac{n}{m^2 + \omega^2} \frac{m}{\cos(\phi)} [\cos(\omega t - \phi)]$$

To simplify the equation and get the coefficient fully in terms of known properties, $\cos(\arctan(\omega/m)) = \frac{m}{\sqrt{m^2 + \omega^2}}$. Thus,

$$\theta = \frac{n}{\sqrt{m^2 + \omega^2}} \cos(\omega t - \phi)$$

1.5. Solution for dominant frequency response

Since $\Theta = \theta + \theta_p$, we get combined solution as

$$\Theta = \frac{n}{\sqrt{m^2 + \omega^2}} \cos(\omega t - \phi) + p$$

Converting it to original properties we get,

$$T(t) - T_a = \frac{-F/MC}{\sqrt{(hA/MC)^2 + \omega^2}} \cos(\omega t - \phi) + \frac{P - F}{hA}$$

$$T(t) - T_a = \frac{-F}{\sqrt{((hA)^2 + (\omega MC)^2)}} \cos(\omega t - \phi) + \frac{P - F}{hA}$$

$$T(t) - T_a = \frac{-F}{\sqrt{((hA)^2 + (\omega MC)^2)}} \cos(\omega t - \arctan(\omega/(hA/MC))) + \frac{P - F}{hA}$$

$$T(t) - T_a = \frac{-F}{(hA)\sqrt{(1 + (\omega MC/hA)^2)}} \cos(\omega t - \arctan(\omega MC/hA)) + \frac{P - F}{hA}$$

Which can be equivalently used with equation in terms of m;

$$T(t) - T_a = \frac{-F}{(hA)\sqrt{(1 + (\omega/m)^2)}} \cos(\omega t - \arctan(\omega/m)) + \frac{P - F}{hA}$$

Reminder: The driving factor for this problem is:

$$q_{fc} = F(1 + \cos(\omega t)) \text{ and } m = hA/MC$$

--- END of Section ---

2. Sample calculations

2.1. Single value of parameters (T vs t)

2.1.1. Prototype specific parameters

Input required parameters here. These parameters do not change for experiments (Ideally). $h(W/m^2K)$, $A(m^2)$, $M(kg)$, $C(J/kg)$;

In []:

```
h=5.5
A=0.1
M=1
C=130
m=h*A/(M*C)
print("The factor m in rad/s is", h*A/(M*C))
```

2.1.2. Experiment specific parameters

Input required parameters. $T_a(^{\circ}C)$, $P(W)$, $F(W)$, $\omega(rad/s)$

In []:

```
Ta=25
P=100
F=93.34

tp=2.4
w=2*np.pi/(tp)
print("frequency in Hz is", w/(2*np.pi))
print(w)
print(w/m)
```

2.1.3. Plotting T vs t at fixed omega

In []:

```
#Initialize zero/ spaced matrices if needed

x=np.linspace(403,650,2501)
y=np.linspace(403,650,2501)

#print(x,y)

m=h*A/(M*C)
phi=np.arctan(w*M*C/(h*A))
print(phi*180/(np.pi))

for i in range(len(x)):
    Amp=-F/(h*A*np.sqrt(1+(pow((w/m),2))))
    Angle=np.cos((w*x[i]-np.arctan(w/m)))

    y[i]=Ta+((P-F)/(h*A))+(Amp*Angle)

plt.figure(figsize=(15,10))
plt.xlabel('Time (s)')
plt.ylabel('Temperature ( $^{\circ}$ C)')
plt.plot(x,y)
plt.grid()
#plt.legend()
plt.rcParams["font.family"] = "Calibri"
plt.rcParams["font.size"] = "24"
```

In []:

```
## Rough comparison
a1=np.loadtxt("SP/SP20.txt")
time=np.array([i/10 for i in range(a1.shape[1])])
b1=np.vstack([a1,time])

plt.figure(figsize=(15,10))
plt.xlabel('Time (s)')
plt.ylabel('Temperature ( $^{\circ}$ C)')
plt.plot(b1[10,:],b1[3,:],'r',label='44W, 20s, 0.8mL')
#plt.plot(x,y)
plt.grid()
#plt.xlim(15,80)
#plt.legend()
plt.rcParams["font.family"] = "Calibri"
plt.rcParams["font.size"] = "24"
#plt.plot(b1[5,:],b1[1,:],'b',label='44W, 20s, 0.8mL')
```

2.2. Estimation for unknown parameters

First we lump the parameters in order to create the formula for curve fitting. The equation is as follows:

$$\Theta = \frac{-F}{(hA)\sqrt{(1 + (\omega(MC)/(hA))^2)}} \cos(\omega t - \arctan(\omega(MC)/(hA))) + \frac{P - F}{(hA)}$$

The known variables at any given time are: t, Θ, ω, P . The unknown (to be fitted) parameters are: $F, (hA), (MC)$.

We can write it as $y = f(x)$ assuming that the unknown parameters remain constant for a given experiment as variations in temperature are negligible compared to actual temperature. Since power is kept constant, the influence of power within a specific experiment is negligible.

2.2.1. Using SciPy curve-fit and pcov for sigma

In []:

```
#Importing only S-P data
c1=np.delete(b1,np.s_[0:4000],1)
c1=np.delete(c1,np.s_[2000:],1)
#c1=b1
print(np.size(b1,1),np.size(c1,1))
plt.plot(c1[10,:],c1[3,:])
```

In []:

```
# Data smoothing
c1[2,:] = savgol_filter(c1[2,:], 3, 2,mode='nearest')
```

In []:

```
Y=c1[3,:]-25 #Y=Theta
X=np.zeros((3,np.size(c1,1)))
X[0,:]=c1[5,:]-c1[5,0]
X[1,:]=np.zeros(np.size(c1,1))+w
X[2,:]=np.zeros(np.size(c1,1))+P
#print(X)

def sp(x,a,b,c): #a=F,b=hA,c=MC
    phi=np.arctan((x[1]*c)/b)
    return ((-(a*(np.cos((x[1]*x[0])-phi)))/(np.sqrt(1+np.power((x[1]*c)/b,2))))+(x[2]-a))/b

popt, pcov = curve_fit(sp, X, Y) #,bounds=([0,0,0],[0.91*P,10,1000]))
print(popt,pcov)
```

In []:

```
#Trial
#solving Theta=a*cos(wt-b)+c
Y=c1[3, :]-25 #Y=Theta
X=c1[10, :]-c1[10, 0]
b=0.55
c=130
#IF b=1
def sp(x, a): #a=F, b=hA, c=MC
    phi=np.arctan((w*c)/b)
    return ((-(a*(np.cos((w*x[0])-phi)))/(np.sqrt(1+np.power((w*c)/b, 2))))+((P-a))/b)
# return (((a*(np.cos((x[1]*x[0])-phi)))/(np.sqrt(1+np.power((x[1]*c)/b, 2))))-((x
[2]-a))/b)

popt, pcov = curve_fit(sp, X, Y)#bounds=([0, 0], [0.91*P, 100])
F=popt
phi=np.arctan((w*c)/b)
A=-(F/(np.sqrt(1+np.power((w*c)/b, 2))))
B=((P-F))/b+25
Ya=A*(np.cos(w*X-phi))+B
print(F)
print(popt, pcov)
print("A=", -(F/(np.sqrt(1+np.power((w*c)/b, 2))))
print("B=", ((P-F))/b+25)
print("phi=", phi)
print("Delay=", (phi*tp)/(2*np.pi))
```

In []:

```
plt.figure(figsize=(10, 10))
plt.xlabel('Time (s)')
plt.ylabel('Temperature ($^{\circ}$C)')
plt.plot(X, Y+25, 'r', label='Raw data')
plt.plot(X, Ya, 'k', label='Steady periodic assumption')
plt.legend(loc=2)
plt.ylim(36, 38)

plt.grid()
plt.legend(loc=1)
plt.rcParams["font.family"] = "Calibri"
plt.rcParams["font.size"] = "36"
plt.ylim(36.9, 37.3)
plt.xlim(50, 150)
```

Appendix E: Optimization code for thermal test vehicle

Part 1: Start of sample calculation

Material properties

Required material properties include resistivity (ρ) (in ohm-m) and Amperage (J) (Maximum current density)

In []:

```
#Material = Nichrome
#rho=5e-6
rho = 1.13e-6 #Ohm-m
#rho=5.05e-7
j= 5*1e8 #3*1.0E+8 #A/m^2
#print(rho,j)
```

Geometry

1. maximum square that can fit in a 4 inch (0.1 m) wafer is 0.0707 m.
2. We estimate be used for fabrication for heater on wafer is 65 mm x 65 mm.
3. The pads extend into the circular region.
4. The pads are to be designed into the 75 mm x 75 mm for Vapor Chamber project.

The design then depends on certain user defined constants and some variables:

User defined constants

Size of available (fabrication) wafer square side,

$$S_f = 0.065m$$

Length of wire for connection,

$$L_w = 0.02m$$

Spacing between heaters,

$$S_h = 0.0002m$$

In []:

```
#User-defined constants
sf=0.065
#Lw=20e-3
lw=0
#sh=1e-3
sh=200e-6
```

Geometry parameters (variables)

1. Number of heaters on each side, N . It provides more control of the heater as well helps to optimize V-I requirements with the the power supply. However, higher N would require large amount of controllers.
2. Thickness of wire, t , is limited by fabrication process
3. Width of wire, w , has a minimum limit depending on fabrication process
4. Spacing between wires, S_w , has a minimum limit depending on fabrication process

In []:

```
#For single calculations
n=10
t=1e-6 #1e-6
w=256e-6 #256e-6
sw=20e-6 #20e-6
#print(lw,sh,n,t,w,sw)
```

Geometry calculations for individual heater

Size of each heater,

$$S = \frac{(S_f - S_h(N - 1))}{N}$$

Number of wires in a heater,

$$N_w = \frac{S}{w + S_w}$$

Total length of wire for each heater,

$$L = L_w + N_w(S + S_w)$$

In []:

```
s = (sf-(sh*(n-1)))/n
nw=s/(w+sw)
l=lw+(nw*(s+sw))
print(s,nw,l) # Improve the display
```

Electrical calculation for individual heater

Resistance of wire,

$$R = \frac{\rho L}{wt}$$

Current capacity of wire,

$$I_{max} = Jtw$$

Maximum voltage,

$$V_{max} = I_{max}R$$

Maximum power,

$$P = V_{max}I_{max}$$

In []:

```
r=(rho*1)/(w*t)
imax=j*t*w
vmax=imax*r
pmax=vmax*imax
print(r,imax,vmax,pmax)

rhot=1e-7
Lt=15e-3
wt=7.5e-3
tt=250e-9
rt=rhot*Lt/(wt*tt)
imaxt=j*tt*wt
vmaxt=imaxt*rt
pmaxt=vmaxt*imaxt
print(rt,imaxt,vmaxt,pmaxt)

print(1.1e-5*15e-3/(320*250e-9))
```

Total power requirements

Since, voltage is shared by all the heaters in parallel, Total voltage,

$$V_{total} = V_{max}$$

Total current,

$$I_{total} = N^2 I_{max}$$

Total power,

$$P_{total} = N^2 V_{max} I_{max}$$

In []:

```
vt=vmax
it=(n*n)*imax
pt=(n*n)*pmax
print(vt,it,pt)
```

End on part 1

Part 2: Database generation and plotting

Material properties

Required material properties include resistivity (ρ) (in ohm-m) and Amperage (J) (Maximum current density)

In []:

```
#Material = Same as sample calculation  
rho = rho  
j=j  
#print(rho,j)
```

Geometry

1. maximum square that can fit in a 4 inch (0.1 m) wafer is 0.0707 m.
2. We estimate be used for fabrication for heater on wafer is 65 mm x 65 mm.
3. The pads extend into the circular region.
4. The pads are to be designed into the 75 mm x 75 mm for Vapor Chamber project.

The design then depends on certain user defined constants and some variables:

User defined constants

Size of available (fabrication) wafer square side,

$$S_f = 0.065m$$

Length of wire for connection,

$$L_w = 0.02m$$

Spacing between heaters,

$$S_h = 0.002m$$

In []:

```
#User-defined constants  
sf= 65e-3 #sf  
lw=lw  
sh=100e-6 #sh
```


Geometry parameters (variables)

1. Number of heaters on each side, N . It provides more control of the heater as well helps to optimize V-I requirements with the the power supply. However, higher N would require large amount of controllers.
2. Thickness of wire, t , is limited by fabrication process - We anticipate coating of roughly 50 nm to 300 nm - to be changed depending of first heater wafer.
3. Width of wire, w , has a minimum limit depending on fabrication process - resolution limit of 20 microns.
4. Spacing between wires, S_w , has a minimum limit depending on fabrication process - resolution limit of 20 microns.

Decision of grid spacing

$$P = \rho N^2 J^2 t w \left[L_w + \left(\frac{S_f - S_h(N-1)}{N(w + S_w)} \right) \left(\frac{S_f - S_h(N-1)}{N} + S_w \right) \right]$$

1. N is restricted to be an integer. After certain tests, we decide to choose maximum limit of 15 which includes both the current and power limits, thus giving a clear picture.
2. Dependency suggest that relation of Power to thickness is linear and from observations, so we choose 10.
3. The effect of width is unclear like N. However, with the tests considered and lack of abrupt changes, we choose 100 - this being the fine adjustment parameter for the design.
4. The reduction of spacing between wires help to reduce dead space and increase heating. The trend generally observed was close to linear drop with peak at minimum value. We choose 10.

In []:

```
na = np.linspace(10,10,1)
ta = np.linspace(1e-6,10e-6,10)
wa = np.linspace(256e-6,256e-6,1)
swa = np.linspace(20e-6,20e-6,1)
#print(n,t,w,sw)
```

Initialization

We need to initialize all the arrays based on the outputs we want to store in ou database. We have included $R, I_{max}, V_{max}, P_{max}, I_{total}, V_{total}, P_{total}$.

In []:

```
r=np.zeros((len(na),len(ta),len(wa),len(swa)))
imax=np.zeros((len(na),len(ta),len(wa),len(swa)))
vmax=np.zeros((len(na),len(ta),len(wa),len(swa)))
pmax=np.zeros((len(na),len(ta),len(wa),len(swa)))
it=np.zeros((len(na),len(ta),len(wa),len(swa)))
vt=np.zeros((len(na),len(ta),len(wa),len(swa)))
pt=np.zeros((len(na),len(ta),len(wa),len(swa)))
print(r)
```

Database

This step runs the calculations for all the possible values of input parameters specified about and creates a large database. This can easily be printed out within the same code cell. Please refer to sample calculation for detailed equations.

In []:

```
# Careful - this cell needs lot of time to run
for a in range(len(na)):
    for b in range(len(ta)):
        for c in range(len(wa)):
            for d in range(len(swa)):
                n=na[a]
                t=ta[b]
                w=wa[c]
                sw=swa[d]

                # sh=n*w

                s = (sf-(sh*(n-1)))/n
                print(s)
                nw=s/(w+sw)
                l=lw+(nw*(s+sw))
                r[a][b][c][d]=(rho*1)/(w*t)
                imax[a][b][c][d]=j*t*w
                vmax[a][b][c][d]=r[a][b][c][d]*imax[a][b][c][d]
                pmax[a][b][c][d]=vmax[a][b][c][d]*imax[a][b][c][d]
                vt[a][b][c][d]=vmax[a][b][c][d]
                it[a][b][c][d]=(n*n)*imax[a][b][c][d]
                pt[a][b][c][d]=(n*n)*pmax[a][b][c][d]

print(r)
```

Filter with constraints

1. We need to apply the current and voltage constraints for the heater.

$$C1 : I_{total} < I_{supply}$$

$$C2 : V_{total} < V_{supply}$$

1. We consider 20% safety limit and use 400 V (out of 500 V) and 40 A (out of 50 A) as our criterion.
2. We make power values zero for any combination if the any one or both constraints are not met. The max variables record and update the maximum values through the scan, and loc variables record the location where max power is observed. This will help during the plotting process.

In []:

```
max_p=0
max_i=0
max_v=0
max_n=0
max_t=0
max_w=0
max_sw=0
max_r=0
loc_n=0
loc_t=0
loc_w=0
loc_sw=0

for a in range(len(na)):
    for b in range(len(ta)):
        for c in range(len(wa)):
            for d in range(len(swa)):
                if vt[a][b][c][d] >400 or it[a][b][c][d]>40:
                    pt[a][b][c][d]=0
                if pt[a][b][c][d]>max_p:
                    max_p=pt[a][b][c][d]
                    max_i=it[a][b][c][d]
                    max_v=vt[a][b][c][d]
                    max_n=na[a]
                    max_t=ta[b]
                    max_w=wa[c]
                    max_sw=swa[d]
                    max_r=r[a][b][c][d]
                    loc_n=a
                    loc_t=b
                    loc_w=c
                    loc_sw=d
print(max_p,max_i,max_v,max_n,max_t,max_w,max_sw,loc_n,loc_t,loc_w,loc_sw,max_n*max_w,
max_r)
```

Plotting

1. The following plots show the relation between one of the four variables with current, voltage and power. The other 3 variables are kept constant for that plot. The plots are concurrent with expectations.
2. A good idea is to look at the plots at optimized point - this gives a larger confidence of a local maximum.
3. Another good idea can be to look at boundaries as well to provide more confidence about a global maximum.
4. Since N and w have most significant and non-linear impact on the power, we also plot a surface plot with power as output.

Plot 1: Number of heaters

In []:

```
plt.figure(figsize=(20,5))
plt.rcParams.update({'font.size': 16})

plt.subplot(1,5,1)
plt.plot(na,it[:,loc_t,loc_w,loc_sw], 'g')
plt.xlabel('Number of heaters, $N$')
plt.ylabel('Max current, $I_{max}(A)$')

plt.subplot(1,5,3)
plt.plot(na,vt[:,loc_t,loc_w,loc_sw], 'b')
plt.xlabel('Number of heaters, $N$')
plt.ylabel('Max voltage, $V_{max}(V)$')

plt.subplot(1,5,5)
plt.plot(na,pt[:,loc_t,loc_w,loc_sw], 'k')
plt.xlabel('Number of heaters, $N$')
plt.ylabel('Max power, $P_{max}(W)$')
plt.show()
```

Plot 1 Observations:

1. As expected total current increases with increase in N
2. As expected total voltage decrease with V
3. With w=5 mm, very small range (2-4) of allowed N but with high power.
4. With w=1 mm, larger range (3-12) of allowed N.

Plot 2: Thickness of wire

In []:

```
plt.figure(figsize=(20,5))
plt.rcParams.update({'font.size': 16})

plt.subplot(1,3,1)
plt.plot(ta,it[loc_n,:,loc_w,loc_sw], 'g')
plt.xlabel('Thickness of wire, $t$ (m)$')
plt.ylabel('Max current, $I_{\max}$ (A)$')

plt.subplot(1,3,2)
plt.plot(ta,vt[loc_n,:,loc_w,loc_sw], 'b')
plt.xlabel('Thickness of wire, $t$ (m)$')
plt.ylabel('Max voltage, $V_{\max}$ (V)$')

plt.subplot(1,3,3)
plt.plot(ta,pt[loc_n,:,loc_w,loc_sw], 'k')
plt.xlabel('Thickness of wire, $t$ (m)$')
plt.ylabel('Max power, $P_{\max}$ (W)$')
plt.show()
```

Plot 2 observations:

1. As expected, current is directly related to thickness (and not directly related to voltage).

Plot 3: Width of wire

In []:

```
plt.figure(figsize=(20,5))
plt.rcParams.update({'font.size': 16})

plt.subplot(1,3,1)
plt.plot(wa,it[loc_n,loc_t,:,loc_sw], 'g')
plt.xlabel('Width of wire, $w$ (m)$')
plt.ylabel('Max current, $I_{\max}$ (A)$')

plt.subplot(1,3,2)
plt.plot(wa,vt[loc_n,loc_t,:,loc_sw], 'b')
plt.xlabel('Width of wire, $w$ (m)$')
plt.ylabel('Max voltage, $V_{\max}$ (V)$')

plt.subplot(1,3,3)
plt.plot(wa,pt[loc_n,loc_t,:,loc_sw], 'k')
plt.xlabel('Width of wire, $w$ (m)$')
plt.ylabel('Max power, $P_{\max}$ (W)$')
plt.show()
```

Plot 3 Observations:

1. As expected, current is directly related to width.
2. The sharp relation to voltage is seen.
3. We get a window of allowable width.

Plot 4: Spacing between wires

In []:

```
plt.figure(figsize=(20,5))
plt.rcParams.update({'font.size': 16})

plt.subplot(1,3,1)
plt.plot(swa,it[loc_n,loc_t,loc_w,:], 'g')
plt.xlabel('Wire spacing,  $S_w$  (m)')
plt.ylabel('Max current,  $I_{max}$  (A)')

plt.subplot(1,3,2)
plt.plot(swa,vt[loc_n,loc_t,loc_w,:], 'b')
plt.xlabel('Wire spacing,  $S_w$  (m)')
plt.ylabel('Max voltage,  $V_{max}$  (V)')

plt.subplot(1,3,3)
plt.plot(swa,pt[loc_n,loc_t,loc_w,:], 'k')
plt.xlabel('Wire spacing,  $S_w$  (m)')
plt.ylabel('Max power,  $P_{max}$  (W)')
plt.show()
```

Part 4 observations

1. Close to inversely linear effect

Surface plot

In []:

```
plt.figure(figsize=(10,10))
X, Y = np.meshgrid(na, 1000*wa)
Z=pt[:,loc_t,:,loc_sw]
ax = plt.axes(projection='3d')
ax.view_init(45,15)
#ax.contour3D(X, Y, Z, cmap='binary')
ax.plot_surface(X, Y, Z, rstride=1, cstride=1,cmap='viridis', edgecolor='none')
ax.set_title('Total power (W)');
plt.ylabel('Width of wire, $w$ (mm)$')
plt.xlabel('Number of heaters, $N$')
plt.rcParams.update({'font.size': 20})
```

End of part 2

End of file

Appendix F: Thermal data for surrogate modeling

Experiment number	Input parameters			Processed state		Steady-periodic averages							
	Power, P (W)	Volume per pulse, v_p (mL)	Pulse interval, t_p (s)	State	Corrected pulse interval, $t_{p,c}$ (s)	Base temperature, $\langle T_b \rangle$ ($^{\circ}\text{C}$)	Outlet temperature, $\langle T_o \rangle$ ($^{\circ}\text{C}$)	Outlet pressure, $\langle P_o \rangle$ (kPa)	Variation in base temperature, $\langle \Delta T_b \rangle$ ($^{\circ}\text{C}$)	Flash cooling rate, $\langle q_{fc} \rangle$ (W)	Effective heat transfer, $\langle h_{eff} \rangle$ ($\text{W}/\text{m}^2\text{K}$)	Cumulative efficiency, η	
3	44	0.8	20	2	20.4	30.7	22	13.3	0.9	42	5798	0.78	
4	100	1.0	5	3	5.5	32.5	22.4	21.4	0.1	97	10267	0.39	
5	100	0.5	10	1	10.3								
6	100	0.8	10	2	10.5	34.2	22.1	20.6	0.2	96	8308	0.89	
7	200	0.7	5	0	5.3								
8	200	0.5	3	1	3.1								
9	200	0.5	3	1	3.4								
12	200	0.8	3	3	3.3	45	31.4	31.6	0.1	192	7626	0.57	
13	200	0.3	5	0	5.5								
14	200	0.3	3	0	3.3								
15	200	0.5	3	1	3.3								
17	200	0.3	1	4	1.4	42.4	30.4	31.2	0.1	193	8813	0.62	
20	100	0.2	2	2	2.4	37.9	22.9	21.3	0.1	95	5832	0.7	
21	150	0.2	2	2	2.3	60.3	25.9	23.7	0.1	136	3058	0.98	
22	200	0.2	2	0	2.2								
23	200	0.2	1	2	1.2	50.9	32.8	33.2	0.1	189	5817	0.77	
24	150	0.3	5	0	5.5								
25	150	0.7	5	3	5.4	45.5	27.4	26.4	0.1	142	5492	0.76	
26	150	0.6	5	1	5.4								
27	150	0.8	10	1	10.4								
28	150	1.0	10	2	10.4	68.2	25.8	23.2	0.9	133	2441	0.95	
31	150	0.5	3	4	3.4	43.8	27	26.7	0.1	142	6017	0.71	
32	200	1.0	5	2	5.4	47.7	32.1	32.6	0.1	191	6681	0.75	
33	200	0.3	2	1	2.2	0	0	0	0				
34	200	0.4	3	1	3.3	0	0	0	0				
35	150	0.7	4	2	4.4	44.4	27.2	26	0.1	142	5821	0.59	
36	200	0.8	4	2	4.5	52.8	32.7	32.1	0.1	189	5398	0.7	
37	150	0.9	4	3	4.5	46.1	27.8	26.7	0.1	141	5327	0.5	
38	200	1.1	5	3	4.5	76.8	30.2	29.8	0.1	179	2750	0.5	
40	200	0.8	3	4	3.5	67.1	27.8	31.1	0.1				

References

- [1] P. Reinke and G. Yadigaroglu, "Explosive vaporization of superheated liquids by boiling fronts," *Int. J. Multiphase Flow*, vol. 27, no. 9, pp. 1487-1516, 2001.
- [2] J. D. Engerer, "Rapid transient cooling utilizing flash boiling and desorption on graphitic foams," Purdue University, West Lafayette, IN, USA, 2016.
- [3] J. D. Engerer, J. H. Doty and T. S. Fisher, "Transient thermal analysis of flash-boiling cooling in the presence of high-heat-flux loads," *Int. J. Heat and Mass Transfer*, vol. 123, pp. 678-692, 2018.
- [4] E. Aktinol and V. K. Dhir, "Numerical simulation of nucleate boiling phenomenon coupled with thermal response of the solid," *Microgravity Science and Technology*, vol. 24, no. 4, pp. 255-265, 2012.
- [5] J. Mathew and S. Krishnan, "A Review on Transient Thermal Management of Electronic Devices," *ASME. J. Electron. Packag.*, vol. 144, no. 1, p. 010801, March 2022.
- [6] J. D. Engerer, J. H. Doty and T. S. Fisher, "Transient thermal analysis of flash-boiling cooling in the presence of high-heat-flux loads," *International Journal of Heat and Mass Transfer*, vol. 123, pp. 678-692, 2018.
- [7] J. D. Engerer and T. S. Fisher, "Flash boiling from carbon foams for high-heat-flux transient cooling," *Applied Physics Letters*, vol. 109, no. 2, pp. (024102) 1-4, 2016.
- [8] S. G. A. Andrae and T. Edler, "On Global Electricity Usage of Communication Technology: Trends to 2030," *Challenges*, vol. 6, no. 1, pp. 117-157, 2015.

- [9] A. Shehabi, S. Smith, D. Sartor, R. Brown, M. Herrli, J. Koomey, E. Masanet, N. Horner, I. Azevedo and W. Lintner, "United States Data Center Energy Usage Report," LBNL-1005775, Berkeley, CA, USA, June 2016.
- [10] S. S. Iyer, "Heterogeneous Integration for Performance and Scaling," *IEEE Transactions on Components, Packaging and Manufacturing Technology*, vol. 6, no. 7, pp. 973-982, 2016.
- [11] A. A. Bajwa, S. Jangam, S. Pal, N. Marathe, T. Bai, T. Fukushima, M. Goorsky and S. S. Iyer, "Heterogeneous Integration at Fine Pitch ($\leq 10 \mu\text{m}$) Using Thermal Compression Bonding," in *IEEE 67th Electronic Components and Technology Conference (ECTC)*, Orlando, FL, USA, 2017.
- [12] S. Jangam, A. Bajwa, K. K. Thankappan, P. Kittur and S. S. Iyer, "Electrical Characterization of High Performance Fine Pitch Interconnects in Silicon-Interconnect Fabric," in *IEEE 68th Electronic Components and Technology Conference*, San Diego, CA, USA, 2018.
- [13] U. Shah, U. Mogera, P. Ambhore, B. Vaisband, S. S. Iyer and T. S. Fisher, "Dynamic Thermal Management Of Silicon Interconnect Fabric Using Flash Cooling," in *18th IEEE Intersociety Conference on Thermal and Thermomechanical Phenomena in Electronic Systems (ITherm)*, Las Vegas, NV, USA, 2019.
- [14] P. Ambhore, U. Mogera, B. Vaisband, U. Shah, T. S. Fisher, M. Goorsky and S. S. Iyer, "PowerTherm Attach Process for Power Delivery and Heat Extraction in the Silicon-Interconnect Fabric Using Thermocompression Bonding," in *IEEE 69th Electronic Components and Technology Conference (ECTC)*, Las Vegas, NV, USA, 2019.

- [15] Intel Corporation, "Intel® Xeon® E-2288G Processor Specifications," 2019. [Online]. Available: <https://www.intel.com/content/www/us/en/products/sku/193743/intel-xeon-e2288g-processor-16m-cache-3-70-ghz/specifications.html>. [Accessed 24 September 2022].
- [16] N. Farrington, E. Rubow and A. Vahdat, "Data Center Switch Architecture in the Age of Merchant Silicon," in *17th IEEE Symposium on High Performance Interconnects*, New York, NY, 2009.
- [17] S. Liu, T. Lin, X. Luo, M. Chen and X. Jiang, "A microjet array cooling system for thermal management of active radars and high-brightness LEDs," in *ECTC*, San Diego, 2006.
- [18] M. X. Ma, "Experimental Investigation of Pressure-Controlled Boiling for Rapid Transient Cooling," University of California, Los angeles, 2021.
- [19] V. P. Carey, *Liquid-Vapor Phase-Change Phenomenon*, 2 ed., New York: Taylor and Francis Group, LLC, 2008.
- [20] V. K. Dhir, "Mechanistic Prediction of Nucleate Boiling Heat Transfer—Achievable or a Hopeless Task?," *ASME J. Heat Transfer*, vol. 128, no. 1, pp. 1-12, 2006.
- [21] J. G. Collier and J. R. Thome, "3. Empirical Treatments of Two-Phase Flow," in *Convective boiling and condensation*, New York, Oxford University Press, 1994, pp. 84-130.
- [22] G. Li, S. Fu, Y. Liu, Y. Liu, S. Bai and L. Cheng, "A homogeneous flow model for boiling heat transfer calculation based on single phase flow," *Energy conversion and management*, vol. 50, no. 7, pp. 1862-1868, 2009.

- [23] M. A. Grolmes and H. K. Fauske, "Axial propagation of free surface boiling into superheated liquids in vertical tubes," in *5th Int. Heat Transfer Conference*, Tokyo, Japan, 1974.
- [24] U. Shah, M. Ma, M. T. B.-C. ., Barako, S. S. Iyer and T. S. Fisher, "Experimental Demonstration of Pressure-Driven Flash Boiling for Transient Two-Phase Cooling," *IEEE Transactions on Components, Packaging and Manufacturing Technology*, vol. 11, no. 10, pp. 1604-1614, 2021.
- [25] K. Miyazaki, Y. Fujii-E and T. Suita, "Propagation of pressure wave in air-water twophase system (I)," *Journal of Nuclear Science and Technology*, vol. 8, no. 11, pp. 606-613, 1971.
- [26] G. Son, V. K. Dhir and N. Ramanujapu, "Dynamics and Heat Transfer Associated With a Single Bubble During Nucleate Boiling on a Horizontal Surface," *ASME J. Heat Transfer*, vol. 121, pp. 623-631, 1999.
- [27] M. Hasan and M. Monde, "Review of homogeneous nucleation boiling phenomenon under non-equilibrium heating condition and a generalized model for boiling explosion," *Trends in Heat and Mass Transfer*, vol. 13, pp. 1-26, 2013.
- [28] D. Kawano, H. Ishii, H. Suzuki, Y. Goto, M. Odaka and J. Senda, "Numerical Study on Flash-Boiling Spray of Multicomponent Fuel," *Heat Transfer-Asian Research*, vol. 35, no. 5, pp. 369-385, 2006.
- [29] A. Faghri and Y. Zhang, "Chapter 4: Generalized Governing Equations: Averaging Formulations," in *Transport Phenomena in Multiphase Systems*, Elsevier, 2006, pp. 238-330.

- [30] K. Sbutega, D. Geb and I. Catton, "Chapter 1: Modeling of Multiscale Heat Transfer Systems Using Volume Averaging Theory," *Advances in Heat Transfer*, vol. 47, pp. 1-165, 2015.
- [31] F. Zhou, "Development of Closure for Heat Exchangers Based on Volume Averaging Theory," University of California, Los Angeles, CA, USA, 2014.
- [32] F. D. Matteo, "Modelling and Simulation of Liquid Rocket Engine Ignition Transients," Sapienza Universita di Roma, Rome, Italy, 2011.
- [33] A. Majumdar, A. C. LeClair and R. Moore, "Generalized Fluid System Simulation Program (GFSSP), Version 6," in *AIAA Propulsion and Energy Forum*, Orlando, FL, USA, 2015.
- [34] R. P. Vara and P. C. Herrero, "Multidisciplinary simulation using EcosimPro," in *Reunión de Usuarios de EcosimPro*, Madrid, Spain, 2001.
- [35] J. Moral, R. P. Vara, J. Steelant and M. d. Rosa, "ESPSS Simulation Platform," in *Space Propulsion*, San Sebastian, Spain, 2010.
- [36] E. Lemmon, I. Bell, M. Huber and M. McLinden, "NIST Standard Reference Database 23: Reference Fluid Thermodynamic and Transport Properties-REFPROP, Version 10.0," Gaithersburg, 2018.
- [37] I. H. Bell et al., "Pure and Pseudo-pure Fluid Thermophysical Property Evaluation and the Open-Source Thermophysical Property Library CoolProp," *Industrial & Engineering Chemistry Research*, vol. 53, no. 6, pp. 2498-2508, 2014.
- [38] J. Wang and N. Zabararas, "Using Bayesian statistics in the estimation of heat source in radiation," *Int. J. Heat and Mass Transfer*, vol. 48, no. 1, pp. 15-29, 2005.

- [39] P. C. Tuan, S. C. Lee and W. T. Hou, "An efficient on-line thermal input estimation method using kalman filter and recursive least square algorithm," *Inverse Problems in Engineering*, vol. 5, no. 4, pp. 309-333, 1997.
- [40] W. Hou, D. Darakananda and J. Eldredge, "Machine Learning Based Detection of Flow Disturbances Using Surface Pressure Measurements," in *AIAA SciTech Forum*, San Diego, CA, USA, 2019.
- [41] J. Lee and I. Mudawar, "Two-phase flow in high-heat-flux micro-channel heat sink for refrigeration cooling applications: Part I—pressure drop characteristics," *Int. J. Heat and Mass Transfer*, vol. 48, no. 5, pp. 928-940, 2005.
- [42] D. G. Avraam and A. C. Payatakes, "Generalized relative permeability coefficients during steady-state two-phase flow in porous media, and correlation with the flow mechanisms," *Transport in Porous Media*, vol. 20, no. 1-2, pp. 135-168, 1995.
- [43] W. Chu, H. Lee, V. K. Dhir and I. Catton, "Hydrodynamics of two phase flow through homogeneous and stratified porous layers," University of California, Los Angeles, CA, USA, 1984.
- [44] T. L. Bergman, A. S. Lavine, F. P. Incropera and D. P. Dewitt, *Fundamentals of Heat and Mass Transfer*, Hoboken, NJ: John Wiley & Sons, 2007.
- [45] R. R. Tummala, *Fundamentals of Microsystems Packaging*, McGraw-Hill Education, 2001.
- [46] S. Pal, I. Alam, K. Sahoo, H. Suhail, R. Kumar, S. Pamarti, P. Gupta and S. S. Iyer, "I/O Architecture, Substrate Design, and Bonding Process for a Heterogeneous Dielet-

- Assembly based Waferscale Processor," in *IEEE 71st Electronic Components and Technology Conference (ECTC)*, San Diego, CA, 2021.
- [47] M. Liu, B. Vaisband, A. Hanna, Y. Luo, Z. Wan and S. S. Iyer, "Process Development of Power Delivery Through Wafer Vias for Silicon Interconnect Fabric," in *IEEE 69th Electronic Components and Technology Conference (ECTC)*, Las Vegas, NV, USA, 2019.
- [48] K. T. Kannan and S. S. Iyer, "Deep Trench Capacitors in Silicon Interconnect Fabric," in *ECTC*, Orlando, 2020, pp. 2295-2301.
- [49] A. Savitzky and M. J. E. Golay, "Smoothing and Differentiation of Data by Simplified Least Squares Procedures," *Analytical Chemistry*, vol. 36, no. 8, pp. 1627-1639, 1964.
- [50] P. Virtanen et al., "SciPy 1.0: Fundamental Algorithms for Scientific Computing in Python," *Nature Method*, vol. 17, pp. 261-272, 2020.
- [51] Thermal Devices, Inc, "Thermal Devices, Watlow ultramic 120V 580W ceramic heater," Watlow, 2023. [Online]. Available: <https://www.thermaldevices.com/product/watlow-ultramic-120-volt-580-watt-ceramic-heater-cer-1-01-00001/>. [Accessed May 2023].
- [52] ARCTIC GmbH, "MX-5 | Premium Thermal Paster for All CPU Applications," ARCTIC GmbH, 2021. [Online]. Available: <https://www.arctic.de/en/MX-5/ACTCP00043A>. [Accessed June 2022].
- [53] Q. Zhang, X. Xu, H. Li, G. Xiong, H. Hu and T. S. Fisher, "Mechanically robust honeycomb graphene aerogel multifunctional polymer composites," *Carbon*, vol. 93, pp. 659-670, 2015.
- [54] Y. C. Yortsos and A. K. Stubos, "Phase change in porous media," *Current Opinion in Colloid & Interface Science*, vol. 6, no. 3, pp. 2018-216, 2001.

- [55] G. M. Davies, N. A. Seaton and V. S. Vassiliadis, "Calculation of Pore Size Distributions of Activated Carbons from Adsorption Isotherms," *Langmuir*, vol. 15, no. 23, pp. 8235-8245, 1999.
- [56] G. Lauriat and V. Prasad, "Non-Darcian effects on natural convection in a vertical porous enclosure," *Int. J. Heat and Mass Transfer*, vol. 32, no. 11, pp. 2135-2148, 1989.
- [57] S. E. Buckley and M. C. Leverett, "Mechanism of Fluid Displacement in Sands," *Transactions of the AIME*, vol. 146, no. 1, pp. 107-116, 1942.
- [58] J. Bénard, R. Eymard, X. Nicolas and C. Chavant, "Boiling in Porous Media: Model and Simulations," *Transport in Porous Media*, vol. 60, no. 1, pp. 1-31, 2005.
- [59] M. A. Ahmadi and Z. Chen, "Comparison of machine learning methods for estimating permeability and porosity of oil reservoirs via petro-physical logs," *Petroleum*, vol. 5, no. 3, pp. 271-284, 2019.
- [60] S. Brunauer, P. H. Emmett and E. Teller, "Adsorption of Gases in Multimolecular Layers," *Journal of the American Chemical Society*, vol. 60, no. 2, pp. 309-319, 1938.
- [61] S. Tian, W. Ren, G. Li, R. Yang and T. Wang, "A Theoretical Analysis of Pore Size Distribution Effects on Shale Apparent Permeability," *Geofluids*, vol. 2017, pp. (7492328) 1-9, 2017.
- [62] C. Y. Wang and C. Beckermann, "A two-phase mixture model of liquid-gas flow and heat transfer in capillary porous media—I. Formulation," *Int. J. Heat and Mass Transfer*, vol. 36, no. 11, pp. 2747-2758, 1993.

- [63] C. Y. Wang and P. Cheng, "A multiphase mixture model for multiphase, multicomponent transport in capillary porous media—I. Model development," *Int. J. Heat and mass Transfer*, vol. 39, no. 17, pp. 3607-3618, 1996.
- [64] S. Whitaker, "Flow in Porous Media I: A Theoretical Derivation of Darcy's Law," *Transport in Porous Media*, vol. 1, no. 1, pp. 3-25, 1986.
- [65] H. C. Brinkman, "A calculation of the viscous force exerted by a flowing fluid on a dense swarm of particles," *Flow, Turbulence and Combustion*, vol. 1, no. 27, pp. 27-34, 1949.
- [66] S. Amini and S. Mohaghegh, "Application of Machine Learning and Artificial Intelligence in Proxy Modeling for Fluid Flow in Porous Media," *Fluids*, vol. 4, no. 3, pp. (126) 1-17, 2019.
- [67] P. Ambhore et al., "PowerTherm Attach Process for Power Delivery and Heat Extraction in the Silicon-Interconnect Fabric," in *ECTC*, Las Vegas, 2019, pp. 1605-1610.
- [68] Q. Zhang, Q. Bi, J. Wu, J. Liang and W. Wang, "Experimental investigation on the rapid evaporation of high-pressure R113 liquid due to sudden depressurization," *International Journal of Heat and Mass Transfer*, vol. 61, pp. 646-653, 2013.
- [69] D. Saury, S. Harmand and M. Siroux, "Flash evaporation from a water pool: Influence of the liquid height and of the depressurization rate," *International Journal of Thermal Sciences*, vol. 44, no. 10, pp. 953-965, 2005.
- [70] U. Shah and et al., "Dynamic Thermal Management Of Silicon Interconnect Fabric Using Flash Cooling," in *ITHERM*, Las Vegas, 2019.
- [71] J. D. Engerer and T. S. Fisher, "Flash boiling from carbon foams for high-heat-flux transient cooling," *Appl. Phys. Lett.*, vol. 109, no. 2, 2016.